1986

Progress Report No. 22

Biomedical Computer Laboratory

PROGRESS REPORT

No. 22

1 July 1985 - 30 June 1986

Biomedical Computer Laboratory

Institute for Biomedical Computing

Washington University

700 South Euclid Ave.

St. Louis, Missouri 63110

BIOMEDICAL COMPUTER LABORATORY

INSTITUTE FOR BIOMEDICAL COMPUTING

WASHINGTON UNIVERSITY

PROGRESS REPORT NO. 22

JULY 1, 1985 - JUNE 30, 1986

TABLE OF CONTENTS

I. INTRODUCTION

This progress report from the Biomedical Computer Laboratory (BCL) summarizes activities during the period from July 1, 1985 through June 30, 1986. The Biomedical Computer Laboratory collaborates with research investigators throughout the Washington University School of Medicine and its affiliated hospitals in the application of advanced computer techniques to problems in biology and medicine. This often requires work in areas stretching from basic biomedical sciences through mathematical models to equipment design. Our orientation is interdisciplinary with the recognition that effective communication for workers with differing backgrounds comes only through extended collaboration and mutual respect.

The vigorous development and evolution of specialized hardware and software systems for use in the solution of research and clinical problems has continued to be the central focus of BCL activities. Several systems now in clinical use have seen a progression from exploratory pilot studies, to major developmental project, to local clinical trial, to clinical trials in multiple locations, to public availability through commercial manufacture. Perseverance in this sometimes tedious chain of development has found reward in the effective fielding of specialized computer systems to the medical community.

One class of computer applications requires strong coupling of the computer to its environment for digital signal processing. These applications typically involve the use of commercially available minicomputers and microprocessors in conjunction with specialized hardware designed and built locally. We have pursued many such applications by bringing signals from hospital wards and research laboratories to BCL by means of either analog or digital tape recordings or telephone lines and, more frequently, by taking the computers to the investigator's laboratory or the patient's bedside. More recently, an emphasis at BCL has been on the development of a flexible digital communication capability for linking data sources and information destinations with research-oriented computational resources at BCL as well as at collaborators' sites.

Of particular importance to current and future BCL projects is the development, in a closely related sister lab (Computer Systems Laboratory, or CSL), of a capability for the design and fabrication of custom very-large-scale integrated (VLSI) circuits. The realization of such circuits through collaboration with CSL is already opening up new opportunities for solving problems intractable with conventional computing devices. The CSL has as its goal the development of innovative approaches to computing that will have important implications for medicine and biology in the future.

For those classes of applications dominated by information processing requirements, provisions have matured from telephone lines linking our minicomputers to the large IBM Systems at the Washington University Computing Facilities, through development and support of a minicomputer based MUMPS system, to the establishment of independent groups such as the Medical Computing Facility and the Medical Computing Service Group which serve the local medical complex. Diverse needs continue to be met by these various options as well as by an increasing number of independent computing facilities within medical school departments.

Still another class of applications requires extensive use of large-scale computational services. Many investigators are assisted in their research through the use of generalized numerical, non-numerical, and statistical routines. Such work is sometimes carried out by staff members of BCL, but primarily by members of the Division of Biostatistics under the direction of Dr. Dabeeru C. Rao, and the University Computing Facilities whose director is Robert J. Benson.

Over the years, the BCL has enjoyed collaborations with most departmental divisions within the medical school but has also found support and enrichment through close ties with other facilities throughout the University. These arrangements are of benefit both to the BCL and to graduate students who find projects and employment among the activities in the laboratory. The Department of Computer Science is under the direction of Dr. Jerome R. Cox, Jr., past Director of the BCL. Strong ties with the Department of Electrical Engineering are sustained through the Engineering School's Biomedical Engineering Program and common interests in digital signal processing techniques. The Department of Electrical Engineering has been chaired by Dr. Donald L. Snyder, past Associate Director of BCL.

Two years ago, Washington University established an interschool Institute for Biomedical Computing. The new Institute encompasses the Biomedical Computer Laboratory and the Computer Systems Laboratory in an organizational setting designed to recognize and foster the joint interests in biomedical computing of the School of Medicine and the School of Engineering and Applied Science. The purpose of the reorganization is to recognize that the development and application of advanced computing and engineering technology to problems in biomedical science are essential components of the research and teaching activities of Washington University. Accordingly, attention has been given to the development of a stable organizational structure that will 1) provide a means by which the primary academic affiliations of its faculty can be in an organizational setting with an adequately broad commitment to research and teaching in biomedical computing; 2) establish a formal administrative connection to the School of Engineering and Applied Science that will facilitate the involvement of its students and faculty in research and instructional activities in biomedical computing; 3) establish mechanisms for adminstration, funding, and review of appointments, promotion, and tenure for the academic staff of this activity; 4) foster organizational and procedural coherence between the Biomedical Computer Laboratory and the Computer Systems Laboratory by placing them within a common administrative structure; 5) create a focal point for interdisciplinary teaching and student research, both in the School of Medicine and the School of Engineering and Applied Science, in areas that do not fit comfortably into existing departments; and 6) encourage a scholarly environment for the activities of the two computer laboratories that will promote and encourage teaching, research, and publication as vehicles for personal development and academic contribution.

In addition to current BCL and CSL space on the Medical School campus, space for part of the activities of the Institute has been provided on the Engineering School campus by completion of a fifth-floor addition to Lopata Hall in December of 1983. This new space (about 6000 square feet), called the Edward L. Bowles Laboratory, is immediately adjacent to the Departments of Computer Science and Electrical Engineering.

The Institute for Biomedical Computing (IBC) has replaced the former Washington University Computer Laboratories (WUCL) which was a less formal federation of BCL and CSL plus working groups within the Departments of Computer Science and Electrical Engineering. Dr. Charles E. Molnar, Director of the Computer Systems Laboratory, and Dr. Lewis J. Thomas, Jr., Director of the Biomedical Computer Laboratory, are respectively Director and Associate Director of the Institute. Both BCL and CSL continue to retain their identities and internal organizations. Accordingly, this Progress Report addresses activities centered primarily within BCL.

Planning and policy development of the Institute are overseen by a Governing Board, the membership of which is drawn from both Schools. The present composition of the Governing Board is:

J. R. Cox, Jr., Chairman, Department of Computer Science
N. Daw, Professor, Department of Cell Biology and Physiology and Department of Ophthalmology
R. G. Evens, Head, Department of Radiology
M. K. King, Dean, School of Medicine
D. M. Kipnis, Chairman, Department of Internal Medicine
E. L. MacCordy, Associate Vice-Chancellor for Research
J. M. McKelvey, Dean, School of Engineering and Applied Science
C. E. Molnar, Director, Computer Systems Laboratory
P. Needleman, Head, Department of Pharmacology
D. L. Snyder, Chairman, Department of Electrical Engineering
L. J. Thomas, Jr., Director, Biomedical Computer Laboratory

To aid in long-range planning of the health-related activities of the Institute, a National Advisory Panel is convened periodically. Particular attention is given to the confluence of important needs in biology and medicine with the technical advances capable of meeting these needs. Successful development may suggest implementation on a larger, perhaps national scale. The present composition of the National Advisory Panel is:

Peter H. Abbrecht, M.D., Ph.D., Professor of Physiology and Medicine, Uniformed Services University of the Health Sciences, Bethesda, Maryland

Howard L. Bleich, M.D., Associate Professor, Beth Israel Hospital, Harvard Medical School

Wesley A. Clark, A.B., Consultant, Sutherland & Sproull Associates, New York, New York,

James N. Gray, Ph.D., Tandem Computer Company, Cupertino, California

Frank E. Heart, M.S.E.E., Vice President and Director, Computer Systems Division, Bolt, Beranek & Newman, Cambridge, Massachusetts

David M. Kipnis, Professor and Chairman, Department of Internal Medicine, Washington University

Brian W. Matthews, Ph.D., Professor, Institute of Molecular Biology, University of Oregon

John M. Smith, Director, Sponsored Research Division, Computer Corporation of America, Cambridge, Massachusetts

Eugene A. Stead, Jr., M.D., Florence McAlister Professor of Medicine, Department of Medicine, Duke University

Carlos Vallbona, M.D., Chairman, Department of Community Medicine, Baylor College of Medicine

II. SOURCES OF SUPPORT

During the period covered by this report the primary source of support for the Biomedical Computer Laboratory was from two grants from the National Institutes of Health, Division of Research Resources.

RR 01380	A Resource for Biomedical Computing.
RR 01362	Tissue Characterization via Ultrasonic Imaging.

NHLBI contract NO1 HV 72941 continues to fund a Holter Monitoring Core Laboratory to support a Multicenter Investigation of Limitation of Infarct Size.

Collaboration with other investigators often involved work already supported by other grants and contracts.

Public Health Services.

CA 41574	Accurate Photon Dose Calculations by Radiotherapy,
CM 47696	Evaluation of High Energy Photon External Beam Treatment Planning,
GM 28232	Physical Mapping of Yeast Chromosomal DNA,
HL 13851	Cyclotron Produced Isotopes in Biology and Medicine,
HL 17646	Study of Ischemic Heart Disease,
HL 25944	Time-of-Flight Positron Tomography for Cardiac Imaging,
HL 28995	Adrenergic Factors and Arrhythmogenic Metabolites,
HL 28998	Tissue Characterization with Ultrasound,
HL 31531	Coronary Vascular Response to Injury: Role in Infraction,
NS 06833	An Interdisciplinary Stroke Program,
RR 01379	Research in VLSI Systems for Biomedical Applications.

National Science Foundation Grant.

ECS-82-15181 Study of Time-of-Flight Tomography.

Research support was also received from the following industrial collaborators.

Biosensor Corporation, Brooklyn Center, MN,
Digital Equipment Corporation, Maynard, MA,
International Business Machines Corporation, St. Louis, MO,
Mead Johnson, Evansville, IN.

III. PERSONNEL

EMPLOYEES

Personnel employed by the Biomedical Computer Laboratory during the period covered by this report were:

Director

Lewis J. Thomas, Jr., M.D., and Associate Director of Institute for Biomedical Computing, and Associate Professor of Biomedical Computing, Anesthesiology, Cell Biology and Physiology, Biomedical Engineering, and Electrical Engineering

Associate Director

G. James Blaine III, D.Sc., and Associate Professor of Biomedical Computing in the Institute for Biomedical Computing, and Affiliate Associate Professor of Electrical Engineering and Computer Science

Senior Research Associates

Jerome R. Cox, Jr., Sc.D., and Professor of Biomedical Computing in the Institute for Biomedical Computing, and Chairman and Professor of Computer Science, and Professor of Electrical Engineering

Harold W. Shipton, C.Eng., and Professor of Biomedical Engineering in the Institute for Biomedical Computing, and Chairman and Professor of Biomedical Engineering

Donald L. Snyder, Ph.D., and Professor of Biomedical Computing in the Institute for Biomedical Computing, and Chairman and Professor of Electrical Engineering

Business Manager

Virginia M. Bixon, B.S.

Research Associates

R. Martin Arthur, Ph.D., and Professor of Biomedical Computing in the Institute for Biomedical Computing, and Professor of Electrical Engineering

Kenneth W. Clark, M.S.

Daniel R. Fuhrmann, Ph.D., and Assistant Professor of Electrical Engineering

Kenneth B. Larson, Ph.D.

James G. Miller, Ph.D., and Professor of Physics, and Associate Director for Biomedical Physics, Laboratory for Ultrasonics, and Research Associate Professor of Medicine

Michael I. Miller, Ph.D., and Assistant Professor of Biomedical Computing in the Institute for Biomedical Computing, and Assistant Professor of Electrical Engineering

Frederick U. Rosenberger, D.Sc., Associate Professor of Biomedical Computing in the Institute for Biomedical Computing, and Associate Professor of Electrical Engineering

Arthur W. Toga, Ph.D., Research Assistant Professor of Neurology

Jonathon S. Turner, Ph.D., Assistant Professor of Computer Science

Research Assistants

David E. Beecher, M.S., and Lecturer in Computer Science
Michael A. Brown, M.S.
William P. Hellberg, B.S.
Russell E. Hermes, M.S.
Patrick H. Johnston, Ph.D.
Joanne Markham, M.S., and Research Assistant Professor in Medicine
Stephen M. Moore, M.S.
Jack G. Mottley, Ph.D.
Kenneth B. Schechtman, Ph.D., and Instructor in Biostatistics in Preventive Medicine, and Research Instructor in Medicine
Tom O. Videen, Ph.D.

Graduate Research Assistants

Steven R. Broadstone, M.S.
Mark R. Holland, M.A.
Neophytos Karamanos, B.S.
Mark E. Kaufmann, M.A.
Arun Kumar, B.Tech.
Stephen K. Liu, B.S.
John M. Ollinger, M.S.
Badrinath Roysam, B.Tech.
Evren Senol, B.S.
Kurt R. Smith, M.S.

Engineering Assistant

Stanley R. Phillips, A.A.S.

Electronic Technician

Deborah A. Schwab

Secretaries

Rebecca J. Bozesky
Shirley A. Gonzalez-Rubio
Polly E. Raith

The following members from other departments and divisions have joint appointments with the Biomedical Computer Laboratory to facilitate collaboration and enhance interdisciplinary research:

H. Dieter Ambos, Research Assistant Professor of Medicine (Cardiology)
A. Maynard Engebretson, D.Sc., Associate Professor of Electrical Engineering in the Department of Speech and Hearing, and the Faculty of Arts and Sciences
William M. Hart, Jr., M.D., Ph.D., Associate Professor of Ophthalmology
Rexford L. Hill III, M.S., Associate Professor of Computer Applications in Radiology
David G. Politte, M.S., Research Assistant in Radiology

John W. Wong, Ph.D., Assistant Professor of Radiation Physics in Radiology

In addition, the following people worked at the laboratory for brief periods:

Shahid Akhtar, B.S.
Heather A. Drury
Sudjiwo Husodo, B.S.
Yau-Man Kwan, M.S.
Joseph C. Lawrence
Anders W. McCarthy
Brian D. Skinner
Ellen E. Witte
Xinscheng Yu

RESEARCH COLLABORATORS

During the period covered by this report the following investigators from other laboratories, departments, or institutions, collaborated with BCL staff members on problems of joint interest.

D. R. Abendschein, Ph.D., Medicine
H. D. Ambos, Medicine
T. R. Baird, Medicine
D. G. Ballinger, B.S., Radiology
S. R. Bergmann, M.D., Ph.D., Medicine
J. J. Billadello, M.D., Medicine
W. R. Binns, Ph.D., Physics
M. A. Brown, M.D., Medicine
P. B. Corr, Ph.D., Medicine and Pharmacology
A. G. Davis, M.D., Medicine
S. R. Devries, M.D., Medicine
R. D. Edelman, B.S., Computer Systems Laboratory
J. O. Eichling, Ph.D., Radiology
B. N. Emami, M.D., Radiology
J. W. Epstein, Physics
R. G. Evens, M.D., Radiology
D. C. Ficke, B.S., Radiology
P. T. Fox, M.D., Neurology and Radiology
M. H. Gado, M.D. Radiology
R. A. Gardner, Ph.D., Mechanical Engineering
S. K. Ge, Radiology
E. M. Geltman, M.D., Medicine
R. L. Grubb, Jr., M.D., Neurological Surgery
W. B. Harms, B.S., Radiology
W. M. Hart, Jr., M.D., Ph.D., Ophthalmology
P. Herscovitch, M.D., Neurology and Radiology
G. R. Hoffman, B.A., Radiology
J. Howe, Pathology
S. Igielnik, Ph.D., Medical Computing Facilities
M. H. Israel, Ph.D., Physics
A. S. Jaffe, M.D., Medicine
G. C. Johns, B.S., Computer Systems Laboratory
R. G. Jost, M.D., Radiology
M. R. Kilbourne, Ph.D., Radiology

J. Klarmann, Ph.D., Physics
H. A. Klotz, M.S., Electrical Engineering
K. E. Krippner, B.S., Radiology
E. T. Macke, M.S., Computer Systems Laboratory
J. W. Matthews, D.Sc., Computer Systems Laboratory
T. R. Miller, Radiology
M. A. Mintun, M.D., Radiology
C. E. Molnar, Sc.D., Computer Systems Laboratory
S. P. Monthofer, Radiology
D. W. Myears, M.D., Medicine
M. V. Olson, Ph.D., Genetics
R. E. Olson, Computer Systems Laboratory
C. A. Perez, M.D., Radiology
J. E. Perez, M.D., Medicine
J. S. Perlmutter, M.D., Neurology
S. M. Pogwizd, M.D., Medicine
D. G. Politte, M.S., Radiology
W. J. Powers, M.D., Neurology and Radiology
J. A. Purdy, Ph.D., Radiology
M. E. Raichle, M.D., Neurology and Radiology
B. H. Raup, Physics
T. L. Rosamond, M.D., Medicine
A. P. Rueter, B.S., Radiology
J. E. Saffitz, M.D., Pathology and Medicine
B. A. Siegel, M.D., Radiology
E. D. Slessinger, M.S., Radiology
B. E. Sobel, M.D., Medicine
A. W. Strauss, M.D., Biochemistry and Pediatrics
S. P. Sutera, Ph.D., Mechanical Engineering
M. M. Ter-Pogossian, Ph.D., Radiology
R. G. Tilton, Ph.D., Pathology
M. W. Vannier, M.D., Radiology
T. O. Videen, Ph.D., Neurology
M. J. Welch, Ph.D., Radiology
J. R. Williamson, M.D., Pathology
J. W. Wong, Ph.D., Radiology
K. A. Yamada, Ph.D., Medicine
C. Y. Yu, M.S., Radiology
J. B. Zimmerman, D.Sc., Radiology and Computer Science

Biosensor Corporation, Brooklyn Center, Minnesota

C. N. Mead, M.D.

Jewish Hospital, St. Louis, Missouri

R. Ruffy, M.D.

Medical College of Ohio, Toledo, Ohio

S. M. Hancock, M.S.

St. Louis Medical Center, St. Louis, Missouri

T. Roy, M.D.

As in the past, collaborative effort with commercial firms continues. This year a project of joint interest involved the Mead Johnson Corporation, Pharmaceutical Division, Evansville, Indiana.

IV. PHYSICAL RESOURCES

The Biomedical Computer Laboratory (BCL) was formed on April 15, 1964 and the original staff moved into 3,800 square feet (net) of laboratory space at 700 South Euclid Avenue in St. Louis. While remaining at this location, adjacent to the Washington University School of Medicine's main building complex, the floor space has been increased to the present 12,000 square feet (net). As a result of the establishment of an interschool Institute for Biomedical Computing at Washington University, space for part of the activities of the Institute (which encompasses both the BCL and the Computer Systems Laboratory (CSL) has been created on the Engineering School campus by completion of a fifth-floor addition to Lopata Hall. This new space (about 6000 square feet), called the Edward L. Bowles Laboratory, is immediately adjacent to the Departments of Computer Science and Electrical Engineering. It became available in December, 1983. In addition to the 700 South Euclid and Bowles Laboratory space, BCL staff members and systems frequently occupy other areas within the Washington University Medical Center at the sites of collaborative project activities.

During the past twenty years BCL has addressed diverse biomedical problems for which digital computing techniques seemed promising and appropriate. A single Laboratory Instrument Computer (LINC) provided the original staff with an opportunity to apply digital computing to a few interesting problems in medicine and biology. Currently BCL has interest and involvement in several specialized instrumentation and computing systems which provide access to diverse image-data sources (modalities) and offer opportunities for collaborative research in biological modeling and algorithm development. BCL has primary responsibility for a complement of computing hardware and software which include: Digital Equipment Corporation MicroVAX-II's and LSI-11's, and MASSCOMP Corporation MC-500's. An MMS-X stroke graphics display system developed by the Computer Systems Laboratory, a Lexidata raster-graphics display system and two MASSCOMP raster-graphic display stations are available for biomedical imaging studies. Personal-class microcomputer systems have been incorporated into the design of biomedical research systems and numerous special-purpose devices have been developed using microprocessor chip-sets and microcomputer board-level assemblies.

A Resource-developed local area network, TERRANET, provides remote terminal-to-computer and inter-computer data communications at rates up to 9600 bps. Two, thirty station networks support terminals and computer systems located throughout the laboratories. Internetwork communication is provided between these networks and others within Washington University, giving access to a broad spectrum of computing equipment and services for use by resource personnel.

A machine shop and reference room are located on the 700 S. Euclid premises and shared with CSL. Other physical resources include a well-stocked electronics shop, a large inventory of electronic and computer test equipment, a variety of digital system modules and both analog and digital recording instruments. Systems for use in developing eight-bit, sixteen-bit and bit-slice microprocessor applications are available.

V. RESEARCH PROJECTS

Introduction

The research program of the Biomedical Computer Laboratory (BCL) is organized into six major project areas with the staff grouped into teams whose interests are focused correspondingly. Because of the growth of the Laboratory's activities in the area of quantitative imaging, that category has been divided into three sections, each dealing with a different imaging modality (ultrasound, radiation-treatment planning, and positron-emission tomography). A total of 52 distinct project activities are grouped into the six project areas briefly summarized below. More complete summaries are given at the beginning of each of the project-report subsections.

Ischemic heart disease and ECG analysis continues to be a major category of research activity, but the development of new algorithms for ECG processing has become less prominent than in the past as a result of a shift in emphasis to exportation of the latest version of our "Argus" algorithm. As that work is being brought to a conclusion, the final evaluation now in progress is showing that the revised algorithm achieves the high level of performance required for real-time, ambulatory ECG-monitoring applications. In the area of ischemic heart disease, more prominent than before are modeling, signal processing, and data analysis work in collaboration with the division of Cardiovascular Medicine as part of their broad program addressed to ischemic heart disease.

Information extraction from quantitative biomedical images continues to increase in prominence within the BCL program. Accordingly, last year's organization of such activities into three categories (by imaging modality) is continued this year. The work in ultrasonic tissue characterization now emphasizes the interpretation of backscattered ultrasonic energy to achieve quantitative estimates of tissue properties, including anisotropy and the state of contraction of cardiac and skeletal muscle, while parallel efforts are directed toward design of a system to employ adaptive beamforming for backscatter measurements.

Work in radiation treatment planning has moved ahead with enhancements and evaluations of our "delta volume" algorithm for three-dimensional absorbed-dose calculations, display experiments employing high-performance stroke graphics (MMS-X system), and the recent completion of two VLSI circuits for expeditious achievement of a demanding kernel of the computations (3-D ray tracing). New work now focuses on the physics of high-energy photon-dose deposition in heterogeneous media.

For positron-emission tomography, work in support of applications and system improvements have continued on several fronts, but the main thrust of BCL activities has been in research on algorithms. Emphasis has been on application of the maximum-likelihood method for improving image quality and for achieving better estimates of physiological parameters through studies of dynamic distributions of tracers. Important new developments include the application of kernel seives to address image artifacts and the formulation of a model for applying the maximum-likelihood method to single-photon emission computed tomography (SPECT).

Systems for Specialized Biomedical Studies embraces a variety of projects that are less broad in scope either because they are in an earlier stage of development or because the nature of the work is necessarily more specialized. The biomedical-imaging theme is well represented in this section as well.

Projects under Resource Development Activities are directed toward improving the Laboratory's capabilities for addressing the needs of multiple research studies involving various facets of biomedical imaging. To that end, a now dominant and integrating activity is the development of a distributed facility for image presentation, analysis and quantification (IPAQ). Components of the IPAQ project include (1) the enhancement of our computational capabilities to support the development of computationally demanding algorithms for information extraction from multi-dimensional measurement data, (2) the establishment of a coherent software environment which incorporates a set of internally consistent software tools, image data formats and display methodologies, (3) the extension of our digital communication capabilities to include the sites of collaborators' data sources and information destinations, and (4) the exportation of specialized, tailored subsystems and/or satellite workstations which may incorporate custom-designed, very-large-scale integrated (VLSI) circuits in order to achieve practical realizations of especially demanding computations.

Individual Projects

A. Ischemic Heart Disease and ECG Analysis

Some of the projects in this section continue longstanding work in high-speed ECG analysis. Other projects in cardiology have supported collaborations which address other aspects of ischemic heart disease, such as the assessment of vascular integrity of the myocardium following ischemic injury, the electrophysiological and biochemical factors underlying the genesis of arrhythmias due to myocardial ischemia and infarction, the kinetics of positron-emitting radiotracers as tools for characterizing myocardial perfusion and metabolism, and the analysis of plasma CK isoforms.

A real-time computer-based arrhythmia monitoring system, called Argus, was in operation in the Barnes Hospital Coronary Care Unit from 1969 until 1975 when it was replaced by a commercial version of the system developed through collaboration with Mennen-Greatbatch Company. In the early 1970's, we developed a system called Argus/H for high-speed processing of long-term (10 hours) single-channel tape-recorded ECGs (Holter ECGs). Argus/H was used for a study of ventricular arrhythmias in survivors of myocardial infarction as well as for several minor studies and continued ECG signal processing algorithm development. Heavy demand eventually required a second Argus/H system.

By the late 1970's, we developed a system called Argus/2H for high-speed processing of 24-hour dual-channel Holter ECGs. Heavy use of this system also led to its duplication. The Argus/2H systems processed several thousand Holter ECGs for national multicenter trials and for several local studies; ECG signal processing algorithm development also continued in strong fashion. At present, we have completed participation in most of the Holter ECG tape processing studies. Recent algorithm development has led to major refinements and additions which we call Argus/R (revised). These enhancements include frequency-domain analysis techniques applied to the classification of QRS complexes. These developments have led to a commercial implementation of a portable real-time ECG arrhythmia analyzer which embodies the Argus/R algorithms. Both the local Argus/R system and its commercial implementation are now going through final evaluations.

A-1. Argus Algorithm Development

Personnel: C. N. Mead, Biosensor Corporation
K. W. Clark, BCL
L. J. Thomas, Jr., BCL

Support: RR 01380
Biosensor Corporation

The Argus/R (revised) algorithms for high-speed ECG processing have changed relatively little since evaluation results were reported a year ago (PR 21, A-1). Those results measured the PVC detection performance of Argus/R on the American Heart Association (AHA) Database of Ventricular Arrhythmias. During the past year, the modules for noise detection and atrial fibrillation analysis were enhanced, and the entire set of Argus/R algorithms was re-run on the AHA database. The algorithms were also run against the Massachusetts Institute of Technology/Beth Israel (MIT/BIH) database, a set of tapes richer than the AHA database in both noise content and presence of atrial fibrillation. The results of these evaluations indicated no degradation in performance as reported a year ago.

Concurrently, the Biosensor Corporation (Brooklyn Center, MN) has continued the development, field testing, and marketing of their real-time microprocessor implementation of Argus/R. In the process of field testing, Biosensor discovered some potential shortcomings in the algorithms when applied to time periods exceeding several hours. The deficiencies were corrected in the BCL and Biosensor versions of Argus/R. This discovery suggested that the AHA and MIT/BIH databases may be excellent foundations for fundamental algorithm development, but that they may be inadequate in some respects for real-world application.

Based on this experience, we began to consider construction of a database of longer records (the MIT/BIH database consists of twenty-minute records and the AHA database consists of 3-hour records; all beats in the MIT/BIH database are annotated while only beats in the last half-hour of the AHA records are annotated). Two additional observations propelled our efforts to construct such a database. First, Biosensor's experience with multiple physician-users indicated that clinicians are not so much interested in total, absolute PVC counts as they were in "clinically relevant event" detection (i.e., order-of-magnitude hourly PVC counts were acceptable from a clinical point of view as long as a system could reliably detect ventricular tachycardia). This observation suggested our database should be annotated not on a beat-by-beat but rather on an event basis. Second, in contrast to Biosensor's digital ECG system, many ECG systems are analog or hybrid in nature and have no means to record timing marks on individual beats, thus, measuring the performance of such systems using the beat-by-beat annotated AHA or MIT/BIH databases is at best cumbersome. On the other hand, measuring performance based on event detection (type and approximate time) is much less restrictive.

Based on these observations, we have begun to construct an "annotated clinical event" data base (ACEDB). Although the final content of ACEDB is not yet totally agreed upon, initial efforts have centered around the selection and event-annotation of 60 six-hour recordings, 10 in each of the following classes: (1) ventricular runs, (2) ventricular

pairs, (3) ventricular bigeminy, (4) pauses > 1.5 seconds (or heart rate < 40), (5) paroxysmal supraventricular tachycardia, and (6) paroxysmal atrial fibrillation/flutter. For a given class, each tape within the class contains at least one example of the class dysrhythmia but may contain other events from other classes (i.e., a tape with ventricular runs might also contain episodes of atrial fibrillation. All 60 recordings were selected from a database accumulated during the MILIS (Multicenter Investigation of the Limitation of Infarct Size) clinical trial (PR 19, A-12). All MILIS tapes had previously been analyzed, reviewed, and cataloged by cardiologists with respect to dysrhythmic content. For each 24-hour dual-channel recording selected for the ACEDB, a six-hour window was chosen to include the event(s) appropriate to the class. Each six-hour window was digitized at 250 samples/second/channel. Each digitized record was saved in unfiltered and filtered (1-30 Hz digital convolution) form. The records are now being annotated with respect to clinical event type and event time of occurrence. Meanwhile, Biosensor plans to create a six-hour analog, Holter-style tape for each ACEDB record.

System developers and/or potential users wishing to evaluate a given system against the ACEDB may simply run either digital or analog data through their system and examine system reports as to the "clock time" for each clinical event detected (a virtually universal feature on all ambulatory ECG processing systems, regardless of architecture). Because the relationship between individual beats and clinical events is a "many-to-one" ratio, it is relatively easy to determine if a clinical event from the ACEDB was detected by the system, even if the times do not "line-up" exactly.

The advantages of such a database might thus be summarized as (1) enabling system developers to try their algorithms on longer records than those available with the AHA and MIT/BIH databases, (2) giving physician-users the means to evaluate detection performance of "clinical events" and (3) giving manufacturers of Holter systems the means to evaluate performance without the constraint of recording each beat's time of occurrence.

A-2. Argus Exportation

Personnel: K. W. Clark, BCL
C. N. Mead, Biosensor Corporation

Support: RR 01380
Biosensor Corporation
Dalhousie University

For three years, we have been working closely with Biosensor Corporation to help them evaluate their commercial implementation of the frequency-domain based Argus algorithm for high-speed ECG processing (VI, Industrial Collaboration). Biosensor markets a variety of systems and services oriented around the micro-processor-based portable real-time ECG analyzer. While BCL continues to evaluate the analyzer, Biosensor provides valuable feedback to BCL on the performance of the Argus algorithm in real-life, long-term situations.

Several years ago, we sent the time-domain-based Argus algorithm to Dalhousie University (Halifax, Nova Scotia). They have been using the algorithm in a Holter-tape processing environment ever since. Quite recently, we sent the frequency-domain-based algorithm (A-1) to Dalhousie; they are now evaluating that algorithm and how it might best be implemented in their environment.

A-3. Holter Tape Processing

Personnel: K. W. Clark, BCL

Support: Mead-Johnson

For two and one-half years, BCL has analyzed long-term (Holter) ECG recordings for a Mead-Johnson (Evansville, Indiana) sponsored "Multicenter Placebo-Controlled Study of Trazadone's Effects in Depressed Cardiac Patients" (PR 20, VI). The original ECG processing contract, due to expire in October, 1985, was extended indefinitely. Patient recruitment has fallen well short of projections, and Mead-Johnson is negotiating with the FDA for modifications to the Study plan. Meanwhile, Mead-Johnson has sent only 48 recordings (12 patients) since July, 1985.

A-4. Assessment of Vascular Integrity of the Myocardium Following Ischemic Injury

Personnel: R. G. Tilton, Ph.D., Pathology
R. A. Gardner, Ph.D., Mechanical Engineering
J. Howe, Pathology
K. B. Larson, BCL
J. Markham, BCL
S. P. Sutera, Ph.D., Mechanical Engineering
J. R. Williamson, M.D., Pathology

Support: RR 01380
HL 31531
The Kilo Diabetes and Vascular Research Foundation

We have continued our previously reported studies (PR 21, A-3) of the role of the endothelium in the pathogenesis of vascular hemodynamic and permeability changes associated with ischemia and reperfusion. In these studies, we employ external-detection techniques to quantify radiolabeled albumin transport across the coronary vasculature under physiological conditions, and during reperfusion after ischemia in isolated-perfused rabbit hearts. The resulting residue-detection data, analyzed on the basis of a two-compartment model of tracer transport, are used to estimate parameters indicative of microvascular integrity, such as permeability and ultrafiltration conductance of endothelium.

Using a modified, oxygenated Krebs-Henseleit buffer for perfusion under constant-flow conditions, we have demonstrated marked increases in vascular resistance and albumin permeation across the coronary vasculature during reperfusion after 30 minutes of ischemia while myocyte contractility recovered, and we have suggested that the increased vascular resistance is due, in part, to coronary vasoconstriction. During the past year, we have continued the studies reported in PR 21, A-3, and have tested, further, the hypothesis that if perfusion pressure is held constant, the flow rate would decline and left ventricle contractile function would not recover during reperfusion. No differences were evident during 5 hours of continuous perfusion in hearts perfused under non-ischemic conditions of constant flow or constant pressure; vascular resistance, LVEDP, maximum +dP/dt, vascular volume, the rate of intravascular clearance of albumin (k_{01}), the mean-transit time of albumin, and albumin permeation remained similar. During reperfusion after 30 minutes of no flow, perfusion pressure increased 43% in the constant-flow experiments and flow rate decreased 30% in the constant-pressure experiments; however, even though oxygen extraction from the perfusate was nearly complete in the low-flow condition, no differences were evident in LVEDP, maximum +dP/dt, k_{01}, or the mean-transit time of albumin during reperfusion in both groups of experiments. Vascular volume increased ~60% in the former experiments, but remained at baseline values in the latter experiments. Estimates of albumin permeability were increased ~5 X and 4 X baseline in the constant-flow and constant-pressure experiments, respectively. The observations that flow rate decreased by 30% during reperfusion in the constant-pressure experiments while left ventricle contractility recovered at the same rate as in the constant-flow experiments did not support our hypothesis that during reperfusion under conditions of constant pressure, the reduced flow rate would cause further deterioration of myocardial contractile function.

In view of the above findings, we have initiated additional constant-flow versus constant-pressure experiments using both sheep and bovine erythrocyte-enriched perfusates (at hematocrits of 25-40%). The rationale for these experiments, in addition to being more physiologic, is that the increased viscosity and decreased baseline flow rate of erythrocyte-enriched perfusates might enhance the decline in flow during reperfusion after ischemia. We have selected sheep and bovine erythrocytes in view of their substantial difference in mean cell volume.

In additional studies, we are investigating the mechanism whereby albumin interacts with walls of capillaries to maintain normal permeability characteristics. In these experiments, we perfuse hearts with buffer containing 1% albumin during baseline, then switch to albumin-free perfusate. Removing albumin from the perfusate has no effect on vascular resistance, LVEDP, maximum +dP/dt, vascular volume, of k_{01}, while albumin permeation increases ~3 fold (which returns to control levels when albumin is reintroduced). These results support the hypothesis that albumin forms an integral part of the capillary molecular filter. Experiments are in progress to assess the specificity of the plasma protein for maintaining normal capillary permeability characteristics.

A-5. Electrophysiological and Biochemical Factors Underlying the Genesis of Arrhythmias Due to Myocardial Ischemia and Infarction

Personnel: P. B. Corr, Ph.D., Medicine and Pharmacology
A. G. Davis, M.D., Medicine
S. M. Moore, BCL
S. M. Pogwizd, M.D., Medicine
B. E. Sobel, M.D., Medicine
K. A. Yamada, Ph.D., Medicine

Support: HL 28995
HL 17646
AHA 81-108

The overall concept of the research is that potential arrhythmogenic metabolites accumulate in ischemic tissue and exert deleterious effects on membranes and that their effects may be exacerbated by the concomitant influences of the adrenergic nervous system. Over the past several years, studies have been completed demonstrating a major electrophysiologic role of α-adrenergic stimulation during myocardial ischemia as well as reperfusion. In addition, it has been demonstrated using radioligand binding procedures that there is a reversible increase in α_1-adrenergic binding sites in ischemic and reperfused myocardium. More recently, we have demonstrated that α-adrenergic blockade specifically attenuates the increase in intracellular calcium associated with reperfusion in reversibly injured tissue [1]. Studies performed in our laboratory have also indicated that lysophosphatides, including lysophosphatidylcholine (LPC) and ethanolamine (LPE) accumulate in ischemic myocardium in situ and have been implicated as potential mediators of arrhythmogenesis in the ischemic heart [2].

Alpha-adrenergic blockade immediately prior to reperfusion attenuates the reperfusion-induced increases in intracellular Ca^{++} and mitochondrial dysfunction. Likewise, the α_1-adrenergic blocking agent hydroxyethyl aminomethyl tetralone (HEAT, 50 μg/kg) given just prior to reperfusion reduces the extent of cellular necrosis measured two days later from 31 to 14% of the left ventricle without altering hemodynamic parameters. To determine whether salvage is dependent on an increase in myocardial blood flow (BF), radiolabeled microspheres (^{141}Ce, ^{51}Cr, ^{85}Sr, ^{46}Sc) were injected into the left atria of chloralose-anesthetized cats subjected to left anterior descending (LAD) coronary artery occlusion and reperfusion. Hearts were sectioned into multiple (10 to 46) endocardial (endo) and epicardial (epi) samples. Control BF was 2.3 ± 0.2 ml/min/g. HEAT (50 μg/kg) given just prior to reperfusion reduced BF in the ischemic zone measured 5 min, 20 min and 48 hr after reperfusion by 20, 22 and 16%, respectively, compared to untreated animals. The endo/epi BF was identical in both the treated and untreated groups (1.2 ± 0.2 and 1.2 ± 0.1). Thus, enhanced salvage by α_1-adrenergic blockade immediately prior to reperfusion is not attributable to an increase in BF but to direct effects on myocardial α_1-adrenoceptors and attenuation of intracellular accumulation of Ca^{++}.

Several years ago, we demonstrated that ischemia is associated with a two-fold increase in myocardial α_1-adrenergic receptors. Hypoxia in isolated myocytes results in increased sarcolemmal (SL) accumulation of long chain acylcarnitines (LCA). Inhibition of carnitine acyltransferase I with sodium 2-[5-(4-chlorophenyl)-pentyl]-oxirane-2-carboxylate (POCA, 10 μM) prevents the increase in LCA during hypoxia and the associated electrophysiologic derangements [3]. To determine whether accumulation of LCA by SL with hypoxia exposes α_1-adrenergic receptors measured with ^3H-prazosin, isolated adult canine myocytes separated with collagenase and a BSA-percoll gradient were utilized. Hypoxia (100% N_2) for 30 min resulted in a greater than two-fold increase in α_1-adrenergic receptor number with no loss of cell viability (1.9 ± 0.2 to 5.4 ± 0.7 fmol/mg protein, n=15, $p<.01$) and no significant change in receptor affinity (K_D = 0.30 to 0.57 nM). Pretreatment with POCA (10 μM) to inhibit SL accumulation of LCA, prevented the increase in receptor number (2.3 ± 0.5 fmol/mg protein, n=9). Prolonged hypoxia (80 min, which decreased cell viability) or lysis of cells with hypotonic HEPES buffer decreased receptor number (1.1 ± 0.4 fmol/mg protein). Thus, increased α_1-receptor density induced by hypoxia results, at least in part, from accumulation of LCA in the SL. Future plans include assessment of the active and passive membrane alterations induced by stimulation of this exposed α_1-adrenergic receptor on adult myocytes, as well as assessment of the influence of stimulation on alterations in cytosolic Ca^{++} utilizing the intracellular dye, quin-2.

We and others have shown that LPC increases in tissue samples and venular effluents from ischemic hearts and in lymph draining ischemic myocardium in vivo [4]. However, intracellular LPC in vitro does not result in electrophysiologic (EP) derangements analogous to those seen with extracellular exposure [4]. To determine whether the extracellular [LPC] observed in lymph after ischemia is sufficient to induce EP changes, we evaluated the effects of LPC in simulated lymph (200 μM albumin + 515 μM palmitate in Krebs) on isolated adult canine myocytes with intracellular microelectrode recordings. The protein profile of canine lymph was determined by electrophoresis. The concentration of LPC in lymph from ischemic zones in vivo, 200 μM, at pH 6.7, reduced resting membrane

potential (RMP) from -87 ± 1 to -73 ± 4 mV, $\dot{V}_{max}$ from 150 ± 7 to 76 ± 15 V/sec and APD_{95} from 293 ± 17 to 203 ± 32 ms. In contrast, the concentration of LPC in control lymph in vivo, 85 μM, even at pH 6.7, had EP effects no different from those of simulated lymph alone. Thus, increased [LPC] in lymph draining ischemic myocardium is sufficient to induce EP alterations. Future studies will be directed toward modulating the increase in LPC in ischemic lymph in vivo with inhibitors of phospholipase A_2 with concomitant assessment of the intervention on arrhythmogenesis and regional electrophysiologic alterations in the ischemic heart.

Extensive studies were performed to assess the effects of POCA with ischemia in vivo induced by five-minute occlusion of the LAD coronary artery in chloralose-anesthetized cats (n=15). To verify inhibition of LCA accumulation by POCA, transmural biopsies were obtained simultaneously from the normal (NZ) and ischemic zone (IZ) and carnitines in acid extracts were measured radioenzymatically. Ischemia elicited a 3-fold increase of LCA in the IZ (0.31 ± .07 nmol/mg protein) compared to sham animals (0.10 ± .03 P<.001) or to the NZ in ischemic hearts (0.18 ± .03, P<.01). Ventricular tachycardia (VT) and fibrillation (VF) occurred in 55% of control animals. POCA (7.3 mg/kg) prevented the increase of LCA (0.04 ± .01, IZ and 0.05 ± .01, NZ) and prevented both VT and VF. Thus, inhibition of accumulation of LCA in ischemic myocardium is profoundly antifibrillatory. Studies are now underway to assess the effect of POCA on the regional conduction delay in the ischemic zone in vivo as well as to determine the extent of SL accumulation of LCA during ischemia in vivo using autoradiography in hearts prelabeled with ^{3}H-carnitine.

Mechanisms underlying VF were evaluated with a three-dimensional mapping system permitting 8-level transmural recording from 232 simultaneous sites [5]. Ischemia was induced for 10 min by LAD coronary occlusion, followed by reperfusion in the chloralose-anesthetized cat. VT leading to VF and nonsustained VT were both initiated in the subendocardium (endo) by a non-re-entrant mechanism (n=11 runs). There were no significant differences in the coupling interval of the initiating beat or the delay in total activation time between VT which lead to VF vs nonsustained VT (199 ± 16 vs 189 ±9 ms and 97 ± 5 vs 89 ± 5 ms, respectively). In contrast, VT leading to VF was due to a rapidly accelerating non-re-entrant mechanism from the endo or epicardium (epi). When the cycle length of VT leading to VF became < 120 ms, very rapid non-re-entrant endo activation occurred with a cycle length of 92 ± 2 ms, leading to enhanced functional block with total activation time exceeding the non-re-entrant cycle length, resulting in disorganization of activation and VF. None of the nonsustained VTs exhibited non-re-entrant activity in the epi, or cycle lengths < 120 ms leading to very rapid endo activation. Thus, VF after reperfusion is due to rapid, nonre-entrant acceleration of rate that elicits even faster endo activation.

1. Sharma, A. D., Saffitz, J. E., Lee, B. I., Sobel, B. E., and Corr, P. B., "Alpha-Adrenergic Mediated Accumulation of Calcium in Reperfused Myocardium," Journal of Clinical Investigation, vol. 72, pp. 8802-8818, 1983.

2. Corr, P. B., Gross, R. W., and Sobel, B. E., "Amphipathic Metabolites and Membrane Dysfunction in Ischemic Myocardium," Invited review for Circulation Research, vol. 55, pp. 135-154, 1984.

3. Knabb, M. T., Saffitz, J. E., Corr, P. B., and Sobel, B. E., "The Dependence of Electrophysiologic Derangements on Accumulation of Endogenous Long-Chain Acyl Carnitine in Hypoxic Neonatal Rat Myocytes," Circulation Research, vol. 58, pp. 230-240, 1986.

4. Akita, H., Creer, M. H., Yamada, K. A., Sobel, B. E., and Corr, P. B., "Electrophysiologic Effects of Intracellular Lysophosphoglycerides and Their Accumulation in Cardiac Lymph with Myocardial Ischemia in Dogs," Journal of Clinical Investigation, vol. 78, pp. 271-280, 1986.

5. Witkowski, F. X. and Corr, P. B., "An Automated Simultaneous Transmural Cardiac Mapping System," American Journal of Physiology (Heart and Circulatory Physiology), vol. 247, pp. H661-H668, 1984.

A-6. Research Projects Utilizing the Isolated Probe Data Acquisition System

Personnel: S. R. Bergmann, M.D., Ph.D., Medicine
H. D. Ambos, Medicine
D. E. Beecher, BCL
M. A. Brown, M.D., Medicine
T. L. Rosamond, M.D., Medicine
B. E. Sobel, M.D., Medicine

Support: RR 01380
HL 13851
HL 17646

The research in this project is designed to define the kinetics of positron-emitting radiotracers that are potentially useful for the non-invasive characterization of myocardial perfusion and metabolism. Studies in this project are conducted in isolated rabbit hearts perfused with a modified Krebs-Henseleit buffer, and in open-chest dogs with controlled, extracorporeal circulation. Both of these animal preparations have been used extensively in our laboratories to develop approaches of proven value in studies using positron-emission tomography. The development of accurate, quantitative, noninvasive measurements of myocardial metabolism and perfusion are dependent on the characterization of the factors that can influence tracer kinetics.

We have previously shown that clearance of 1-^{11}C-palmitate reflects oxidative metabolism when flow and arterial oxygen content are normal. During either ischemia or hypoxia, we demonstrated that labeled unmetabolized palmitate "back-diffuses" from the myocardium. Therefore, estimates of oxidative capacity based on clearance of tracer from the heart during ischemia would tend to overestimate the oxidative capacity. To further study this relationship, the fates of 1-^{11}C- and 1-^{14}C-palmitate were studied in 13 open-chest dogs during control or ischemic

extracorporeal perfusion of the left circumflex coronary artery. Residue detection of myocardial radioactivity with the isolated-probe data-acquisition system and radio-biochemical analyses of sequential transmural biopsies and arterial and coronary venous effluent were performed for 30 minutes after intracoronary bolus injection of tracer. In control hearts, 10.3% of the initial extracted tracer was retained in tissue, 73.7% was oxidized, and 16.1% back-diffused unaltered. With ischemia, 28.1% was retained, 27.2% was oxidized, and 44.4% back-diffused ($p < 0.05$ compared to control). Throughout the 30-minute study, triglyceride, diglyceride, and non-esterified fatty acid comprised a significantly greater fraction of initially extracted radioactivity in ischemic than in control hearts. We thus conclude that during ischemia, externally detected clearance rates cannot be used as a direct measure of fatty acid metabolism because of the marked influences of efflux of non-metabolized radiolabeled palmitate and the distribution of tracer retained in the tissue. Quantitative measurements of specific metabolic processes by tomography would thus require development and validation of tracers confined to individual metabolic pathways or pools.

To assess one such tracer, we evaluated the assessment of myocardial oxidative capacity with radiolabeled acetate. Because metabolism of acetate is virtually exclusively oxidative, we used it to define viability of myocardium rendered transiently ischemic in isolated rabbit hearts perfused retrogradely with the modified Krebs-Henseleit buffer. Extraction fraction averaged 56.4 ± 4.5% in six control hearts perfused at 20 ml/min and increased to 67.9 ± 4.8% with ischemia (flow = 2 ml/min, n=5). The $t_{1/2}$ for clearance of total and $^{14}CO_2$ radioactivity averaged 4.1 ± 1.3 and 4.2 ± 1.3 minutes in controls (n=11); 18.9 ± 11.7 and 15.8 ± 4.5 with ischemia (n=12); and 3.4 ± 0.1 and 3.4 ± 0.2 with 60 minutes of ischemia followed by reperfusion (n=5). MVO_2 correlated closely with clearance of total and $^{14}CO_2$ radio-activity (r=0.90 and 0.92, $p<.001$ for each). Clearance of ^{11}C-acetate, detected externally with the isolated-probe data-acquisition system correlated closely with that of ^{14}C-acetate (r=0.99). Thus use of ^{11}C-acetate is a promising approach for delineation of myocardial oxidative capacity and hence viability after ischemia and reperfusion.

The studies performed in the laboratory using the isolated-probe data-acquisition system during the past year with ^{11}C-palmitate and ^{11}C-acetate have permitted a better understanding of the factors that influence the uptake of these tracers, and allowed delineation of the limitation of the use of ^{11}C-palmitate in the context of ischemia and reperfusion. We will continue in the coming year to study the usefulness of ^{11}C-acetate, with its simpler metabolic pathway, as a potential tracer for assessment of the oxidative capacity of myocardium. Clarification of the kinetics of these tracers under controlled laboratory conditions should enhance the understanding of the tomographic data that is acquired in our studies with experimental animals (D-1) as well as studies utilizing positron-emission tomography in humans (D-2).

A-7. Analysis of Plasma CK Isoforms

Personnel: D. R. Abendschein, Ph.D., Medicine
J. J. Billadello, M.D., Medicine
S. R. Devries, M.D., Medicine
A. S. Jaffe, M.D., Medicine
J. Markham, BCL
B. E. Sobel, M.D., Medicine
A. W. Strauss, M.D., Pediatrics

Support: HL 17646

Early and reliable detection of acute myocardial infarction and myocardial reperfusion are important for timely initiation of therapy and evaluation of the efficacy of therapy. We have shown previously that post-translational modification of creatine kinase (CK) MM isoenzyme released from myocardium, MM_A, to two additional isoenzyme subforms (isoforms), MM_B and MM_C, in plasma permits prompt detection of infarction in dogs subjected to coronary artery occlusion [1]. Because of continuous elimination of circulating MM_A (*via* conversion to MM_B and MM_C and clearance from blood), the proportions of isoforms in plasma are altered markedly by egress of small amounts of MM_A from myocardium, often in the absence of a measurable change in total CK activity. Thus, changes in plasma isoform proportions indicative of recent enzyme release from tissue occur very early after the onset of ischemia and are more sensitive to early myocardial damage than total CK activity in plasma.

In the past year, we have extended these observations to include analysis of CK isoforms in patients admitted to Barnes Hospital with suspected acute myocardial infarction. We found that in the first blood sample, usually obtained within 2 to 3 hours of the onset of clinical symptoms, the ratio of tissue isoform (MM_A) to the second modified isoform (MM_C) was markedly elevated in patients with myocardial infarction (verified retrospectively) compared to groups of normal controls and patients with unstable angina [2]. In many of the patients with increased MM_A:MM_C ratios, the total CK activity in plasma was still within accepted normal limits.

We have also completed a study showing that the fraction of total CK activity in plasma represented by MM_A (MM_A%) changes very early after the onset of myocardial reperfusion in conscious dogs [3]. The rate of change of MM_A% in plasma during the first 30 minutes of reperfusion after 1, 2 or 3 hours of ischemia was remarkably consistent and significantly faster than the rate in the absence of reperfusion regardless of the magnitude of absolute plasma CK activity or infarct size. Thus, analysis of changes in MM_A% in plasma may provide an early and reliable index of myocardial reperfusion.

We are currently investigating isoform changes in dogs during reperfusion through a high-grade stenosis of the coronary artery to determine if the extent of coronary reflow affects the isoform profiles in plasma. A clinical study is also in progress to evaluate isoform changes in patients receiving thrombolytic therapy.

Recent evidence indicates that reperfusion salvages ischemic myocardium when initiated within several hours of the onset of ischemia, but may exacerbate tissue damage if it is initiated late in the course of infarction. Accordingly, it is important to know the approximate duration of ischemia before reperfusion therapy is administered. Improved understanding of the kinetics of isoform conversion and elimination from the circulation may permit timing of the onset of enzyme release from myocardium by analysis of isoform profiles in plasma.

In the past year we have conducted experiments to characterize the mechanism of isoform formation in plasma. We recently reported that MM_A is converted to MM_B and MM_C by successive removal of the COOH-terminal lysine residue from one M subunit at a time [4]. We have also shown that the isoform conversion enzyme in plasma is carboxypeptidase N [5] and that the rate of isoform conversion is directly related to the plasma level of carboxypeptidase N. Preliminary data indicate that the level of carboxypeptidase N in plasma varies widely among normal dogs and patients and increases during the course of infarction. Thus, measurement of carboxypeptidase N levels in plasma will be important to define the time course of isoform conversion in vivo.

Additional experiments are planned to assess the individual clearances of isoforms in vivo. Purified isoforms will be injected intravenously in conscious dogs in the presence of a specific inhibitor of carboxypeptidase N so that clearance of isoforms in the absence of simultaneous conversion may be assessed. These results, in conjunction with additional studies of changes in carboxypeptidase levels in plasma, will permit development of a physiologic model of isoform kinetics in vivo. This model can then be employed to estimate the time of enzyme release from myocardium based upon the profiles of isoforms in plasma samples.

1. Hashimoto, H., Abendschein, D. R., Strauss, A. W., and Sobel, B. E., "Early Detection of Myocardial Infarction in Conscious Dogs by Analysis of Plasma MM Creatine Kinase Isoforms," Circulation, vol. 71, pp. 363-369, 1985.

2. Jaffe, A. S., Serota, H., Grace, A. M., and Sobel, B. E., "Diagnostic Changes in Plasma Creatine Kinase Isoforms Early After Onset of Acute Myocardial Infarction," Circulation, vol. 74, pp. 105-109, 1986.

3. Devries, S. R., Sobel, B. E., and Abendschein, D. R., "Early Detection of Myocardial Reperfusion by Assay of Plasma MM Creatine Kinase Isoforms in Dogs," Circulation, in press.

4. Billadello, J. J., Roman, D. G., Grace, A. M., Sobel, B. E., and Strauss, A. W., "The Nature of Post-Translational Formation of MM Creatine Kinase Isoforms," Journal of Biological Chemistry, vol. 260, pp. 14988-14992, 1985.

5. Abendschein, D., Plummer, T., Devries, S., Grace, A., Sobel, B. and Strauss, A., "MM Creatine Kinase Conversion Factor in Human Plasma is Carboxypeptidase N," Federation Proceedings, vol. 45, p. 560, 1986 (abstract).

A-8. SCOR Patient Information Database

Personnel: H. D. Ambos, Medicine
A. S. Jaffe, M.D., Medicine
J. Markham, BCL
K. B. Schechtman, BCL
B. E. Sobel, M.D., Medicine

Support: RR 01380
HL 17646

In the past year the Specialized Center for Research (SCOR) database was implemented on a DEC PRO-380 system configured with a 30 megabyte Winchester disc and dual floppy disc drives. The system runs under POS, a menu driven operating system.

Each SCOR project has its own specialized data entry forms which were created using the Responsive Data Manager (RDM) software. This is a data-entry and report-generating system which allows customization of data entry forms and final reports. Once data are entered, they can be analyzed via RS/1, a data-analysis system incorporating statistics and graphics. All data analysis and management facilities are interactive.

The database currently contains information on more than 3000 patients with documented coronary artery disease or who have suffered acute myocardial infarction. Studies which have utilized the SCOR database include an analysis of changes in plasma creatine kinase isoforms early after the onset of acute myocardial infarction; a study of the relationship between apoproteins and the severity of coronary artery disease; a consideration of the association between the continued activation of thrombin reflected by fibrinopeptide A and the efficacy of thrombolysis; an application of radionuclide ventriculography to determine the age dependence of diastolic function and to evaluate the association of other factors with diastolic performance; and a study which utilized fast-Fourier transforms of signal-averaged electrocardiograms to determine if frequency analysis detects patients in whom sustained ventricular tachycardia might be induced.

A-9. Software Support for Cardiological Processing

Personnel: D. E. Beecher, BCL
W. H. Hellberg, BCL

Support: RR 01380
HL 17646

The software system designed for cardiological image processing (PR 21, A-11) has been in routine use over the past year. This year's efforts have centered around the recently acquired QMS model 800 Laser Printer which was purchased to replace the obsolete Versatec printer/plotter. The laser printer has powerful printing and plotting capabilities, however this system has very little support software on the PE 3230 mainframe which drives it and Super PETT I. A system (QPRINT) was developed which allows users to easily access the printing capability of the QMS (font selection, justification, cpi, lpi, margin control, etc.) which translates user-supplied "English" commands and command files into "machine" commands understood by the laser printer. Essential data about the QMS character fonts are stored and processed as text files that can be rapidly modified as the QMS hardware is upgraded or changed. This processing system also includes an on-line, menu-driven user's guide to the QPRINT utility. Future enhancements will include a menu-driven, interactive command-generator within QPRINT. A subroutine library to utilize the plotting capability of the QMS was also designed and implemented for generating hardcopy plots of PETT images and plots of various types of PETT data.

B. Quantitative Imaging: Ultrasonic Tissue Characterization

Although ultrasound has proven to be a useful source of diagnostic information, results of examinations based on current ultrasonic methods are primarily qualitative and pictorial. In a collaborative effort with Cardiology and the Department of Physics work has continued on methods of tissue characterization via ultrasound. Our overall goal is to use ultrasound for the noninvasive identification of tissue pathologies within two-dimensional images of tissue properties. Specific objectives of this effort are 1) to investigate the magnitude and character of anisotropy in tissue, 2) to systematize the representation of the ultrasonic field and to reduce the data needed to describe that field by determining the moments of the spatial distribution of energy over the receiver aperture, 3) to seek improvement in measurement capability of imaging systems via interactive, adaptive beamforming for both linear and variable-aperture transducer arrays, 4) to test the hypothesis that quantitative images based on intrinsic tissue properties can be produced with reflected ultrasound, and 5) to construct a digital multiprocessor system to perform post-echo ultrasonic estimation of attenuation, phase velocity and backscatter in two dimensions.

Our investigation of spatial moments of the received field was extended in three studies conducted over the past year. We demonstrated the phase-cancellation insensitivity of a pseudo-array of 1 mm elements compared to a 12.7 mm circular transducer in measurements of attenuation, centroid shift, and beam broadening (B-1). We generalized the theory of moments from two to N dimensions as a framework for future applications (B-2). In addition the effects of noise on moments values was assessed in terms of the mean and variance of the noise (B-3).

Quantitative images based on ultrasonic tissue properties have been made at the BCL for several years using transmitted ultrasound with a multiple-frequency tomographic reconstruction system. We are now able to reconstruct tomograms with reflected ultrasound using the complete dataset (B-4). At present, reconstruction is off-line, but we are developing, for real-time operation, a VLSI implementation of an algorithm for mapping a given pixel of a backscattered signal into the tomogram. The effects of the transducers have also been studied. The frequency and angular responses of elements in the linear arrays of the tomographic system were measured and the disturbance at the aperture inferred as a method for assessing and correcting for diffraction effects (B-5).

Two additions were made to the processing environment for ultrasonic tissue characterization (B-6). A disk drive for image storage and an Ethernet controller are now part of our image-processing workstation.

B-1. Transmission Measurements Using a Phase-Insensitive Two-Dimensional Pseudo-Array and the Method of Spatial Moments

Personnel: P. H. Johnston, BCL
J. G. Mottley, BCL
J. G. Miller, BCL

Support: RR 01362
HL 17646
HL 28998

Although the primary emphasis in clinical applications of ultrasound rests on backscattering, many studies designed to investigate the underlying basis for ultrasonic tissue characterization are better performed using transmitted ultrasound. In this section we demonstrate the phase-insensitivity of the pseudo-array approach in measurements of a sample exhibiting a "worst-case" condition for phase-cancellation. We then present a series of results obtained in experiments using a two-dimensional receiving pseudo-array in transmission-mode.

Phase-Insensitive Detection Using a Two-Dimensional Pseudo-Array

Phase cancellation over the face of a piezoelectric receiver results whenever the incident wavefronts are not parallel with the receiver face. Range, and thus phase, differences between all points on a receiver and a point source of sound in a homogeneous medium result in a specific phase cancellation effect, i.e. the directivity of the receiver. Further, variations in the index of refraction in a medium can produce phase variations in the ultrasonic field which may cause additional phase-cancellation losses at the receiver. The errors resulting from phase-cancellation represent a problem in measurements where the electrical energy developed by the receiving transducer is assumed to represent the incident ultrasonic energy. In fact conditions exist in which a receiving transducer registers a null voltage output despite a substantial energy flux incident on its face. For example, such a "worst-case" situation can exist as an ultrasonic field propagates through the edge of an organ or specimen which exhibits a different speed of sound from the media surrounding it. This sharp discontinuity in acoustic properties produces a corresponding distortion of the propagating waves which then may produce a completely null response when detected by a phase-sensitive receiver. This effect is well-known in the field of ultrasonic transmission tomography [1-5].

In order to demonstrate the phase-insensitive nature of the two-dimensional receiving pseudo-array, we experimentally prepared a "worst-case" condition for phase-cancellation based on an approach developed by Busse and Miller [6]. Our experimental arrangement is depicted in Figure 1. A planar broadband transmitting transducer was mounted coaxially with a receiving transducer or pseudo-array. Using a broadband substitution technique we performed transmission measurements of attenuation at three sites in a plexiglass specimen prepared with a step discontinuity in thickness. At positions (i) and (iii) the wavefronts of the transmitted beam passed undistorted through the plane-parallel plate and were received. At position (ii), however, the discontinuity in thickness resulted in a discontinuity in the wavefronts, the aforementioned "worst-case" condition

for phase-cancellation. Measurements were made at sites (i), (ii), and (iii) using both a phase-sensitive transducer and a phase-insensitive two-dimensional pseudo-array.

The signal loss as a function of frequency measured through the stepped plexiglass plate using phase-sensitive and phase-insensitive detection is presented in Figure 2. The results of phase-sensitive detection using a 12.7 mm diameter planar piezoelectric receiving transducer are plotted in panel (a). The loss measured at positions (i) and (iii), where the surfaces of the plate were parallel, exhibits a linear dependence on frequency. The loss measured at position (ii), where the transmitted beam was centered on the discontinuity of thickness in the plate, exhibits a scalloped frequency-dependence. The discontinuity of phase caused by the thickness discontinuity represented a varying fraction of a period as a function of frequency, resulting in a varying degree of partial cancellation over the frequency spectrum. At approximately 5 MHz, where the phase discontinuity represented an odd number of half-cycles, the loss was more than 20 dB greater at position (ii) than at the other positions. This behavior is indicative of the nearly complete cancellation of signal by integration at the face of the receiver of those wavefronts which passed through the thicker portion of the plate with those which passed through the thinner portion.

Subsequent to acquiring a phase-sensitive spectrum at each site, the receiving transducer was fitted with an aperture plate having a 1 mm diameter aperture. The resulting small-diameter receiver served as the receiving element of a phase-insensitive two-dimensional pseudo-array. The pseudo-array was employed to measure the ultrasonic field over the same two-dimensional region sampled by the unapodized transducer. The zeroth-order two-dimensional spatial moment of the received signal was calculated as a function of frequency and loss was determined by comparison with the zeroth moment measured in the absence of the specimen. The resulting loss curves are presented in panel (b) of Figure 2. We note that at all three sites the measured loss exhibits smooth nearly-linear behavior with frequency. The cancellation exhibited in the phase-sensitively detected loss at position (ii) is eliminated.

Attenuation Measurements Using Phase-Insensitive Pseudo-Array

A measurement of the attenuation coefficient of a sample using the zeroth spatial moment is presented in Figure 3. The solid curve in the upper panel represents the zeroth-order moment measured for a transmitted beam in a water-only path as a function of frequency. A series of plates of thicknesses 3, 4, 5, 6, 7, 8, 9, and 10 mm were constructed from a larger sheet of plexiglass. Each of these plates was mounted normal to the interrogating beam in front of the receiving pseudo-array. The measured zeroth-order moments for the 5 mm and the 10 mm specimens are presented in the upper panel of Figure 3. The attenuation coefficient for plexiglass could be determined by comparing each of the spectra measured with a specimen in place with that measured with only a water path. Because measurements were performed for several thicknesses of plexiglass in this experiment, we were able to take a slightly altered approach. We fit a straight line to the zeroth moment as a function of sample thickness at each frequency to obtain the attenuation coefficient values plotted in the lower panel of Figure 3. The attenuation coefficient for plexiglass is observed to exhibit linear dependence on frequency with a slope of

attenuation β equal to (mean ± standard deviation) 0.68 ± 0.05 dB/cm-MHz. Although the properties of plastics differ somewhat from batch to batch, this value is comparable to a published value for plexiglass of 0.77 ± 0.12 dB/cm-MHz [7].

In addition to the plastic specimens, we measured the attenuation of tissue-mimicking phantoms constructed of several concentrations of graphite powder in gelatin and of glass beads in gelatin. Fabrication of these phantoms followed the techniques outlined by Madsen et al. [8]. The slope of attenuation with respect to frequency for these specimens is presented in Figure 4 as a function of concentration. The results for graphite-in-gelatin phantoms are given in panel (a). Similarly, in panel (b) we present our results for glass beads in gelatin. In both sets of data the slope of attenuation varies linearly with concentration of inclusions in accordance with the results from Insana et al. [9].

Centroid Shift

In order to evaluate the sensitivity of the moments approach to small shifts, a set of measurements were performed in which the position of the pseudo-array was changed relative to a fixed transmitter and the coordinates of the centroid of the energy in the transmitted beam were determined at each receiver location. The results of two runs from this series are presented in Figure 5. In panel (a) are the results of an experiment in which both the horizontal and vertical positions of the receiver were altered. The target positions are indicated by open circles. Measured values of centroid are indicated by asterisks. Beginning with the pseudo-array centered on the beam, the receiver was moved in increments of (0.2, 0.1) mm to a position (1.0, 0.5) mm from the start. Then the step size was increased to (1.0, 0.5) mm for three more sites. In this run, performed using narrow-band detection at a frequency of 5 MHz, the measured centroids match the target positions to within less than one tenth of one millimeter.

In a second run, in which only the horizontal position was varied, broadband measurements were performed and the centroids determined at all frequencies within the useful bandwidth averaged. Those results are presented in panel (b) of Figure 5. The increment between sites in this run was initially 0.1 mm and was increased to 0.5 mm as seen in the figure. [Note that the horizontal scales differ by a factor of two between panel (a) and panel (b).] The excellent agreement of these centroid values with the target values suggests that a broadband measurement with subsequent average over frequency may provide an improved measure of the centroid of a beam relative to narrowband measurements.

Beam Broadening by Plexiglass Plates

As a final demonstration of transmission measurements using a phase-insensitive receiving pseudo-array, we examine the effects on beam width of propagation through plates of plexiglass and polyethylene. In panel (a) of Figure 6 we present a schematic diagram of a transmitting transducer and a coaxial receiving two-dimensional pseudo-array. In the far field of the transmitting transducer, the beam diverges linearly with range. When a plate of material exhibiting a greater speed of sound than water is placed in the far field of the transmitter at range R, as depicted in panel (b), we expect the diverging beam to be broadened by passage through the plate. We performed an investigation to demonstrate this effect.

We first investigated the behavior of the transmitted beam in the absence of a specimen. In panel (a) of Figure 7, we present the zeroth-order moment measured using a two-dimensional receiving pseudo-array as a function of axial range in the far field of a 6.35 mm diameter broadband planar transmitting transducer. Zeroth moments for ultrasonic frequencies 3.5, 5.5, and 7.5 MHz are plotted as open circles, squares, and triangles, respectively. The beam widths determined from the same measurements are plotted in panel (b). The linear divergence of beam width with range is evident in the data. Because the beam width increases linearly with range, the effective area covered by the beam increases as the square of the range. This Z^2 dependence of beam area couples with the Z^{-2} dependence of the magnitude of the energy in the beam to yield a constant value of the zeroth moment as shown in panel (a).

The zeroth moment and beam width measured with a 10 mm thick plate of plexiglass in the beam path are presented as the filled symbols in Figure 7. The zeroth moment measured at three ranges with the specimen present, although attenuated, appears to exhibit the same independence of range observed in the water alone. The beam width after propagation through the plate is slightly larger in magnitude than in water only, but appears to diverge at the same axial rate. The range-independence of the zeroth moment suggests that the exact position of the receiving array relative to the specimen is not critical for attenuation measurements.

The broadening of a transmitted ultrasonic beam due to propagation through plastic plates of varying thickness is presented in Figure 8. The beam width measured at fixed range with different thicknesses of plexiglass positioned in the beam path are plotted as squares. The results for polyethylene plates are plotted as circles. Values measured in the absence of plastic plates are plotted as zero thickness. Least-square fit lines are drawn for both sets of data. We note that the refractive effect of propagation through these faster-than-water plastics resulted in broader beam width in proportion to the thickness of plastic traversed.

Summary

We have shown in this section that phase-insensitive two-dimensional pseudo-arrays can be used to give improved performance in detecting spatially distorted fields. Because of the two-dimensional sampling, additional information can also be extracted when the field takes on a special form, such as a transmitted beam.

1. Carson, P. L., Oughton, T. V., and Hendee, W. R., "Ultrasound Transaxial Tomography by Reconstruction," Ultrasound in Medicine, vol. 2, pp. 391-400, 1976.

2. Greenleaf, J. F., Johnson, S. A., Bahn, R. C., and Rajagopalan, B., "Quantitative Cross-Sectional Imaging of Ultrasound Parameters," Proceedings 1977 IEEE Ultrasonics Symposium, IEEE Catalog No. 77 CH 1264-ISU), pp. 989-995, 1977.

3. Glover, G. H. and Sharp, J. C. "Reconstruction of Ultrasound Propagation Speed Distributions in Soft Tissue: Time-of-Flight Tomography," IEEE Transactions on Sonics & Ultrasonics, vol. SU-24, pp. 229-234, 1977.

4. Dines, K. A. and Kak, A. C., "Ultrasonic Attenuation Tomography of Soft Tissues," Ultrasonic Imaging, vol. 1, pp. 16-33, 1979.

5. Pan, K. M. and Liu, C. N., "Tomographic Reconstruction of Ultrasonic Attenuation with Correction for Refractive Errors," IBM Journal of Research and Developmeent, vol. 25, pp. 71-82, 1981.

6. Busse, L. J. and Miller, J. G., "Detection of Spatially Nonuniform Ultrasonic Radiation With Phase Sensitive (Piezoelectric) and Phase Insensitive (Acoustoelectric) Receivers," Journal of the Acoustical Society of America, vol. 70, pp. 1377-1386, 1981.

7. Hung, B-N. and Goldstein, A., "Acoustic Parameters of Commercial Plastics," IEEE Transactions on Sonics and Ultrasonics, vol. SU-30, pp. 249-254, 1983.

8. Madsen, E. L., Zagzebski, J. A., Banjavic, R. A., and Jutila, R. E., "Tissue Mimicking Materials for Ultrasound Phantoms," Medical Physics, vol. 5, pp. 391-394, 1978.

9. Insana, M., Zagzebski, J., and Madsen, E., "Acoustic Backscattering From Ultrasonically Tissuelike Media," Medical Physics, vol. 9, pp. 848-855, 1982.

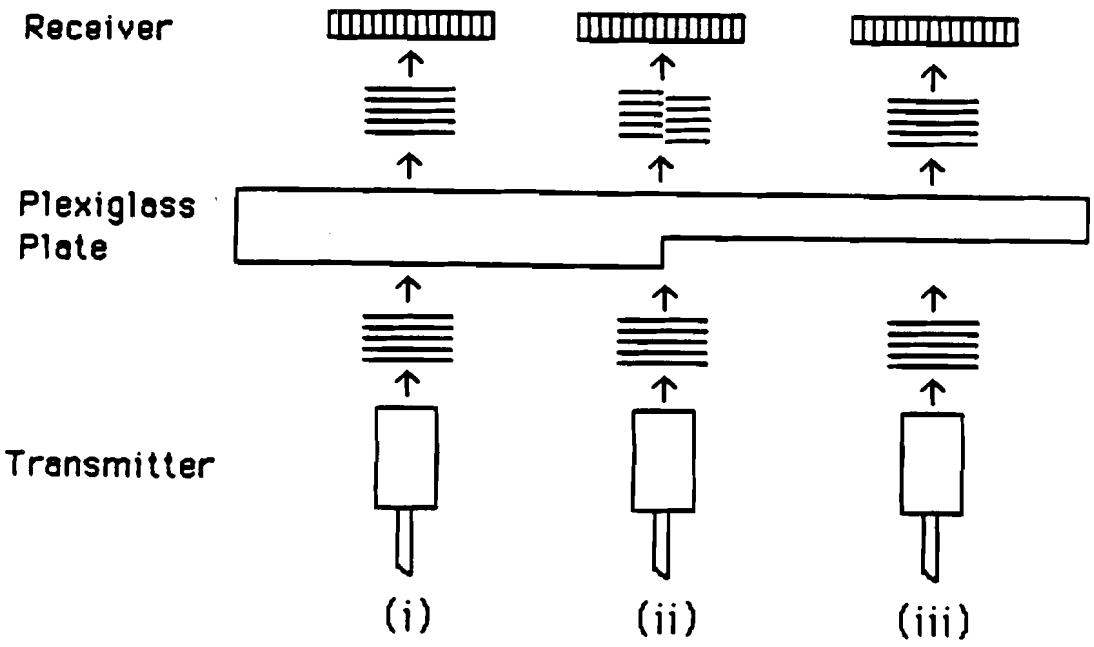

Figure 1. Stepped plate experiment. The transmitted waves at positions (i) and (iii) are received undistorted. The discontinuity in thickness at position (ii) produces distortion of the wavefronts.

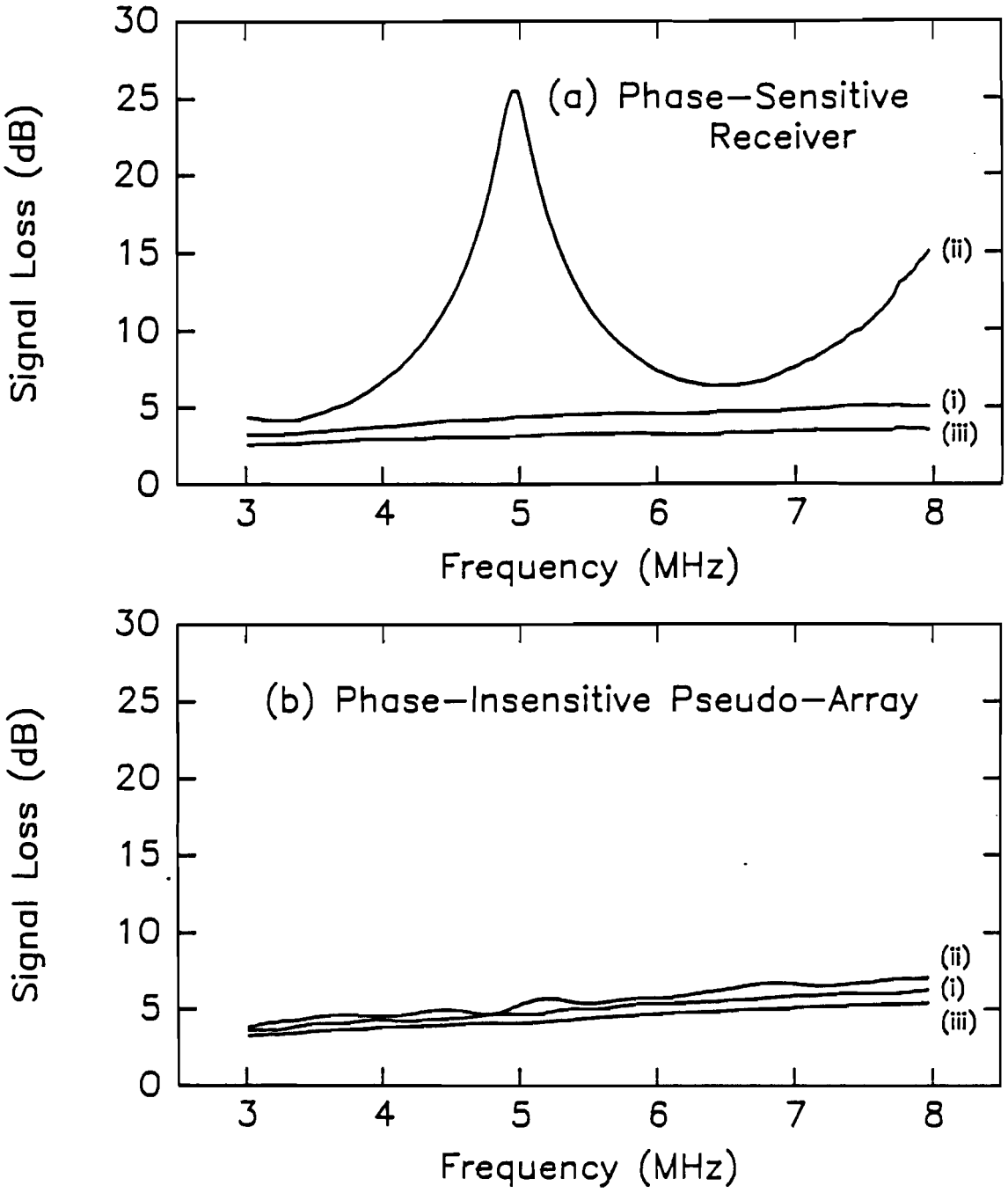

Figure 2. Results of stepped-plate measurements. In panel (a) the loss measured at the position of the step-discontinuity using phase-sensitive detection exhibits a scalloped frequency-dependence, in contrast with the linear dependence exhibited by the loss at other positions. In panel (b) the loss measured using phase-insensitive detection exhibits linear behavior at all sites.

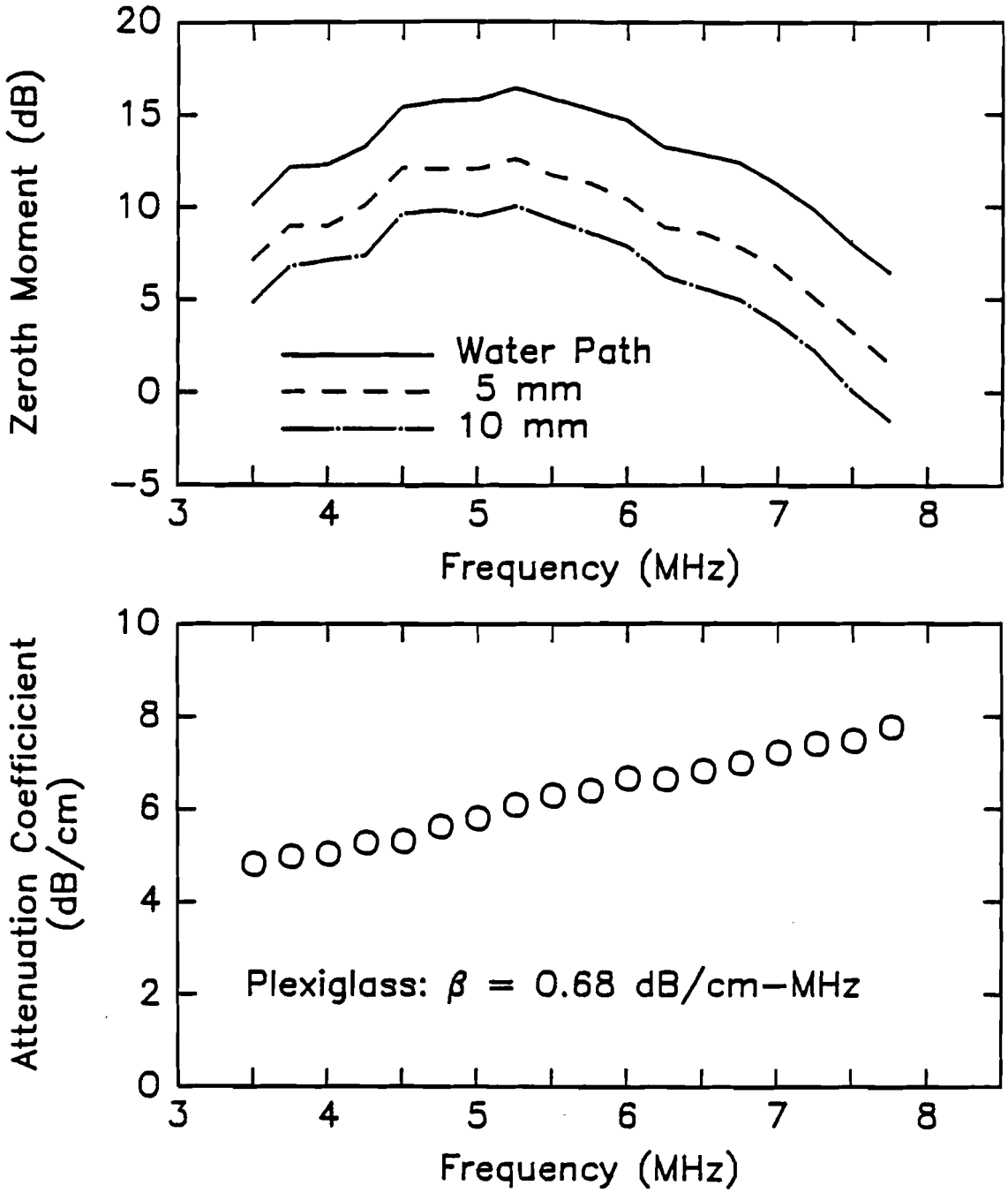

Figure 3. Attenuation of plexiglass measured using phase-insensitive pseudo-array. Upper panel: Zeroth-order spatial moment of the received beam with a water only path (solid), and with the insertion of a 5 mm thick plexiglass plate (dashed), and a 10 mm thick plexiglass plate (dot-dashed). Lower panel: Attenuation coefficient of plexiglass is determined by the slope of a linear fit of M_0 versus thickness at each frequency. This attenuation estimate is free of transmission coefficient contributions.

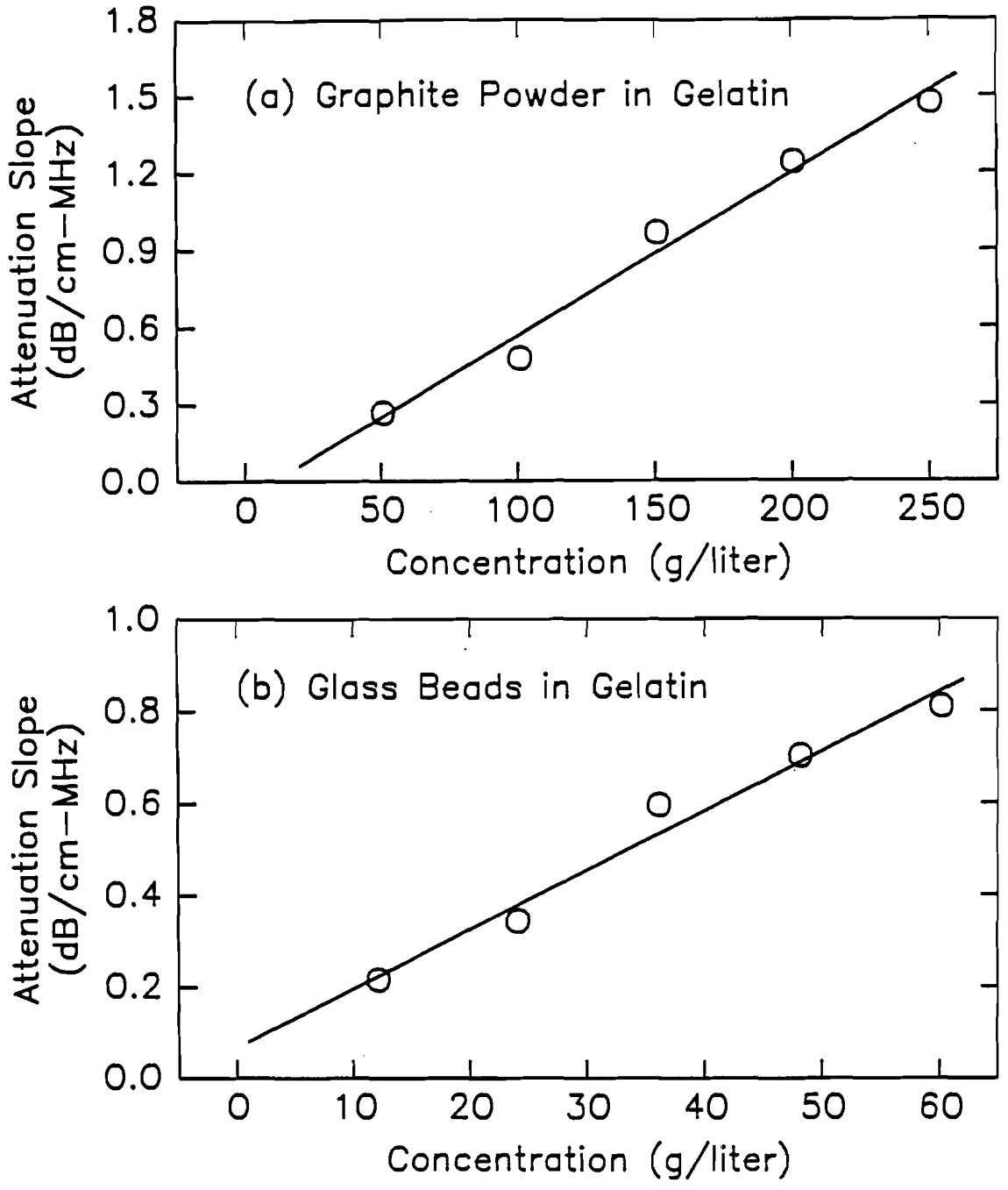

Figure 4. Slope of attenuation measured using a phase-insensitive two-dimensional pseudo-array plotted as a function of concentration of inclusions for tissue-mimicking phantoms constructed using (a) graphite powder in gelatin and (b) glass beads in gelatin. Slope is found to depend linearly with concentration, in agreement with Insana et al. [9].

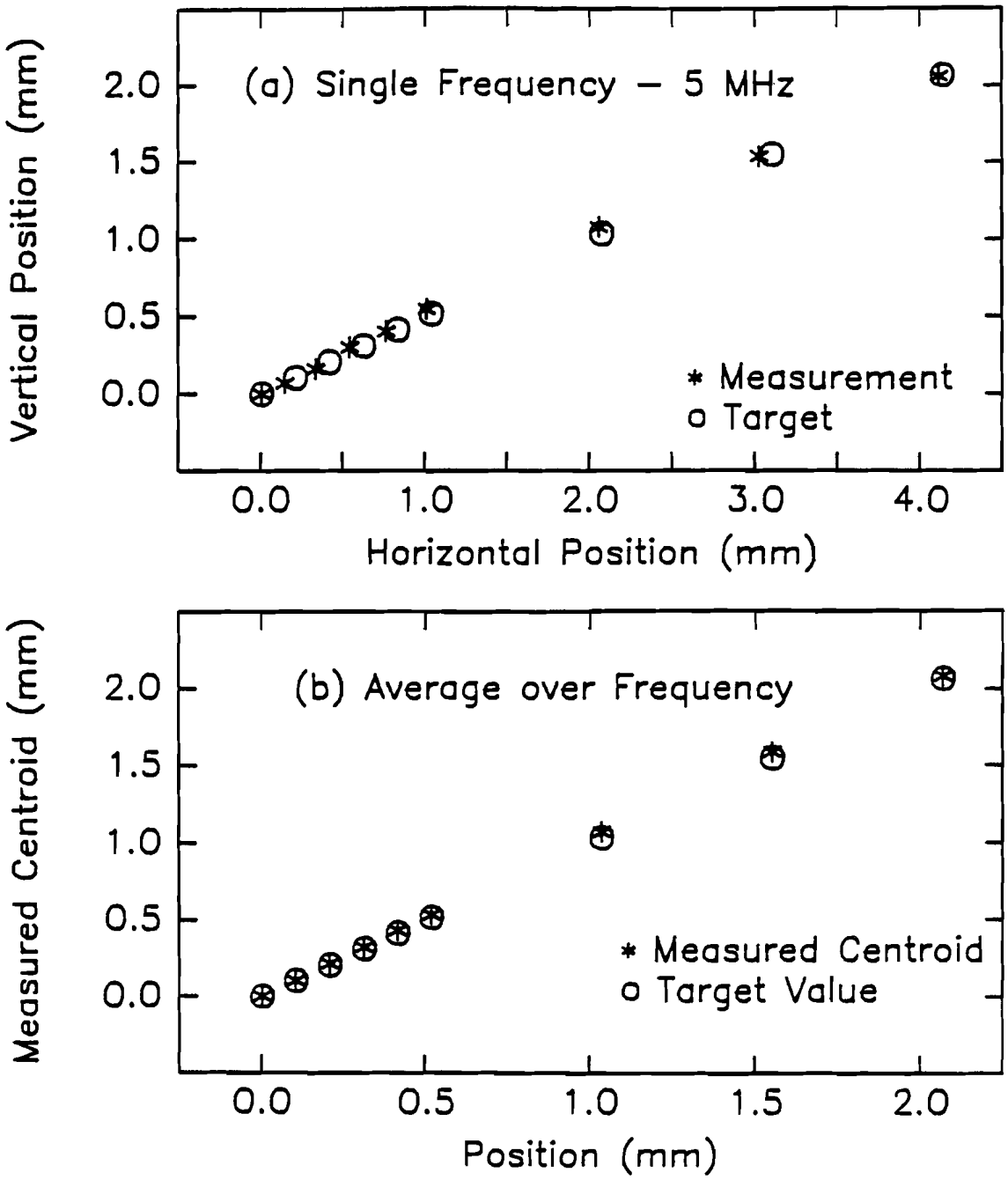

Figure 5. Estimated centroid of beam as the position of the pseudo-array is varied. (a) Single frequency measurement of centroid exhibits some error in position of the beam. (b) Average of centroid components determined at several frequencies yields an improved estimate of the centroid.

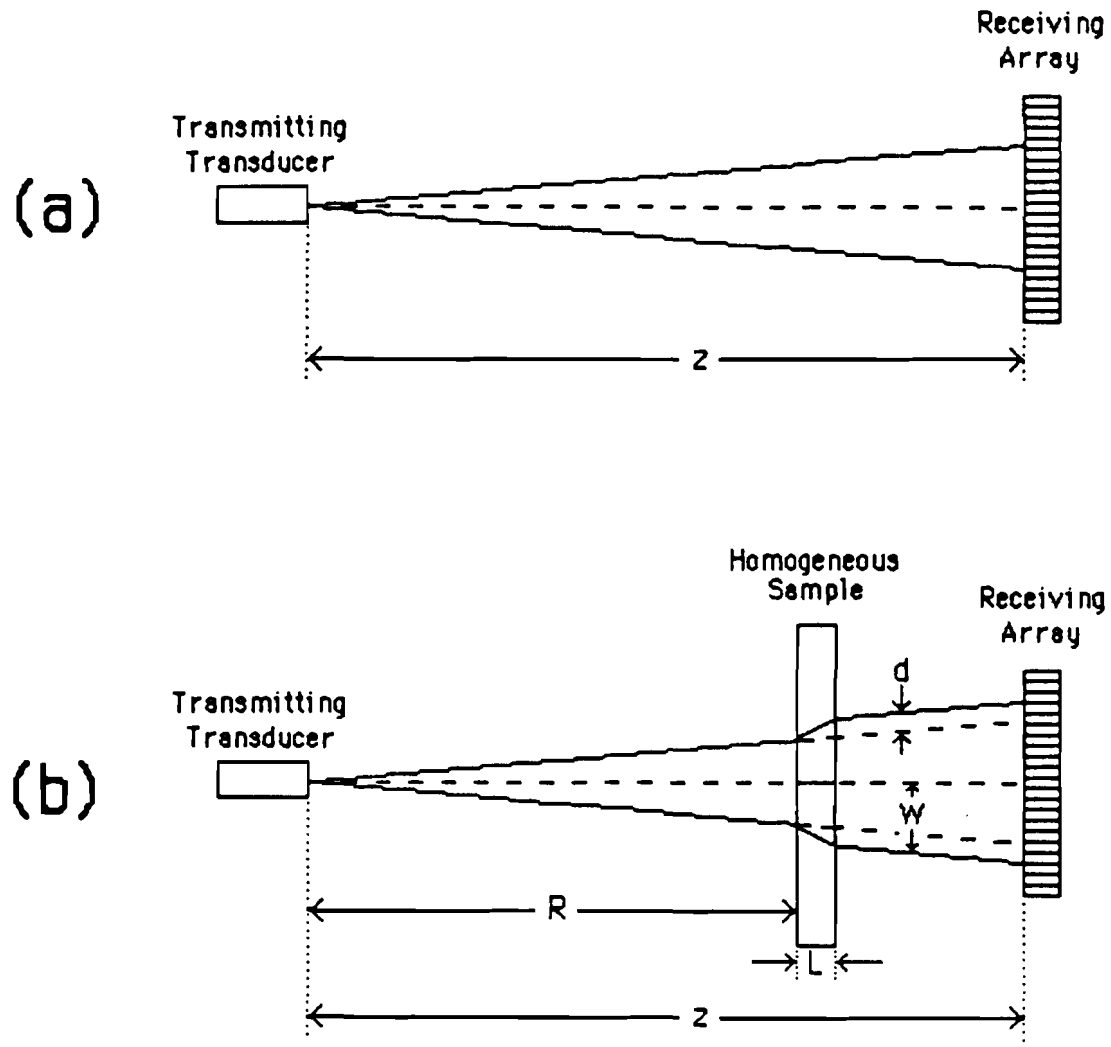

Figure 6. Divergence of the ultrasonic field (a) in a water-only path and (b) with a specimen present. A specimen having a faster speed of sound than the surrounding bath broadens the ultrasonic beam.

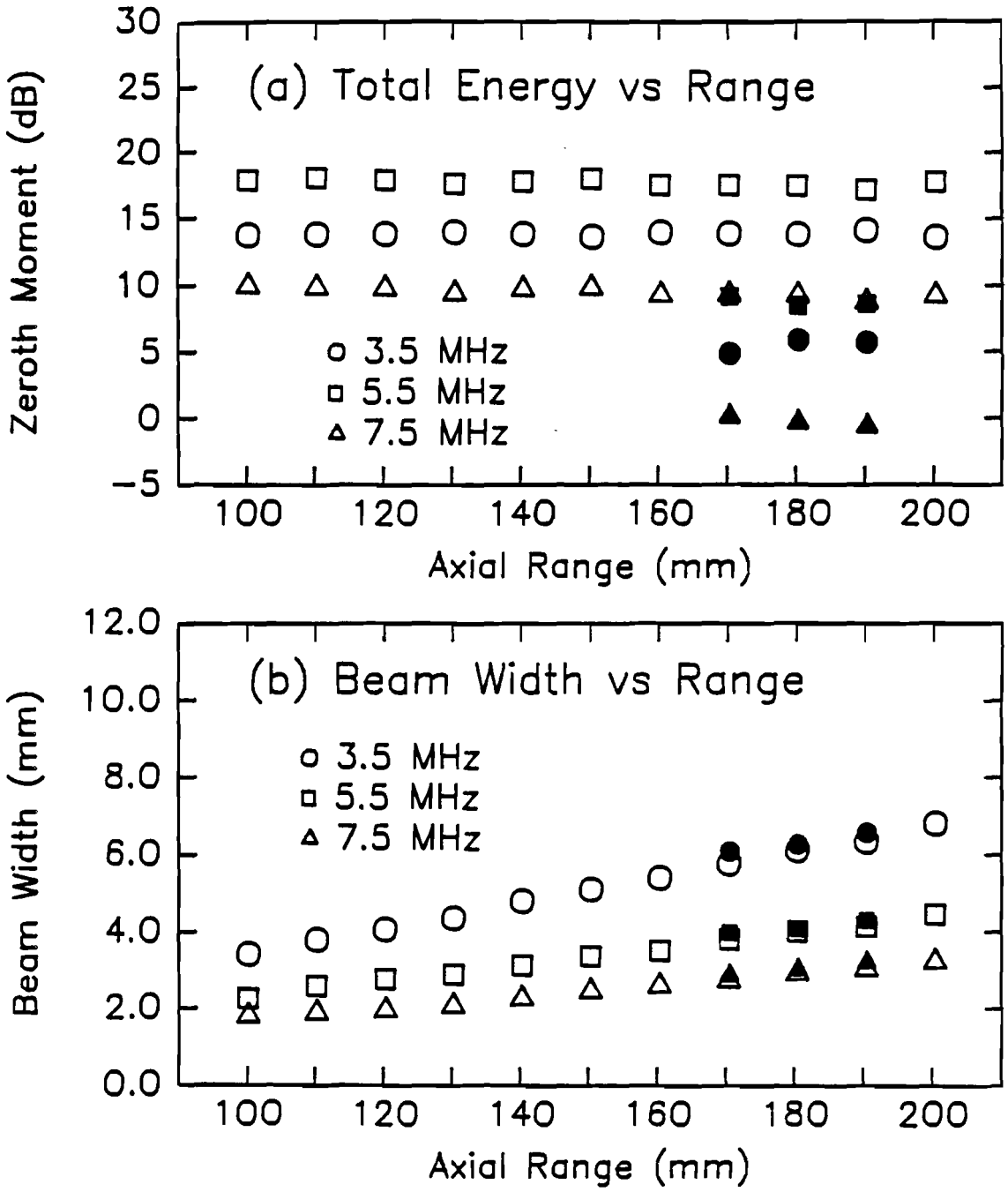

Figure 7. Zeroth moment and beam width as a function of axial range. Open symbols indicate measurements in water only. Filled symbols correspond to measurements performed with a 10 mm plexiglass specimen in the beam.

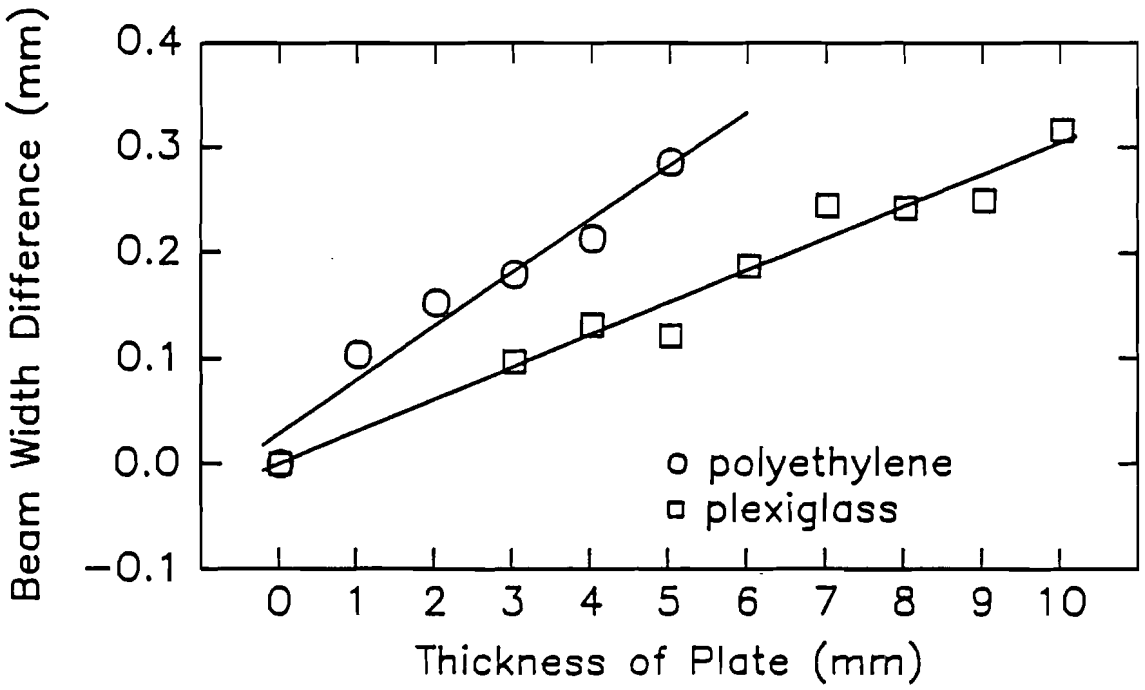

Figure 8. Broadening of a transmitted beam by propagation through plexiglass and polyethylene plates.

B-2. Theory of Moments in N Dimensions

Personnel: P. H. Johnston, BCL
J. G. Miller, BCL

Support: RR 01362
HL 17646
HL 28998

Our experimental work is based primarily upon the measurement of the ultrasonic energy transmitted or scattered in an experiment as a function of one or more variable coordinates. Although we seldom examine the properties of a measured distribution of energy over all variables at once, a general approach to analysis might provide the flexibility to do so. In what follows we investigate moments in N dimensions. The results presented in the last progress report which involve only one or two dimensions are easily extracted from the general formulation. The general forms also allow the extension of our present ideas into higher dimensionality for future applications.

Consider a function f(x) of the variable x defined over some domain V. The nth order moment of the function f(x) over V is defined as

$$m_n[f] = \int_V x^n f(x)dx \ . \tag{2.1}$$

This integral may be viewed as the average value of x^n over the domain V, with each increment of the domain weighted by a density function f(x). Alternatively, we choose to view the integral as an average of f(x) with weighting function x^n. In the notation of Equation (2.1), the argument in square brackets denotes the function to which the moment formula is applied, to distinguish the moments $m_n[f]$ of function f(x) from the moments $m_n[g]$ of function g(x).

An extension of this formulation to N dimensions is

$$m_{ij\cdots k}[f] = \int_{V^N} x_1^i x_2^j \cdots x_N^k f(\vec{x}) \, d^N\vec{x} \tag{2.2}$$

where

$$\vec{x} = (x_1, x_2, \cdots, x_N) \tag{2.3}$$

$$d^N\vec{x} = dx_1 dx_2 \cdots dx_N \ .$$

Here each of the N subscripts applied to m denotes the power to which the corresponding variable is raised in the weighting factor of the integral. We refer to the N-dimensional volume V^N as the aperture in analogy with the

case of two spatial dimensions. In addition, we say that the raw N-dimensional moment $m_{ij\cdots k}[f]$ is of order $n=i+j+\cdots+k$.

Radial Moments

One special class of multidimensional moments is what we refer to as the radial moments. The nth order radial moment $M_{Nn}[f]$ is defined as the integral of the function $f(\vec{x})$ over the aperture V^N weighted by the nth power of the radius vector $\vec{x}$

$$M_n[f] = \int_{V^N} \vec{x}^n \, f(\vec{x}) \, d^N\vec{x} \, . \tag{2.4}$$

The notation $\vec{x}^n$ expands as

$$\vec{x}^n = \begin{cases} 1 \, , & n=0 \\ \vec{x} \, , & n=1 \\ \vec{x} \cdot \vec{x} \, , & n=2 \\ (\vec{x}\cdot\vec{x})\vec{x} \, , & n=3 \\ (\vec{x}\cdot\vec{x})^2 \, , & n=4 \\ \cdots \, , & \cdots \end{cases} \tag{2.5}$$

Examination of the weighting factor $\vec{x}^n$ reveals that the even order radial moments are scalars and the odd order radial moments are vectors.

An appealing property of the lowest order radial moments is that they yield to physical interpretation. The scalar zeroth order radial moment is the definite integral of $f(\vec{x})$ over the aperture V^N, the "total energy" or "total mass," the most global characteristic of $f(\vec{x})$. The vector first order moment of $f(\vec{x})$ is related to the "centroid" or "center of gravity," a global property specifying the center of concentration of the function $f(\vec{x})$. The scalar second order radial moment represents the spread of $f(\vec{x})$ about the origin of coordinates, or the "moment of inertia." Third and fourth order radial moments are related to the "skewness" and "kurtosis" of the function, respectively. These interpretations provide much of the motivation for the use of radial moments in this work to characterize the distribution of ultrasonic energy.

Central Moments

The radial moments are defined relative to the origin of the particular coordinate system in use. Alternatively, the weighting factor of radial moments may be defined relative to any other point in N-space. If the point of reference is chosen to lie at the centroid of the function $f(\vec{x})$ defined as

$$\vec{C}[f] = \frac{\vec{M}_1[f]}{M_0[f]} , \tag{2.6}$$

then the moments are referred to as radial central moments of $f(\vec{x})$. These are denoted as U_n and are given by

$$U_n[f] = \int_{V^N} \left[\vec{x} - \vec{C}[f]\right]^n f(\vec{x})\, d^N\vec{x} . \tag{2.7}$$

In addition, raw central moments in a form analogous to Equation (2.2) may be defined as

$$\mu_{ij\cdots k}[f] = \int_{V^N} (x_1-C_1)^i (x_2-C_2)^j \cdots (x_N-C_N)^k f(\vec{x}) d^N\vec{x} . \tag{2.8}$$

Aperture Moments

In the special case that the function of interest is unity, i.e. $f(\vec{x})=1$, the moments specify geometric properties of the aperture itself. Thus we assign special notation to these aperture moments as follows

$$m_{ij\cdots k}[1] = a_{ij\cdots k} \qquad \mu_{ij\cdots k}[1] = \alpha_{ij\cdots k}$$

$$M_n[1] = a_n \qquad U_n[1] = A_n \tag{2.9}$$

As in the case of the radial moments of an arbitrary distribution, the radial aperture moments yield to physical interpretation as descriptors of the geometry of the aperture. The zeroth order moment a_0 represents the total volume of the aperture. The geometrical center of the aperture is given by the centroid $\vec{O} = \vec{a}_1/a_0$. The average width of the aperture is related to the second order aperture moments.

As a reference aid for the reader, a summary of the various types of moments defined above is presented in Table 1.

Summary of Moments			
Moment Description		Non-Central	Central
Distribution	Raw	$m_{ij\cdots k}$	$\mu_{ij\cdots k}$
	Radial	M_n	U_n
Aperture	Raw	$a_{ij\cdots k}$	$\alpha_{ij\cdots k}$
	Radial	a_n	A_n

Table 1. Summary of notation for the various types of moments defined in this chapter.

A useful property to note is that for apertures exhibiting symmetry about the x and y axes the odd order central aperture moments are zero. In order to demonstrate this, we now examine the aperture moments in two dimensions of three configurations depicted in Figure 1. Consider first the raw central aperture moments of a circular aperture of radius R, depicted in panel (a)

$$\alpha_{pq} = \int_{\text{circle}} x^p \, y^q \, dx \, dy \quad . \tag{2.10}$$

Converting to polar coordinates yields

$$\alpha_{pq} = \int_0^{2\pi} \cos^p \theta \, \sin^q \theta \, d\theta \int_0^R r^{1+p+q} \, dr \quad . \tag{2.11}$$

The radial integral evaluates to $R^{2+n}/(2+n)$, where n=p+q. The angular integral equals zero whenever either of p or q is odd. The results of these evaluations are tabulated in Table 2 along with results for two cases of rectangular aperture.

We now compute the aperture moments for a rectangular aperture of width w and height h, as shown in panel (b) of Figure 1. First, let the

origin be located in the lower left corner of the aperture, so that the raw aperture moments become

$$a_{pq} = \int_0^w dx \int_0^h dy\ x^p\ y^q = \frac{w^{p+1} h^{q+1}}{(p+1)(q+1)} \quad . \tag{2.12}$$

The values obtained for up through fourth order are given in Table 2. We note that all of the moments are non-zero. The centroid is located at the geometrical center of the aperture, i.e.

$$\vec{o} = \left(\frac{a_{10}}{a_{00}}, \frac{a_{01}}{a_{00}}\right) = \left(\frac{w}{2}, \frac{h}{2}\right) \quad , \tag{2.13}$$

as expected.

Shifting the origin of coordinates to $\vec{o}$, as presented in panel (c) of Figure 4, we calculate the central aperture moments

$$\alpha_{pq} = \int_{-h/2}^{h/2} dx \int_{-h/2}^{h/2} dy\ x^p\ y^q$$

$$= \frac{(w/2)^{p+1}(h/2)^{q+1}}{(p+1)(q+1)} \left[1-(-1)^{p+1}\right]\left[1-(-1)^{q+1}\right] \quad . \tag{2.14}$$

Examination of this result reveals that if either p or q are odd then the central aperture moment is zero. Values of these moments are listed in Table 2. We note that the numerical value of all the moments in Table 2 will decrease with n if the dimensions of the aperture are numerically less than unity. This property has been found to be useful for improving the convergence of algorithms for reconstruction of images from their moments [1].

Interrelationships Between Moments

The several types of moments defined above are linked by simple relationships. The raw central moments may be expressed in terms of the raw moments through application of the binomial expansion

$$(x_i - C_i)^p = \sum_{q=0}^{p} \binom{p}{q} (-C_i)^{p-q}\ x_i^q \tag{2.15}$$

where

$$\binom{p}{q} = \frac{p!}{q!(p-q)!} \quad . \tag{2.16}$$

Substitution into Equation (2.8) yields the result

$$\mu_{ij\cdots k}[f] = \sum_{\alpha=0}^{i} \sum_{\beta=0}^{j} \cdots \sum_{\gamma=0}^{k} \binom{i}{\alpha} \binom{j}{\beta} \cdots \binom{k}{\gamma} \times$$

$$(-C_1)^{i-\alpha}(-C_2)^{j-\beta} \cdots (-C_N)^{k-\gamma} m_{\alpha\beta\cdots\gamma} \quad . \tag{2.17}$$

A raw central moment of order n thus expands in terms of the raw moments of order less than or equal to n and powers of the components of the centroid.

The expression of radial moments in terms of raw moments involves a multinomial expansion

$$(\vec{x}\cdot\vec{x})^k = \left[\sum_{i=1}^{N} x_i^2\right]^k = \sum_{k_1,k_2\cdots,k_N} (k;k_1,k_2,\cdots,k_N) \prod_{i=1}^{N} x_i^{2k_i} \tag{2.18}$$

where

$$(k;k_1,k_2,\cdots,k_N) = \frac{k!}{k_1!k_2! \cdots k_N!} \tag{2.19}$$

and where the summation is over values of k_j which sum to k, i.e.

$$\sum_{j=1}^{N} k_j = k \quad . \tag{2.20}$$

Using Equation (2.18) in Equation (2.4) we thus find that the even order radial moments are given by

$$M_{2k} = \sum_{k_1,k_2,\cdots,k_N} (k;k_1,k_2,\cdots,k_N) m_{2k_1 2k_2 \cdots 2k_N} \tag{2.21}$$

and the jth components of the odd order radial moments are given by

$$\left\{M_{2k+1}\right\}_j = \sum_{k_1,k_2,\cdots,k_N} (k;k_1,k_2,\cdots,k_N) m_{2k_1 2k_2 \cdots 2k_j+1 \cdots 2k_N}. \tag{2.22}$$

In analogy with the preceding equations, the relationship between the radial and raw central moments are

$$U_{2k} = \sum_{k_1,k_2,\cdots,k_N} (k;k_1,k_2,\cdots,k_N) \mu_{2k_1 2k_2 \cdots 2k_N} \tag{2.23}$$

and the jth components of the odd order radial moments are given by

$$\left\{U_{2k+1}\right\}_j = \sum_{k_1,k_2,\cdots,k_N} (k;k_1,k_2,\cdots,k_N)\mu_{2k_1 2k_2\cdots 2k_j+1\cdots 2k_N} \quad . \tag{2.24}$$

These may in turn be expressed in terms of the noncentral raw moments by substituting from Equation (2.17).

We now evaluate these expressions for the lowest order moments to point out some important relationships. The first important set of relationships is the equality among the zeroth order moments

$$m_{00\cdots0} = M_0 = U_0 = \mu_{00\cdots0} = \int_{V^N} f(\vec{x})\, d^N\vec{x} \tag{2.25}$$

$$a_{00\cdots0} = a_0 = A_0 = \alpha_{00\cdots0} = \int_{V^N} d^N\vec{x} \quad .$$

Another set of equalities exists in one dimension, where the raw moments become identical to the corresponding radial moments, i.e.

$$\begin{aligned} m_n &= M_n \\ \mu_n &= U_n \\ a_n &= a_n \\ \alpha_n &= A_n \end{aligned} \qquad \text{in one dimension.} \tag{2.26}$$

The relationships between the first order moments are

$$\vec{M}_1 = \left[m_{10\cdots0}, m_{01\cdots0}, \cdots, m_{00\cdots1}\right] = M_0\vec{C} \tag{2.27}$$

$$\vec{U}_1 = \left[\mu_{20\cdots0}, \mu_{01\cdots0}, \cdots, \mu_{00\cdots1}\right] = 0 \quad . \tag{2.28}$$

$$\vec{a}_1 = \left[a_{10\cdots0}, a_{01\cdots0}, \cdots, a_{00\cdots1}\right] = a_0\vec{0} \tag{2.29}$$

$$\vec{A}_1 = \left[\alpha_{10\cdots0}, \alpha_{01\cdots0}, \cdots, \alpha_{00\cdots1}\right] = 0 \quad . \tag{2.30}$$

Equation (2.27) defines the position of the centroid of $f(\vec{x})$ relative to an arbitrary origin of coordinates in V^N. The same is true for Equation (2.29). Because the central moments are by definition calculated about the centroid, the first order central moments are all equal to zero.

The evaluated expressions for second order moments are

$$\mu_{1_i 1_j} = m_{1_i 1_j} - m_0 C_i C_j \tag{2.31}$$

$$\mu_{2_i} = m_{2_i} - m_0 C_i^2$$

$$M_2 = \sum_{i=1}^{N} m_{2_i} \tag{2.32}$$

$$U_2 = \sum_{i=1}^{N} \mu_{2_i} \; . \tag{2.33}$$

Here we have introduced a new notation in which

$$m_{a_i b_j} = \int_{V^N} x_i^a x_j^b \, f(\vec{x}) d^{N\vec{}}x \tag{2.34}$$

and

$$\mu_{a_i b_j} = \int_{V^N} (x_i - C_i)^a (x_j - C_j)^b \, f(\vec{x}) \, d^{N\vec{}}x \; . \tag{2.35}$$

Expanding the central radial moments using the other relations shown, we may obtain a familiar form for the parallel axis theorem

$$U_2 = M_2 - U_0 |\vec{C}|^2 \; . \tag{2.36}$$

Expansion of the third order moments yields

$$\mu_{1_i 1_j 1_k} = m_{1_i 1_j 1_k} - \left(C_i m_{0_i 1_j 1_k} \; C_j m_{1_i 0_j 1_k} + C_k m_{1_i 1_j 0_k} \right) + 2 m_{0_i 0_j 0_k} C_i C_j C_k$$

$$\mu_{2_i 1_j} = m_{2_i 1_j} - m_{2_i 0_j} C_j - 2 m_{1_i 1_j} C_i + 2 m_{0_i 0_j} C_i^2 C_j \tag{2.37}$$

$$\mu_{3_i} = m_{3_i} - 3 m_{2_i} C_i + 2 m_{0_i} C_i^3$$

$$\left\{ M_3 \right\}_j = \sum_{i=1}^{N} m_{2_i 1_j} \tag{2.38}$$

$$\left\{U_3\right\}_j = -\sum_{i=1}^{N} \mu_{2_i 1_j} \quad . \tag{2.39}$$

1. Teague, M. R., "Image Analysis Via the General Theory of Moments," Journal of the Optical Society of America, vol. 70, pp. 920-930, 1980.

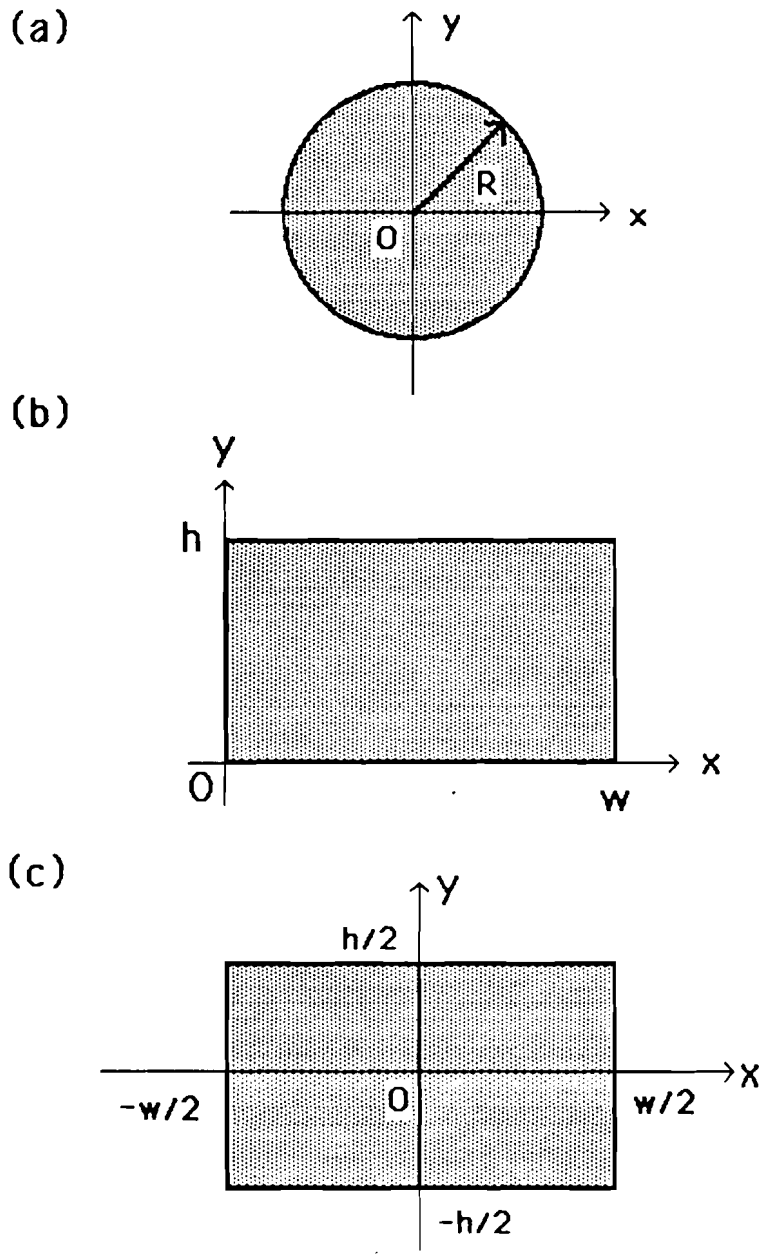

Figure 1. Three arrangements of symmetric aperture and coordinate axes for demonstration of aperture moments: (a) a circular aperture of radius R with the origin of coordinates at its center, (b) a rectangular aperture of height h and width w with the origin of coordinates at its lower left corner, and (c) the rectangular aperture of (b) with the origin of coordinates moved to its center.

n	p	q	circle radius R α_{pq}	rectangle $[0,w],[0,h]$ a_{pq}	rectangle $[-w/2,w/2][-h/2,h/2]$ α_{pq}
0	0	0	πR^2	wh	wh
1	1	0	0	$w^2h/2$	0
	0	1	0	$wh^2/2$	0
2	2	0	$\pi R^4/4$	$w^3h/3$	$w^3h/12$
	0	2	$\pi R^4/4$	$wh^3/3$	$wh^3/12$
	1	1	0	$w^2h^2/4$	0
3	3	0	0	$w^4h/4$	0
	0	3	0	$wh^4/4$	0
	2	1	0	$w^3h^2/6$	0
	1	2	0	$w^2h^3/6$	0
4	4	0	$\pi R^6/8$	$w^5h/5$	$w^5h/80$
	0	4	$\pi R^6/8$	$wh^5/5$	$wh^5/80$
	3	1	0	$w^4h^2/8$	0
	1	3	0	$w^2h^4/8$	0
	2	2	$\pi R^6/24$	$w^3h^3/9$	$w^3h^3/144$

Table 2. Values of the aperture moments for the three symmetrical two-dimensional apertures presented in Figure 1.

B-3. Effects of Noise on Moments

Personnel: P. H. Johnston, BCL
J. G. Miller, BCL

Support: RR 01362
HL 17646
HL 28998

We find that higher order moments are more sensitive to noise and finite-aperture effects than are lower moments. To illustrate this qualitatively, consider the one dimensional slice along the x_i axis through the centroid of a multidimensional function $f(\vec{x})$ presented in Figure 1. This function might, for example, represent an energy distribution composed of a signal $H(\vec{x})$ plus noise $\eta(\vec{x})$. Here the distribution of energy $H(\vec{x})$ is concentrated about the centroid located at point C, and falls to relatively small values at positions far away from that point. The noise $\eta(\vec{x})$ is approximately constant over the aperture, and is much less than the value of the signal $H(\vec{x})$ in the vicinity of point C, but is greater than the signal far away from point C. Under the assumption that the origin of coordinates lies at the centroid, point C, the nth order radial central moment is expressed in N dimensional polar coordinates (r,Ω) as

$$U_n[f] = \int_{V^N} \vec{x}^n \left[H(r,\Omega) + \eta(r,\Omega)\right] r^{N-1} dr\, d\Omega \quad , \tag{3.1}$$

where the value r is the radial distance from the centroid and Ω represents solid angle. The effective weighting factor in this integral results from the product of $\vec{x}^n$ and r^{N-1} and is thus proportional to r^{n+N-1}. Hence the contribution of values of $H(\vec{x})+\eta(\vec{x})$ at distances far from the origin is increasingly more important as either the order n or the dimensionality N increases. Because we assumed that regions where $\eta(\vec{x})>H(\vec{x})$ are far from the origin, such as segments AF and GB, higher-order moments are very sensitive to the noise level.

Another problematical feature is that small details in the function $f(\vec{x})$ at distances further from the origin are weighted more stongly than similar features nearer the centroid. For example, given that the small lobe at position E in Figure 1 and the shoulder at position D contribute equally to the zeroth moment of $f(\vec{x})$, the lobe at position E will have a greater effect on all higher-order moments than the shoulder due to its greater distance from the origin. In addition, the extraneous noise bump at position A will exhibit a distorting influence on the moments calculated over the full aperture AB. Thus, more remote features in actual measurements such as sidelobes or random fluctuations in amplitude in the wings of the distribution of energy contribute significantly to higher order moments. This is usually not desirable because the most interesting information is contained in the main lobe of the distribution of energy, and random fluctuations are not representative of global characteristics of the medium under test.

Further, in the case of a bounded volume (aperture), the higher-order moments will be more sensitive to the shape and size of the boundary

due to the weighting factor r^{n+N-1}. In Figure 2 we show a function $f(\vec{x})$ over the aperture AB in which the signal is significantly larger than the noise only in a small fraction of the aperture. Considered over the full aperture, the function $f(\vec{x})$ resembles a constant with a small bump on it. Moments calculated over the full aperture AB will therefore be dominated by the constant noise level and hence will be relatively insensitive to changes in the desired signal at C. Moments calculated over the aperture DE, however, would be dominated by the signal itself.

These considerations indicate the need to limit the region of integration to exclude locations where the signal falls below the noise or where small features of modest significance lie at relatively large distances from the centroid of energy. A cut-off might be applied so that the aperture in Figure 1 would be limited to the segment FG, for example. In a previous progress report we discussed a signal-dependent cutoff scheme for estimation of the two-dimensional moments of an ultrasonic beam.

Statistical Treatment of Noise Effects

Irrespective of the truncation or apodization employed, the signal which is used for calculation of moments is still the sum of signal plus noise. We now consider the propagation of noise into our determinations of the moments. For simplicity, we restrict ourselves to two dimensions in this section. A practical measurement consists of discrete values of energy taken from some instrument. The result can be expressed as

$$f(x_i,y_i) = H(x_i,y_i) + \eta_i \ , \tag{3.2}$$

where the measurements represent the energy at one of the N sample points $(x_i y_i)$ in the aperture, and are parameterized by the index i. The noise samples η_i are independent of $(x_i y_i)$ and are assumed drawn from a population exhibiting mean value $\langle\eta\rangle = \eta_0$ and variance σ^2. Our goal in this section is to find expressions for the mean and variance of several useful moments.

The definition of the raw moments in this discrete formulation takes the form

$$m_{pq}[f] = \sum_{i=1}^{N} x_i^p \, y_i^q \, f\,(x_i,y_i) \ . \tag{3.3}$$

Because of the linear nature of moments, the moment of the measurement is given by the sum of the moment of the signal and the moment of the noise

$$m_{pq}[f] = m_{pq}[H] + m_{pq}[\eta] \quad . \tag{3.4}$$

From this it is easy to see that the mean value of the raw moment is given by the sum of the desired moment of energy and the mean value of the moment of noise

$$\langle m_{pq}[f] \rangle = m_{pq}[H] + \langle m_{pq}[\eta] \rangle \quad . \tag{3.5}$$

Examination of the mean value of the moment of noise samples yields

$$\begin{aligned} \langle m_{pq}[\eta] \rangle &= \left\langle \sum_{i=1}^{N} x_i^p \, y_i^q \, \eta_i \right\rangle \\ &= \sum_{i=1}^{N} x_i^p \, y_i^q \, \langle \eta_i \rangle \\ &= a_{pq} \, \eta_0 \quad . \end{aligned} \tag{3.6}$$

Here we have identified the discrete form of the raw aperture moment a_{pq} and the definition of the mean value of the noise η_0. Thus, the general result for the mean value of a moment of a signal plus noise is

$$\langle m_{pq}[f] \rangle = m_{pq}[H] + a_{pq} \, \eta_0 \quad . \tag{3.7}$$

The desired moment value is modified by the addition of the mean noise level times the corresponding aperture moment. Further, as we saw in the preceding section, if the aperture exhibits symmetry about the coordinate axes, then the appropriate aperture moments are the central moments α_{pq} which are zero for order n=p+q=odd. Thus, the effects of noise are minimized in the mean for odd-order moments over a symmetrical aperture.

We now examine the variance of the raw moments. As each sample of the noise function is assumed independent of all the others, the variance of $m_{pq}[f]$ may be defined [1]

$$\mathrm{var}(m_{pq}[f]) = \sum_{k=1}^{N} \left(\frac{\partial m_{pq}[f]}{\partial \eta_k} \right)^2 \mathrm{var}(\eta_k) \quad . \tag{3.8}$$

The partial derivatives bring out the weighting function for the kth point

$$\frac{\partial m_{pq}[f]}{\partial \eta_k} = x_k^p \, y_k^q \quad . \tag{3.9}$$

Noting that the variance of η is defined as σ^2 we write

$$\mathrm{var}(m_{pq}[f]) = \sum_{k=1}^{N} (x_k^p \, y_k^q)^2 \sigma^2 \tag{3.10}$$

or

$$\mathrm{var}(m_{pq}[f]) = a_{2p2q}\sigma^2 \quad . \tag{3.11}$$

This result states that the variance of a moment of order n=p+q is equal to the product of the variance of the noise and the corresponding aperture moment of order 2n=2p+2q. No choice of aperture will provide even order aperture moments equal to zero, in contrast with the odd-order aperture moments. Thus all moments will exhibit nonzero variance in proportion to the noise variance and higher-order moments of the aperture.

Mean and variance of the centroid

From the preceding results we can develop expressions for the other moments. In order to express the central moments, for example, we need the values of the centroid $\vec{C}$. The x component of the centroid is defined as $C_x = m_{10}/m_{00}$. Thus, the mean value is given by

$$\langle C_x \rangle = \frac{\langle m_{10}[f] \rangle}{\langle m_{00}[f] \rangle} \quad . \tag{3.12}$$

By the result of Equation (3.7), we express this as

$$\langle C_x \rangle = \frac{m_{10}[H] + \eta_0 \alpha_{10}}{m_{00}[H] + \eta_0 \alpha_{00}} \rightarrow \frac{m_{10}[H]}{m_{00}[H] + \eta_0 \alpha_{00}} \quad , \tag{3.13}$$

where the latter form is valid for a symmetrical aperture. For large signal to noise ratio, this may be approximated as

$$\langle C_x \rangle = \frac{m_{10}[H]}{m_{00}[H]\left[1 + \frac{\eta_0 \alpha_{00}}{m_{00}[H]}\right]} \approx \frac{m_{10}[H]}{m_{00}[H]}\left[1 - \frac{a_{00}\eta_0}{m_{00}[H]}\right]. \tag{3.14}$$

The constant noise floor tends to shift the apparent value of the centroid toward the origin in proportion to the ratio of the zeroth order moment of the noise to that of the signal.

The variance of the centroid is given in terms of the variances of the moments as [1]

$$\mathrm{var}(C_x) = \langle C_x \rangle^2 \left[\frac{\mathrm{var}(m_{10}[f])}{\langle m_{10}[f] \rangle^2} + \frac{\mathrm{var}(m_{00}[f])}{\langle m_{00}[f] \rangle^2}\right] \tag{3.15}$$

By previous results, we have $\text{var}(m_{10}[f]) = \sigma^2 a_{20}$ and $\text{var}(m_{00}[f]) = \sigma^2 a_{00}$. Assuming appropriate symmetry for use of the central aperture moments, we may write

$$\text{var}(C_x) = \sigma^2 \left(\frac{m_{10}[H]}{m_{00}[H] + \eta_0 \alpha_{00}}\right)^2 \left(\frac{\alpha_{20}}{m_{10}[H]^2} + \frac{\alpha_{00}}{(m_{00}[H] + \eta_0 \alpha_{00})^2}\right) . \tag{3.16}$$

For large signal to noise ratio, the first order approximation to the variance of the centroid is

$$\text{var}(C_x) \approx \sigma^2 \left(\frac{\alpha_{20}}{m_{00}[H]} + \frac{\alpha_{00} m_{10}[H]^2}{m_{00}[H]^4}\right) . \tag{3.17}$$

The above results support the idea of restricting the calculation of moments to as small an aperture as possible. The mean and variance of the noise in the measured signal appear as factors with the aperture moments. Thus, reducing the total aperture decreases the aperture moments and the effects of noise.

It was previously pointed out that the units of length can be adjusted to force the higher-order moments to numerically decrease with increasing order. This maneuver may thus reduce the numerical effects of noise on the moments. Some caution must be taken with this reasoning, however, because many of the useful quantities which can be found using moments (such as the centroid) are in terms of ratios of moments. It may be that these ratios are not so free of the effects of noise, since the scaling operation makes changes in numerator and denominator.

1. Bevington, P. R., Data Reduction and Error Analysis for the Physical Sciences, McGraw-Hill, New York, 1969.

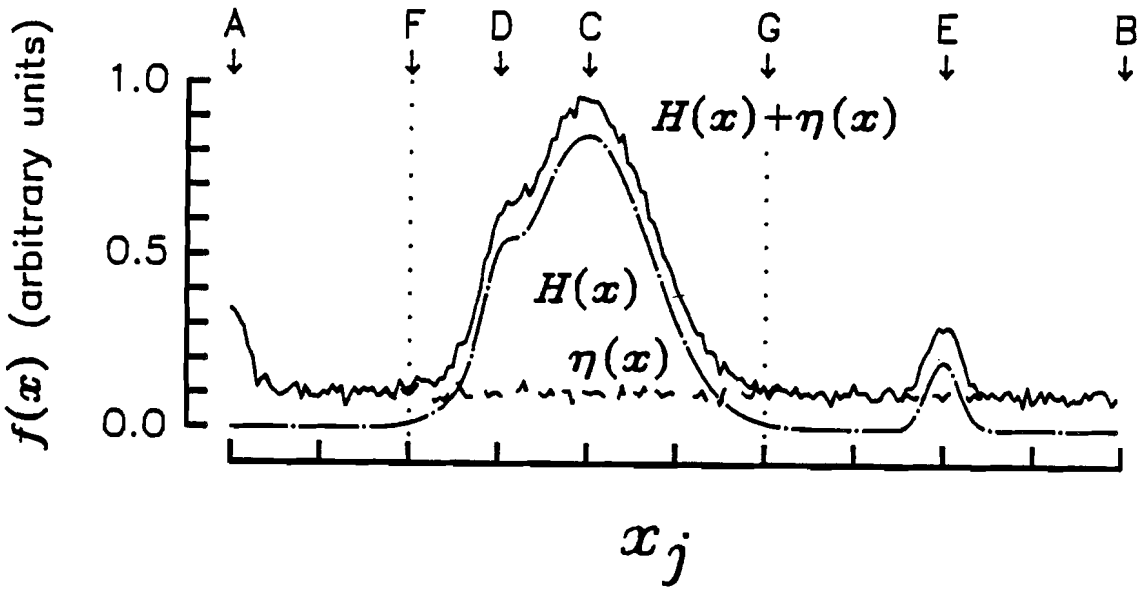

Figure 1. Example of a concentrated energy distribution illustrating noise and aperture effects. Measurement is the sum of signal H(x) and noise $\eta(x)$.

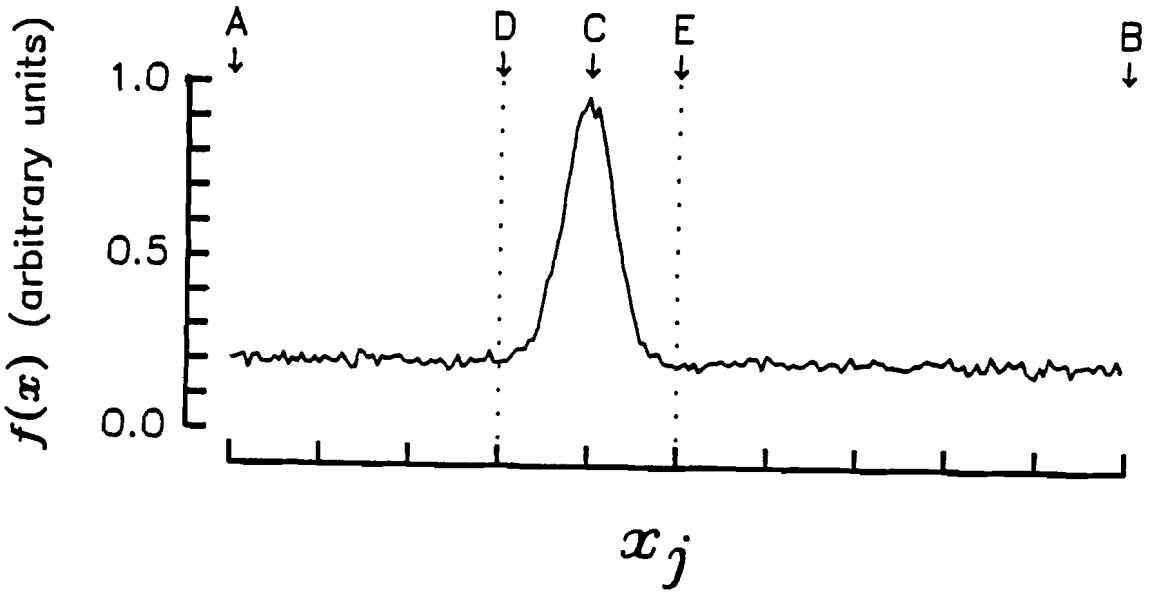

Figure 2. Demonstration of the detection of a concentrated energy distribution using a large aperture or a small aperture. Moments computed over aperture AB will be dominated by the noise value, while moments computed over the aperture DE will better represent the signal centered at C.

B-4. Ultrasonic Reflection Tomography

Personnel: S. R. Broadstone, BCL
R. M. Arthur, BCL

Support: RR 01362

Although state-of-the-art phased-array sector scanners produce images with good axial and azimuthal resolution, their performance is often compromised by constraints applied for real-time operation. If in-phase detection of backscattered signals is not performed at each image point in the field of view, accurate estimation of tissue properties is compromised. Consequently, an off-line imaging system was designed and built to investigate improvements for on-line or real-time imaging systems [1,2]. Because all signal-processing and image-generation steps were done in software, we could precisely compare homogeneous and adaptive beamforming algorithms and test any other algorithms on tissue phantoms or tissue samples without building new acquisition circuitry. Signals were acquired and images were generated using the processing environment described in Section B-6.

Signal Acquisition

We designed and built 32 drivers for ultrasonic-transducer elements, which could be controlled by the processing environment (Section B-6). These drivers were designed to deliver over 50% of the pulse energy uniformly to the 2-7 MHz range when loaded by an element of either the 3.5 or 5.0 MHz linear-array transducers used in this study. Each element had its own pulser, but only one receiver channel was available. Each element in turn was pulsed under computer control. The backscattered signal at the element with the receiver was sampled at 50 MHz, digitized with 8 bits of precision, and stored in response to each pulse. The receiver circuitry was moved to another element and the procedure was repeated until recordings were made from all elements of the array. Thus if there were N elements in the array, we recorded N^2 backscattered signals.

Just over 2000 samples from each backscattered signal were retained, so that we could view a 3×3 cm portion of the insonified object. Even though we performed no beamforming during acquisition to reduce the amount of data which had to be saved, only about 2 megabytes of storage were required for the element signals from a 32-element array. Raw signals were sent via serial line to our Masscomp workstation for further manipulation, beamforming, image generation, quantitative assessment, comparison, and display.

Image Generation

System performance was evaluated by imaging a water-filled AIUM 100-mm test object with a 3.5 MHz, 32-element linear array. We generated both linear-array and phased-array images using 5 elements from the center of the array, as well as using all 32 elements. We implemented the typical focus-and-steer algorithm and applied it ideally, so that it focused the array on each pixel in the view grid.

A new ray-tracing algorithm which also yields ideal focusing was developed. It, however, allowed the system to produce images about 30% faster than the focus-and-steer algorithm. Figure 1 shows the time-of-flight geometry for the ray-tracing algorithm. In a medium with constant phase-velocity, a line, or ray from the transmitting element to the field point (r_1) and back to the receiving element (r_2) permits calculation of the beamformer delay. The roundtrip time is

$$t_{rt} = (r_1 + r_2) / c$$

$$r_1 = [\ (x - x_0)^2 + (z - z_0)^2\ ]^{1/2}$$

$$r_2 = [\ (x - d - x_0)^2 + (z - z_0)^2\ ]^{1/2}$$

where c is the speed of sound in the medium.

The focus-and-steer algorithm was also applied in a manner typical of most real-time systems. The transducer was focused along an arc through the middle of the view grid. Although the result is qualitatively appealing, it suffers from significant phase-cancellation errors, both from improper focus and from spatial under sampling. The conventional phased-array image was clearly not suitable for quantitative analysis.

Images reconstructed using the ray-tracing algorithm with 240, 60 and 15 μm spatial sampling revealed the effects of phase cancellation due to spatial undersampling, even when the focusing was ideal. For example, in images with pixel size $\geq$ 240 μm (sample rates < 3.5 MHz), the size of the wires could not be determined to within a factor of two. Their shapes were grossly noncircular. On the other hand, the images with 15 μm pixel size permitted a reasonable estimate of the shape and size of the 0.75 mm diameter wires and showed details of the insides of wires, which were consistent with their material properties. Figure 2 shows the central wires, which are made of stainless steel, in the AIUM test object along with a 15 μm pixel-size image. The standing wave pattern inside the wires has a wavelength expected for stainless steel.

Real-Time Operation

Beamformers are usually implemented by delaying transducer-element signals appropriately before summing them to get a function of time which gives a view of the insonified tissue along a given direction. What is really of interest is how each instant of each element signal contributes to a particular pixel in the tissue image. We are now designing a VLSI circuit, to be used with the ultrasonic reflection tomographic system, which will serve as a digital delay line and a coordinate transformer to perform real-time beamforming and image generation. The VLSI circuit maps backscattered signals into the image-display space. In the tomographic system the backscattered signal at each element is collected in response to pulsing each element in turn. Clearly the mapping depends upon which element is the transmitter. For an N-element transducer, each element will have N circuits to map each sample of each transducer-element signal to the correct pixels in the final image.

A flow diagram of the VLSI circuit is shown in Figure 3. For simplicity the diagram describes a second-order polynomial fit of the mapping surface. A circuit which implements a higher-order fit operates at the same speed, but takes up more real estate. The beamforming scheme implemented depends upon how the mapping circuit is seeded. The circuit is seeded with first forward-differences from a Taylor series expansion of the polynomial which matches the mapping surface. It then calculates approximate values for round-trip samples values for the entire image space. For a homogeneous medium the backscattered signal from a given element falls along an ellipse in the image. The maximum error in a homogeneous medium for a second-order polynomial over a 512 × 512 region is 2.5 samples. For a third-order fit the error is 0.3 sample. Although initially a homogeneous medium will be assumed, the circuit can be seeded with values which depend on the medium and thereby implement adaptive-beamforming algorithms.

The parallel operation of N VLSI mapping circuits per element reduces the processing time per pixel to 125 ns for a 512 ×512 image and 50 MHz sample rate, where the number of elements N is 32. Real-time operation would still be unrealizable with present technology if the VLSI circuit had to calculate the roundtrip time using the expressions given previously, which depend on square and square root operations. The mapping circuit reduces those operations to a single add for any order polynomial and thus should be able to achieve real-time operation.

1. Broadstone, S. R., "Ultrasonic Reflection Tomography: An Off-Line High Resolution Imaging System for Tissue Characterization," Master's Thesis, Washington University, May, 1986.

2. Broadstone, S. R. and Arthur, R. M., "Ultrasonic Reflection Tomography: An Off-Line High Resolution Imaging System for Tissue Characterization," Ultrasonic Imaging, vol. 8, 1986 (abstract).

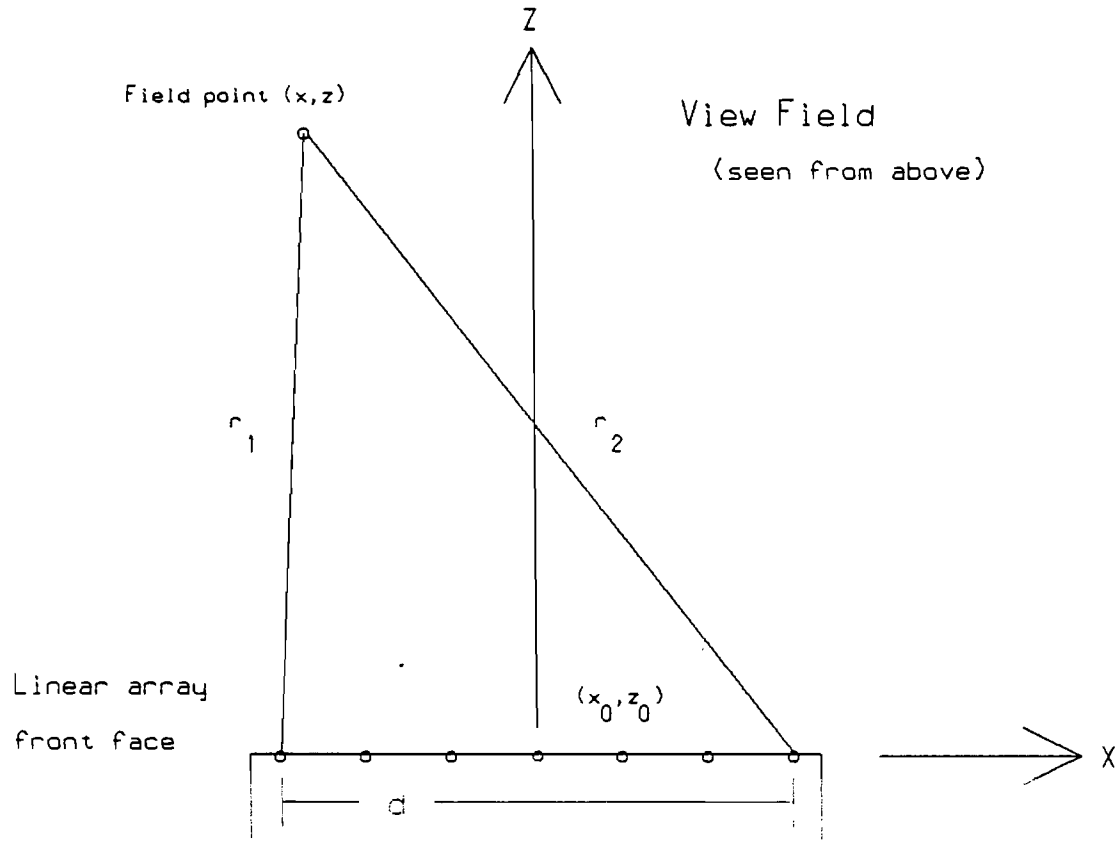

Figure 1. Time-of-Flight Geometry.

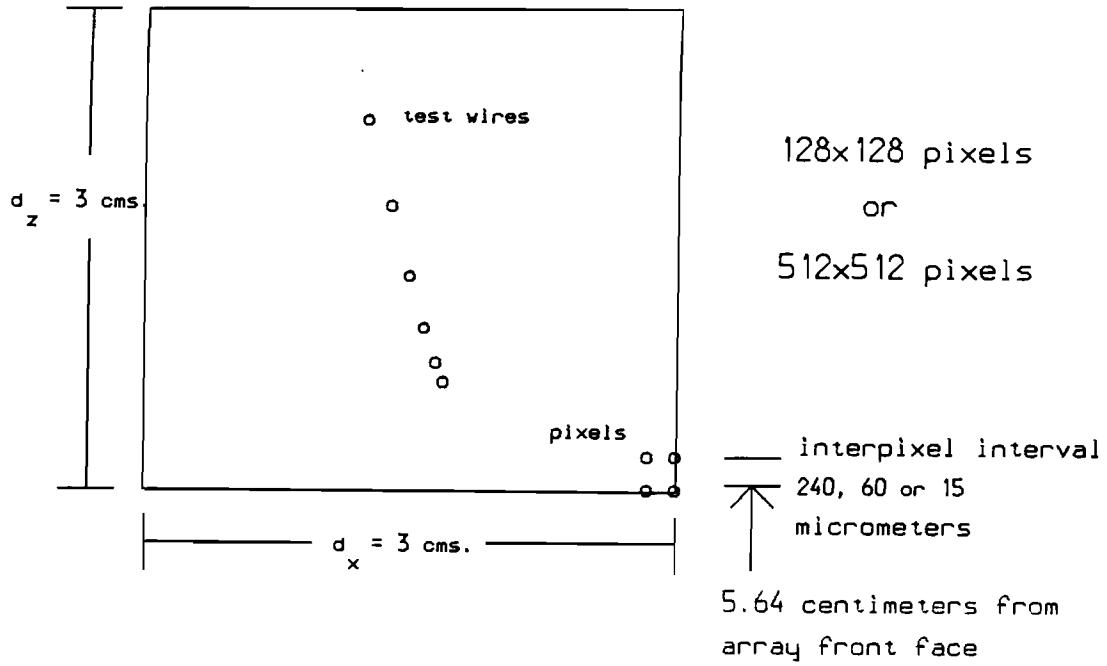

Figure 2a. View Grid Dimensions.

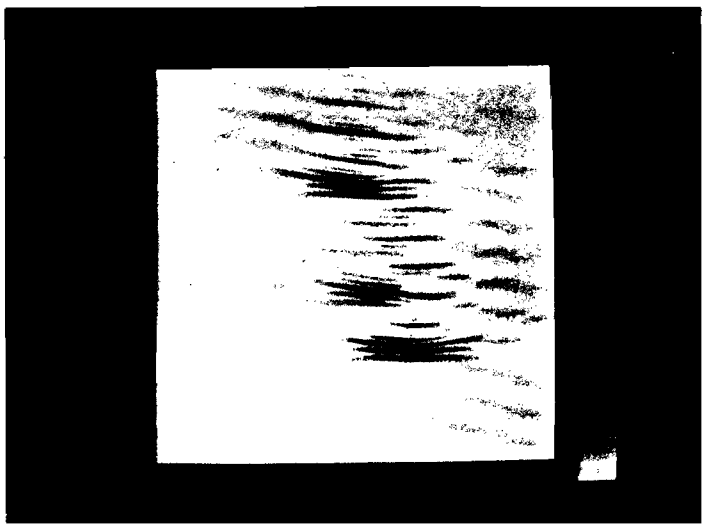

Figure 2b. Lower Three Wires in the View Grid. The image contains 512x512 pixels, which are 15 micrometers on a side.

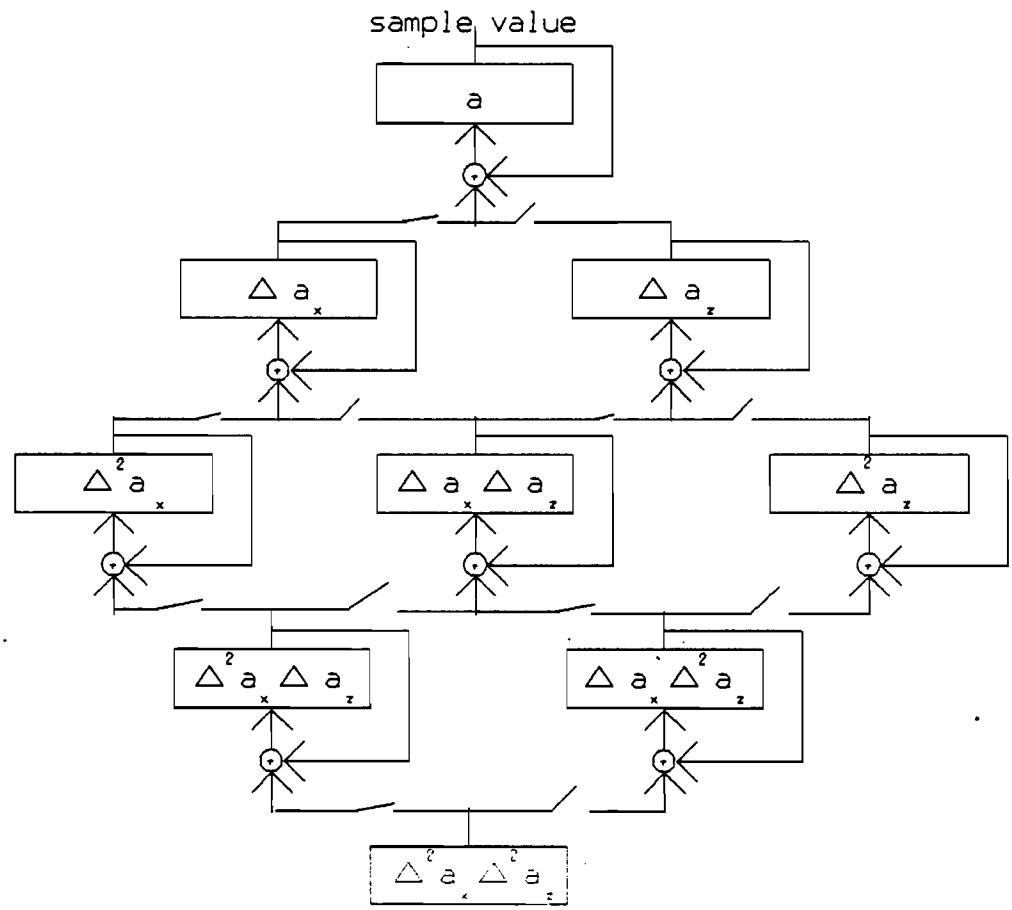

Figure 3. Time-of-Flight Calculator. Version shown is for a best-fit second-order polynomial.

B-5. The Transfer Function of Transducer Elements

Personnel: R. M. Arthur, BCL
S. R. Broadstone, BCL

Support: RR 03162

Transducer behavior must be taken into account in order to make quantitative ultrasonic measurements. Clearly, the content of the beam of a phased array is dependent on the beam profiles of the individual elements in that array. The energy transmitted or received by a transducer element is dependent on signal frequency and on the angle of propagation or incidence. We have attempted to infer transducer vibration modes from the diffraction patterns of single elements at single frequencies.

The diffraction patterns of uniform circular and rectangular pistons were calculated using the methods of Oberhettinger [1] and Lockwood and Willette [2], respectively. These methods treat an element as a collection of point sources and yield the impulse response of the element as a function of time at any field point. Previously we tried to match measured diffraction patterns on a least-squares-error basis by modelling an element as a collection of ideal subelements. The least-squares-error method fails if the location of a given field point with respect to other field points is not known to within a few μm, which is the distance over which phase changes by 1 degree in soft tissue at 3.5 MHz.

By considering single frequencies we can calculate the diffraction pattern of an element from its Fourier transform or aperture function. The magnitude of the aperture function is often taken to be the diffraction pattern in any plane parallel to the face of the transducer [3]. Actually the aperture function gives the diffraction pattern over any sphere or along any arc. Figure 1 compares the aperture function for a circular piston for the case in which the radius is 2.5 times the wavelength to the same frequency in the spectrum of the impulse response along an arc. The pattern is independent of radius. The impulse-response method is in error near the propagation axis where the effects of too low a sample rate are seen. Even though the sample rate was 400 MHz, it was not high enough to avoid aliasing. Figure 2 compares impulse response and aperture function for a rectangular piston whose width is 5 times the wavelength.

If we measure the diffraction pattern, we can then find the disturbance at the transducer face by performing an inverse Fourier transform. We plan to map the response of individual elements of an array by rotating the array within its image plane about an axis through the center of the element face. We have used this technique previously and are now in the process of measuring a 2.25 MHz circular piston and elements of 3.5 and 5 MHz, 32-element linear arrays. Rotation is performed by a stepper motor under control of the processing environment (Section B-6). Another motor fixes the range between the array element under study and a hydrophone. The excitation pulse and the pressure field recovered by the hydrophone are recorded as a function of hydrophone range and angle. Signals are sampled at 50 MHz with 8 bits of precision. Spectra are determined by Fourier transform.

1. Oberhettinger, F., "On Transient Solutions of the Baffled Piston Problem," Journal of Research of the National Bureau of Standards, (U.S.) B, vol. 65, p. 1, 1961.

2. Lockwood, J. C. and Willette, J. G., "High-Speed Method for Computing the Exact Solution for the Pressure Variations in the Nearfield of a Baffled Piston," Journal of the Acoustical Society of America, vol. 53, pp. 735-741, 1973.

3. Goodman, J. W., Introduction to Fourier Optics, McGraw-Hill, New York, 1968.

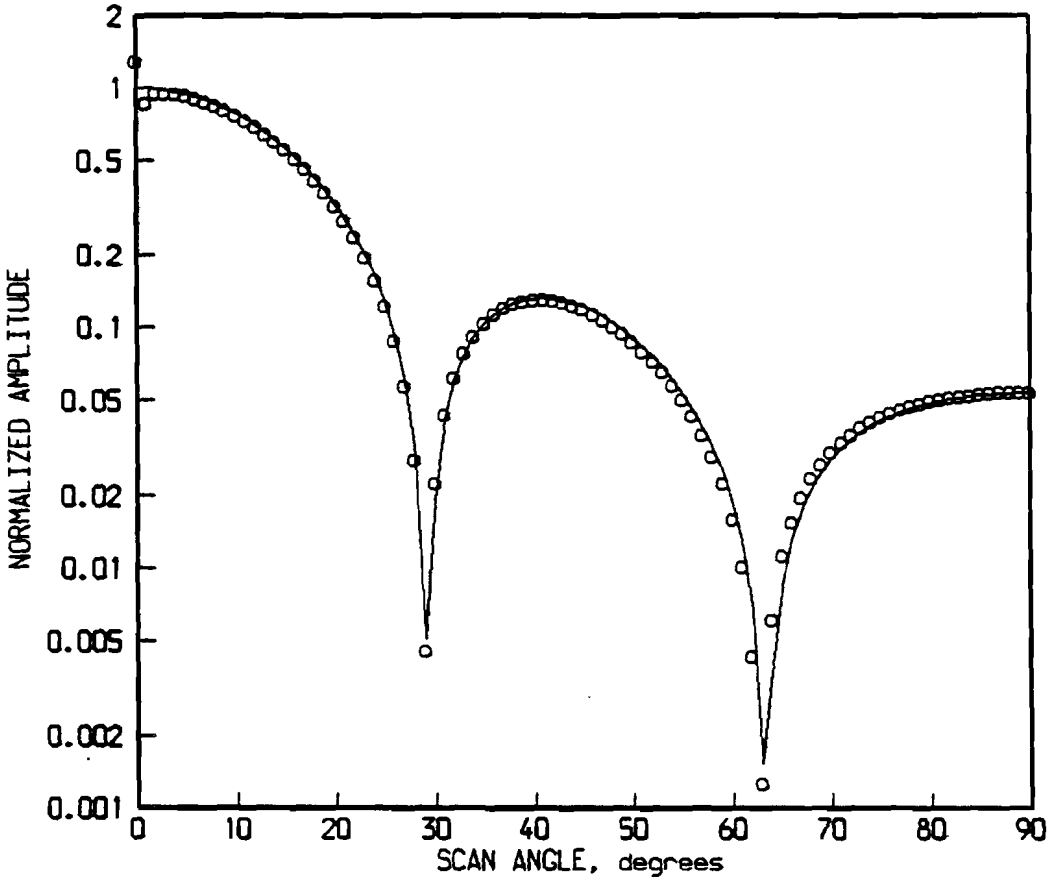

Figure 1. Diffraction pattern for a circular piston whose radius is 2.5 times the wavelength.

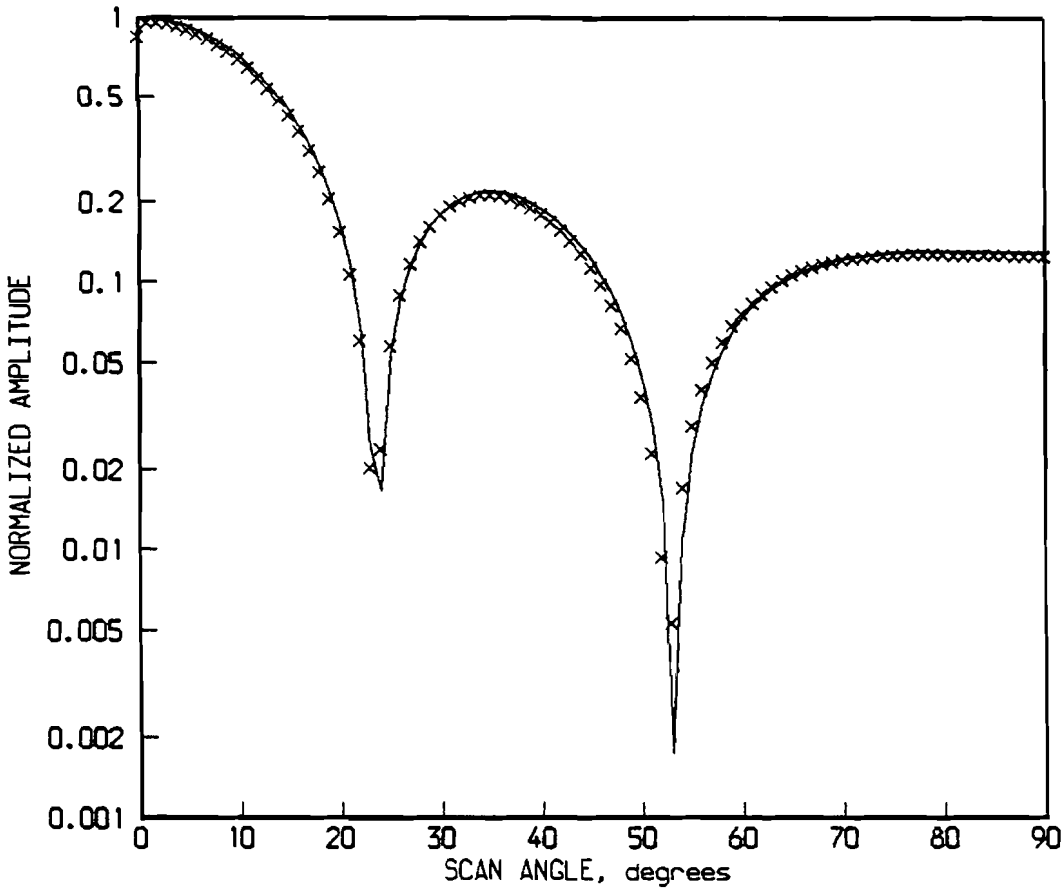

Figure 2. Diffraction pattern for a rectangular piston whose width is 5 times the wavelength.

B-6. The Processing Environment for Ultrasonic Tissue Characterization

Personnel: R. M. Arthur, BCL
S. R. Broadstone, BCL
P. H. Johnston, BCL
J. G. Miller, BCL
J. G. Mottley, BCL
L. J. Thomas, Jr., BCL

Support: RR 01362

This year we added a 190-megabyte drive and an Ethernet controller to our Masscomp MCS-537 workstation (see Figure 1). The workstation is a multiuser system for generating and manipulating images, which contains 2 megabytes of memory, special floating-point hardware, and an integral graphics processor with a high-resolution color display. The workstation is also supported by an Epson LQ-1500 dot-matrix printer, which has both draft and letter-quality modes plus graphics capability.

The new drive augmented a 50-megabyte drive and gave us sufficient storage for two- and three-dimensional graphics software, which produces CORE standard files for transfer to other systems, plus storage for more than one ultrasonic image at a time. Before we added the Ethernet controller the only way the workstation could communicate with systems outside of the processing environment was serially via a 1200 bit/second modem. The baseband Ethernet connection allows high-speed transfer of files to a computer with a tape drive for system and image backup. It makes us a closer part of the growing community of workstations in the Resource (F-1).

Previously the heart of our processing environment was a DEC LSI-11/23 microcomputer whose total memory and user partitions within memory (56 kilobytes) are far too small to hold, much less manipulate, typical ultrasonic images (256 kilobytes). The DEC LSI-11/23 is now dedicated to the acquisition of ultrasonic signals. Its main peripherals include: 1) a 111-megabyte Winchester drive; 2) an FPS 100E array processor; 3) a 9-track, industry compatible tape drive for backup storage; 4) an IEEE-488 bus for communication with the instrumentation that controls our ultrasonic transducers and collects their signals; and 5) a medium-resolution, gray-scale graphics system called digivision, which was designed and built in our laboratory. We recently installed a package called Kermit for protocol transfers via serial link to the Masscomp workstation.

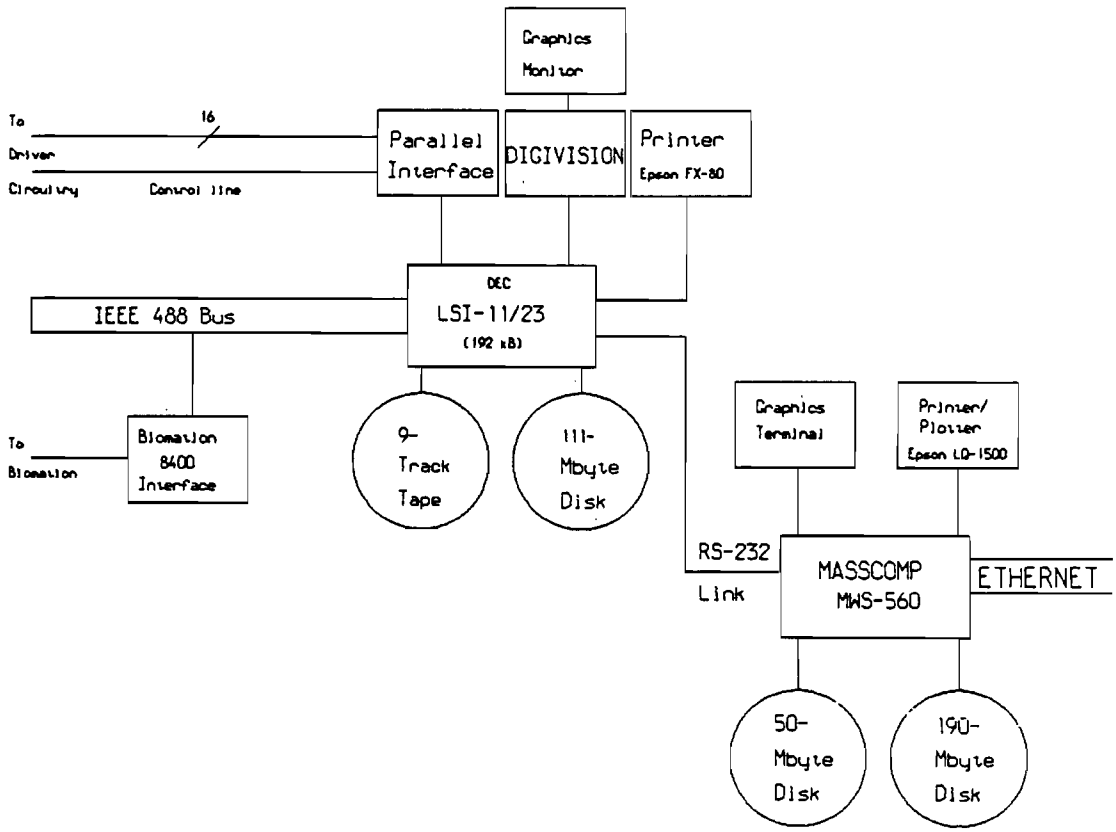

Figure 1. Ultrasound Processing Environment.

C. Quantitative Imaging: Radiation Treatment Planning

Research and development in RTP (Radiation Treatment Planning) has progressed in several important areas, including evaluation of existing treatment protocols, determining the dependence of dose deposition on atomic constituents, preliminary testing of a method for quantitative treatment verification, and preliminary development of a rapid areal dosimetry system. This work is centered in the Mallinckrodt Institute of Radiology, and represents a set of activities with the ultimate goal of providing more effective radiation therapy treatment of cancer by improving the accuracy of dose calculation and delivery.

C-1. Evaluation of High Energy Photon External Beam Treatment Planning

Personnel: J. A. Purdy, Ph.D., Radiology
B. N. Emami, M.D., Radiology
W. B. Harms, B.S., Radiology
K. E. Krippner, B.S., Radiology
J. W. Matthews, D.Sc., Computer Systems Laboratory
E. D. Slessinger, M.S., Radiology
J. W. Wong, Ph.D., Radiology

Support: RR 01380
RR 01379
NCI Contract #NO1-CM-47696

In September 1984, the National Cancer Institute (NCI) funded a three-year Multi-institutional effort to develop criteria, guidelines and methodology for the performance and evaluation of state-of-the-art high-energy photon external-beam treatment planning. This task is to be accomplished by extensive treatment planning for actual patients using state-of-the-art computerized treatment planning and imaging systems.

The collaborating institutions participating in this project are: Washington University School of Medicine in St. Louis; Massachusetts General Hospital; Memorial Sloan-Kettering Cancer Center; and the University of Pennsylvania. The project established a Working Group, which consists of medical physicists, radiation oncologists, and computer scientists from each collaborating institution, and which meets three times a year to develop strategies to accomplish the project's research goals and to review the progress of the participating institutions.

As a participant in this project, we have implemented a prototype 3-dimensional RTP system having both real-time display and advanced dose-algorithm capabilities for calculating and displaying the dose distribution and patient anatomy for non-coplanar fields and arbitrary planes in the patient. The system consists of a CMS Modulex computer interfaced to a MMS-X display system and an array processor. The computer hardware configuration is listed in Table 1.

The MMS-X display system was developed by the Washington University Computer System Laboratory to provide high-performance line-drawing graphics for biomedical applications, primarily electron-density fitting in crystallography and has been described in previous reports [1,2].

The Modulex computer is used as the input device for both the beam data and patient data and for display of the calculated dose distribution. The patient's volume of interest for planning purposes is established by viewing CT slices on the Modulex viewing monitor and using a light pen or digitizer to outline the normal structure and the target volume contours on each CT slice. The contour data are transferred to the MMS-X display system via an RS-232 interface.

After the patient data have been sent to the MMS-X, the treatment planner selects a beam type, field size and initial orientation from the various treatment-machine types available via the Modulex and sends the beam parameters to the MMS-X. The beams are represented as a configuration of lines diverging from a point source. Three planes within the beam-configuration lines are provided, one fixed at the SAD of the machine used, and the other two moveable and below the fixed plane. The system allows multi-beam displays and has several features to assist treatment planning including contour turn-on/off, dashed contours rather than continuous lines, blinking contours, and brightened contours (Figure 1). In addition, a unique feature of this display system is the capability for stereo viewing in which two images are projected on the monitor with different rotation around the screen's vertical axis. By the use of special prism glasses, a 3-dimensional stereo view is perceived.

Joy-stick control is provided for viewing the patient contours and beam arrangements as an object from any arbitrary viewing position "(Room View)." In addition, joy-stick control is provided for each of the machine motion functions, including collimator length, width and angle, gantry angle, couch angle, and couch latitude, longitude and height position "(Beam View)." During Beam View the display changes as if the observer were attached to the couch; i.e., only the manipulated beam moves on the display. It is emphasized that display manipulations for both Room View mode and Beam View are real time.

Once beam arrangements have been determined geometrically, the beam setting information is returned to the Modulex host computer where dose calculations are performed. Presently, there are two dose-calculation algorithms used in the 3-D RTP system - an effective-path-length (EPL) algorithm and the Delta-Volume (DV) algorithm [3,4]. The EPL algorithm is operational, whereas the DV algorithm is still being implemented.

Once the three dimensional dose matrix has been calculated, two-dimensional isodose information can be displayed on any planar views of the patient's anatomy via the Modulex's display (Figure 2). Hard copy of the dose distributions can be generated via a Tektronix Model 4634 device, for evaluation purposes.

Table 1

Computer Hardware Configuration of 3-D Treatment Planning System

(1) Modulex Radiation Treatment Planning Computer System
- Central Processing Unit
- 1 Mbyte 16 bit MOS CPU Memory
- 100 Mbyte CDC Disk Drive (two 25 Mbyte Fixed and two 25 Mbyte Removable)
- 6 serial ports
- Two Videographic Display Units with Light Pens
- Two Videographics Generators - 8 Colors and 24 Shades of Gray
- Two CRT Terminal (Visual V 55)
- Matrix Printer (Okidata 93)
- Digitizing Tablet, Back-lit
- Modem
- System Console
- MX-OS Operating System, MUMPS Interpreter, FORTRAN Compiler,
- MX-Assembler

(2) MMS-X Display System

- TI-980 Mini-Computer with 128 Kbytes RAM
- Pertec disc drive (4 Kbytes)
- Specialized hardware for coordinate rotation and vector display
- HP1321A display scope
- Display control console with two 3-axis joy sticks, four knobs, 10 switches and 7 buttons
- XOS operating system
- CRT terminal (Beehive B100)

(3) Array Processor System
- Numerix 432 Array Processor
  - 30 Million Floating Point operations per second
  - 64 Kbyte 32 bit words of data memory
  - DMA Interface to Micro-VAX computer
  - AREX/AVID Runtime software
  - AFOR-FORTRAN 77 Compiler
  - ARAS/LCOM Assembler/Optimizer

(3) Array Processor System (cont.)
- DEC Micro-VAX II Computer
  - 9 Mbyte RAM
  - 72 Mbyte Winchester Disk Drive (RD52)
  - 800 Kbyte Floppy (RX50)
  - 1/2 inch tape Controller
  - DMA Controller (DR11-W)
  - 9 serial ports (DHV-11)
  - Micro-VMS operating system
  - FORTRAN 77 compiler

(4) Floppy Disk CT Connection—DEC AND IBM Format
- Dual 8 inch Floppy Disk Drive, 2.5 MByte Storage
- Software for decoding CT images, contour extraction, and density calculations

(5) Magnetic Tape CT Connection — 9 track 1/2 inch tape, up to 10.5 inch reel. Magtape, 800/1600 BPI, ANSI format.
Connection to Modulex and RSX

(6) Hewlett Packard 8 Pen Color Plotter

(7) Tektronics Hard Copy Unit (Model 4634)

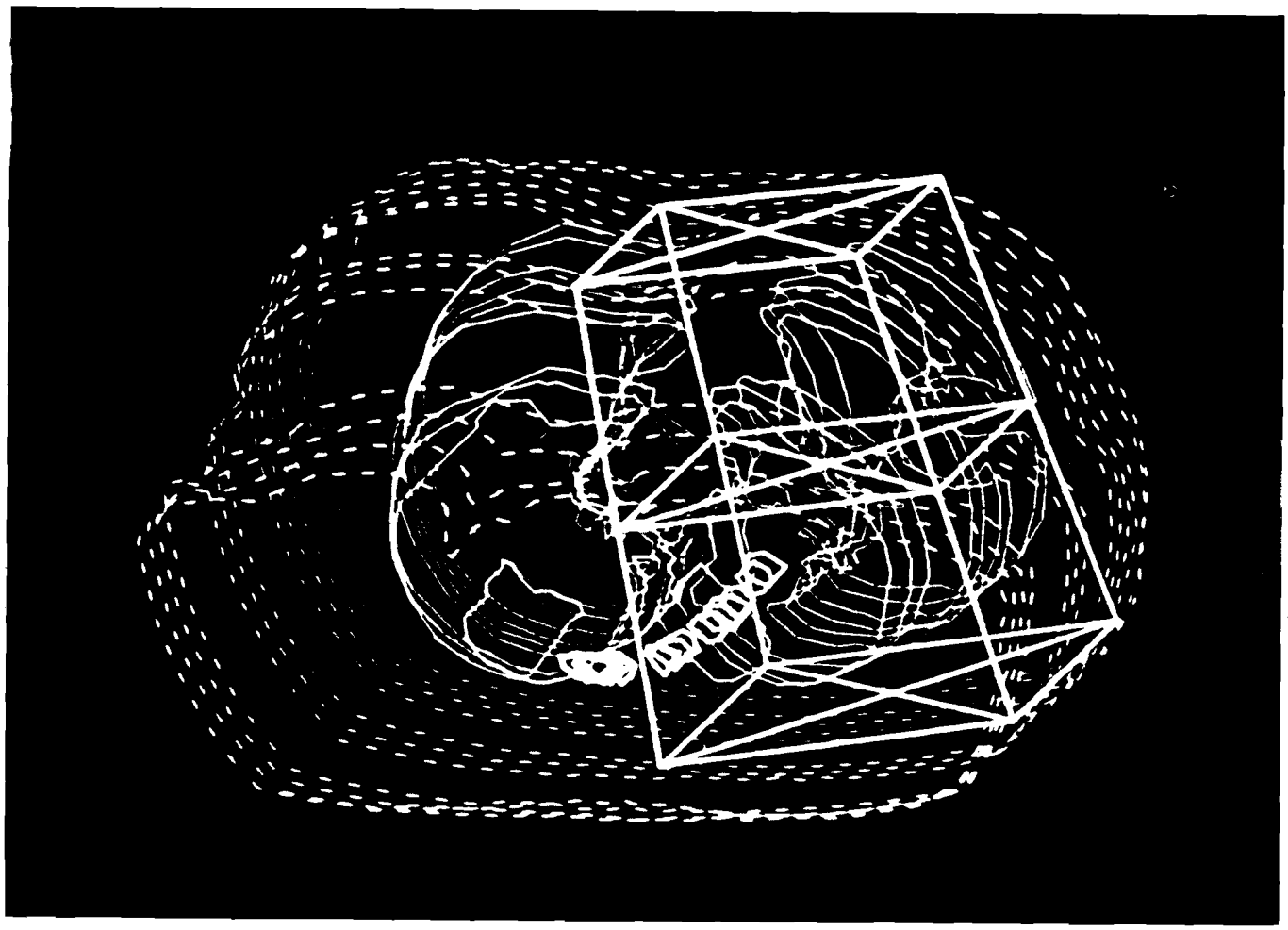

Figure 1. On the 3-D display, the patient is represented as a series of contours and the beams are represented as a configuration of lines diverging from a point source. Three planes within the beam configuration lines are provided, one fixed at the SAD of the machine used, and the other two moveable above and below the fixed plane. It is emphasized that both the "Room View" and manipulation of all beam motion with respect to patient anatomy are real-time.

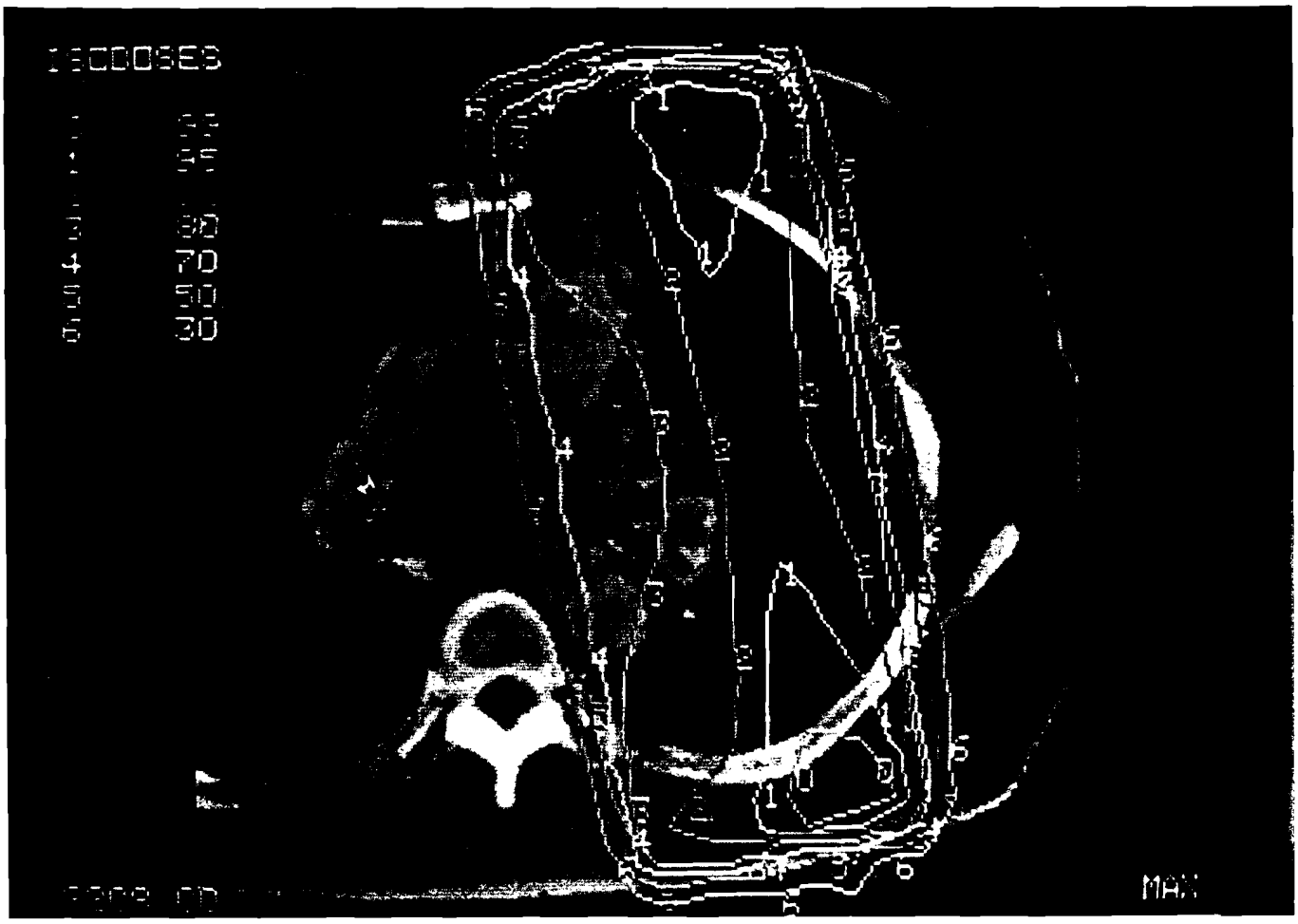

Figure 2. Display of dose distribution superimposed on 2-dimensional gray-scale CT images of patient's anatomy.

Treatment planning protocols have been developed for eight treatment sites, including nasopharynx, larynx (non-T1 or advanced), lung (T3, T4), Hodgkin's mantle, para-aortic nodes (cervix primary), prostate, rectum and breast. These protocols define the target volumes, critical structures and target doses to be used in the 3-D planning exercises. With regard to target volume designation, the Working Group defined the term "Biological Target Volume" (BTV) to mean the volume that contains gross and microscopic disease. That volume plus the additional margin that accounts for patient motion and set-up error was defined by the Working Group as the "Mobile Target Volume" (MTV) and is identical to what ICRU 29 defines as "target volume" [5].

Dosimetry experiments to verify the dose calculations performed on the 3-D RTP system were performed to isolate effects of curvature, blocks, inhomogeneities, beam quality, etc. from each other to the extent possible. The measurements were divided into three groups: basic water phantom measurements, polystyrene phantom measurements involving surface curvature and inhomogeneities and anthropomorphic phantom measurements (not completed as of this date). The measurements were performed for 4 MV and 18 MV x-ray beams generated by a Varian Clinac 4 (uranium flattening filter) and a Clinac 20 linear accelerator. The water-phantom measurements were performed using a CMS, Inc. Beam Data Acquisition Controller (BDAC), Model 3308 and Water Phantom System, Model 311. The radiation detectors used were PTW ionization chambers (type no. 23322, 0.1 cm^3). For the inhomogeneity phantom tests, Harshaw TLD-100 rods were used as the dosimeters and a Harshaw Model 2000 TL analyzer as the readout device.

The water-phantom test geometries were as follows:

Test 1: Normal beam incidence, open field. Measurements - central axis, off-axis (transverse and diagonal).

Test 2: Oblique incidence (30° to normal). Measurements - central axis, off-axis (transverse and diagonal).

Test 3: Wedged fields (45°). Measurement - central axis, off-axis (transverse and diagonal).

Test 4: Blocked fields. Measurement - under block and in the open field (transverse and diagonal).

Test 5: Elongated fields. Measurements - central axis, off-axis (short and long dimension).

The inhomogeneity-phantom test geometries were as follows: (Note: The phantoms used for these measurements were fabricated by Memorial Sloan-Kettering for use in the referenced NCI project).

Test 1: Polystyrene phantom containing a foam (low density) heterogeneity (Figure 6).

Test 2: Polystyrene phantom containing a bone-like (high density) heterogeneity (Figure 7).

Test 3: A hemi-spherical polystyrene phantom (Figure 8).

Figures 3, 4 and 5 show representative results of the comparison of dose calculations and measurements for the water-phantom tests. A total of 105 points for each of two energy beams (4-MV and 18-MV) were compared. For the EPL algorithm, 64 points for the 4-MV beam and 58 points for the 18-MV beam were outside a ± 3% difference criteria. However, all but 18 of these points were within a 3-mm radius for the 4-MV beam as were all but 29 of the points for the 18-MV beam. The majority of the points outside a 3%/3-mm criteria were in the buildup region or were for the case in which a beam modifier had been added. The disagreements in the buildup region are not surprising because of the changes in the contribution from contaminations, particularly under beam modifiers. In the other situations, the disagreements reflect the deficiency of the EPL method in scatter calculation. The Delta-Volume (DV) method was also used to calculate dose for the blocked-field case and shows significant improvement over the EPL method. Only eight out of the total 44 points were not within a 3% dose criterion (3/22 for the 4-MV beam, and 5/22 for the 18-MV beam). Disagreements were understandable in the buildup region because of the effects of contaminations, and in the diagonal positions because of the

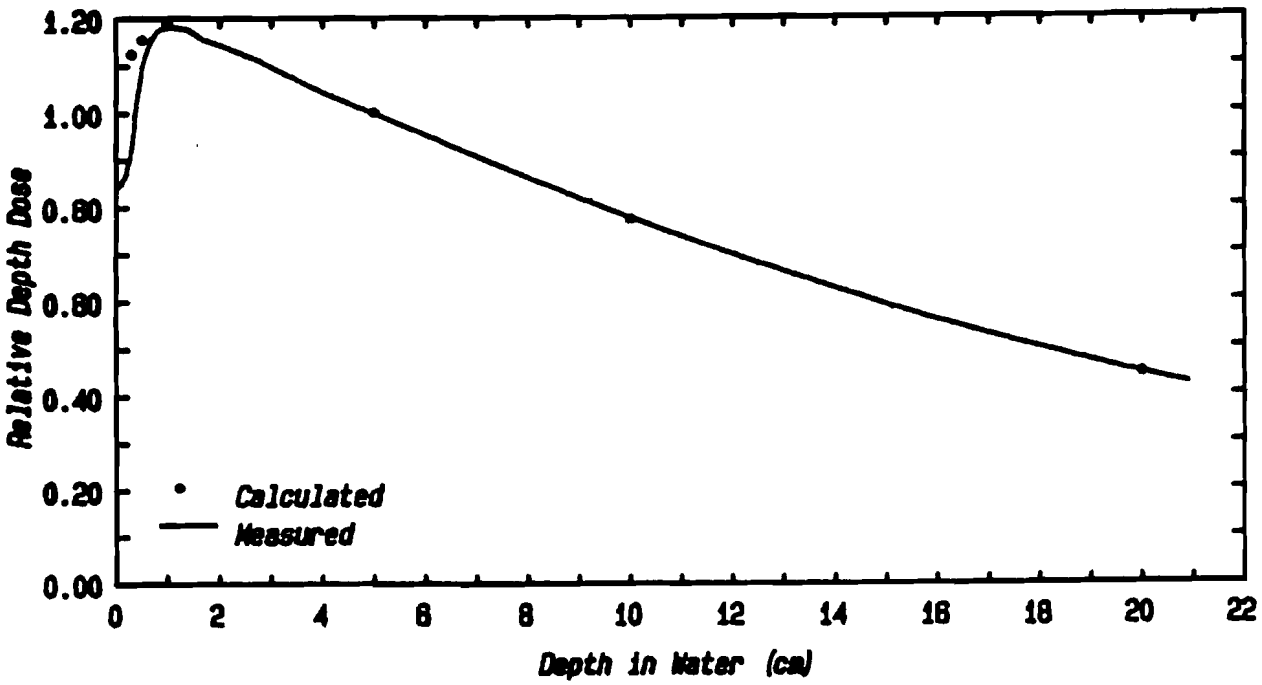

Figure 3. Central axis depth dose for a 22 cm x 22 cm, 80-cm SSD, normally incident Clinac 4 beam. The data are normalized to the dose at 5-cm depth on the central axis.

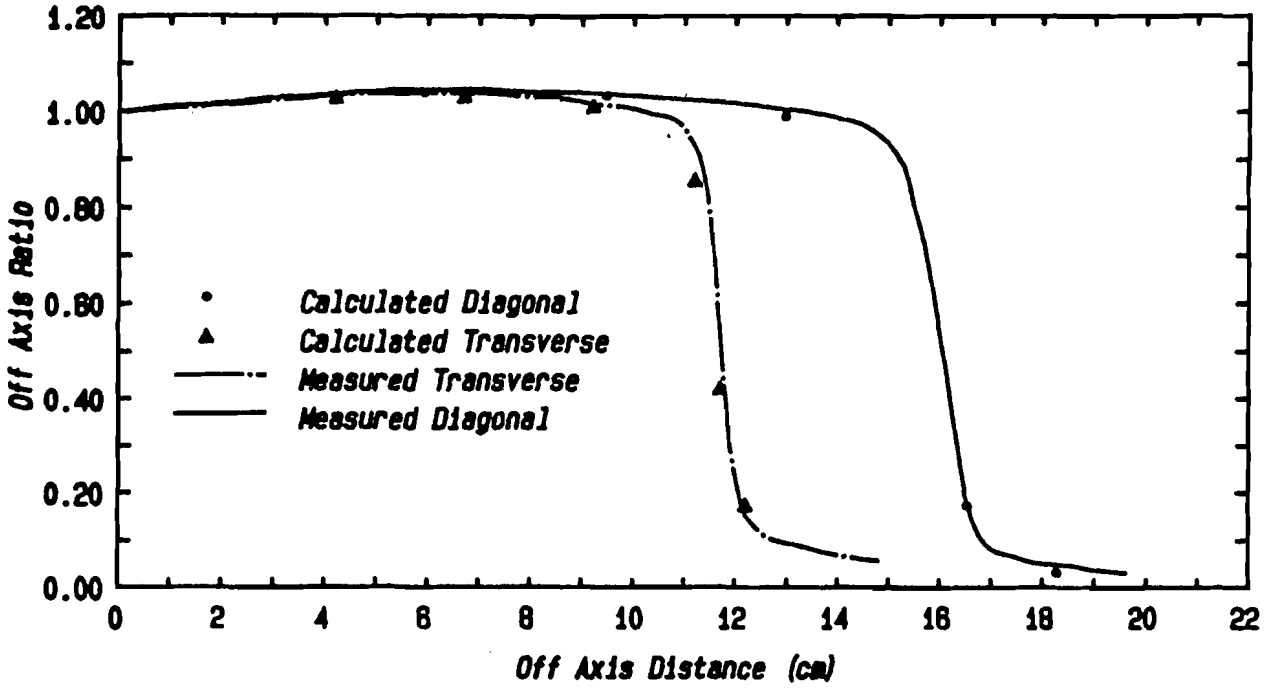

Figure 4. Transverse and diagonal profiles of a 22 cm x 22 cm, 80-cm SSD, normally incident Clinac 4 beam at 5-cm depth. The data are normalized to the dose at 5-cm depth on the central axis.

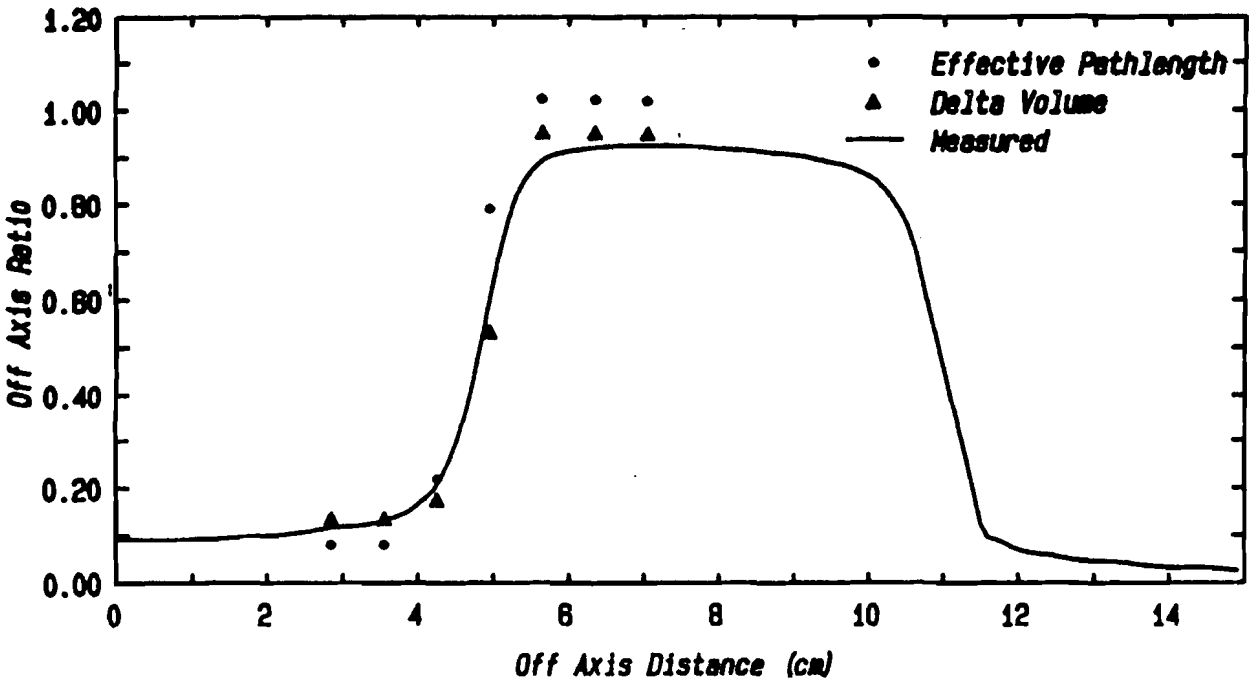

Figure 5. Diagonal profile of a 15 cm x 15 cm, 80 cm SSD, normally incident Clinac 4-beam with a 7 cm x 7 cm central block. The data are normalized to the open field dose at 5 cm depth on the central axis.

possible measurement error due to chamber-volume effect. The remaining two points reflect the fact that the DV calculations slightly overestimate scatter dose. This is because the altered primary intensities are not incorporated in the multiple-scatter dose calculations based on sector integrations. We plan to correct this deficiency by converting the multiple-scatter-air-ratio values and including their summations in the ray-trace loop of the calculations.

The polystyrene/foam phantom (Figure 6, 0.1 density foam) tests stressed electronic equilibrium even at the lower 4-MV x-ray energy. Review of the data showed that the calculations did not agree with measurements, especially in the foam. In the 4-MV case, agreement was achieved even in the foam under conditions for which electronic equilibrium was re-established. The other points showed relatively good agreement (Table 2).

The polystyrene/bone phantom (Figure 7) test showed good agreement in the 4-MV case with distinct disagreement at interface positions. This may reflect the inadequate resolution of sampling and calculation rather than algorithm accuracy. For the 18-MV case, calculations consistently underestimated measurements in the bone, illustrating the inability of the present algorithms to account for the effect of changes in atomic constituents on pair production (Table 3).

Relatively poor agreement was observed for the polystyrene/hemisphere phantom (Figure 8) as it tested the ability of the calculations to account for missing tissue and for electronic equilibrium. In addition, the steepness of the gradient of the hemispherical surface further stressed the sampling resolution of the calculation (Table 4).

Other areas that this research effort will address are the incorporation of uncertainty analysis into the treatment planning process and the numerical evaluation and scoring of treatment plans. Methods are being developed to assist the clinician, clinical physicist and dosimetrist in evaluating the large amount of data a three-dimensional dose distribution provides, such as dose-volume histograms, dose uniformity parameters, and isodose distributions superimposed on any arbitrary plane(s) in the irradiated volume.

Regarding uncertainty analysis, we are attempting to identify sources of uncertainty, assessing their magnitude and estimating the impact on the calculated dose distribution pertaining to the eight disease sites being studied. The point is that the implicit uncertainty in the isodose value shown is often not heeded by the clinician and can lead to unintentional over- or under-dosing.

Results based on each institution's efforts will be incorporated into a final report which is to include a definition of state-of-the-art treatment planning, and provide insight on the role of several areas in treatment planning including CT, and other diagnostic modalities, tissue inhomogeneity corrections, 3-D dose calculations, 3-D displays, uncertainty analysis, and numerical evaluation and scoring of treatment plans.

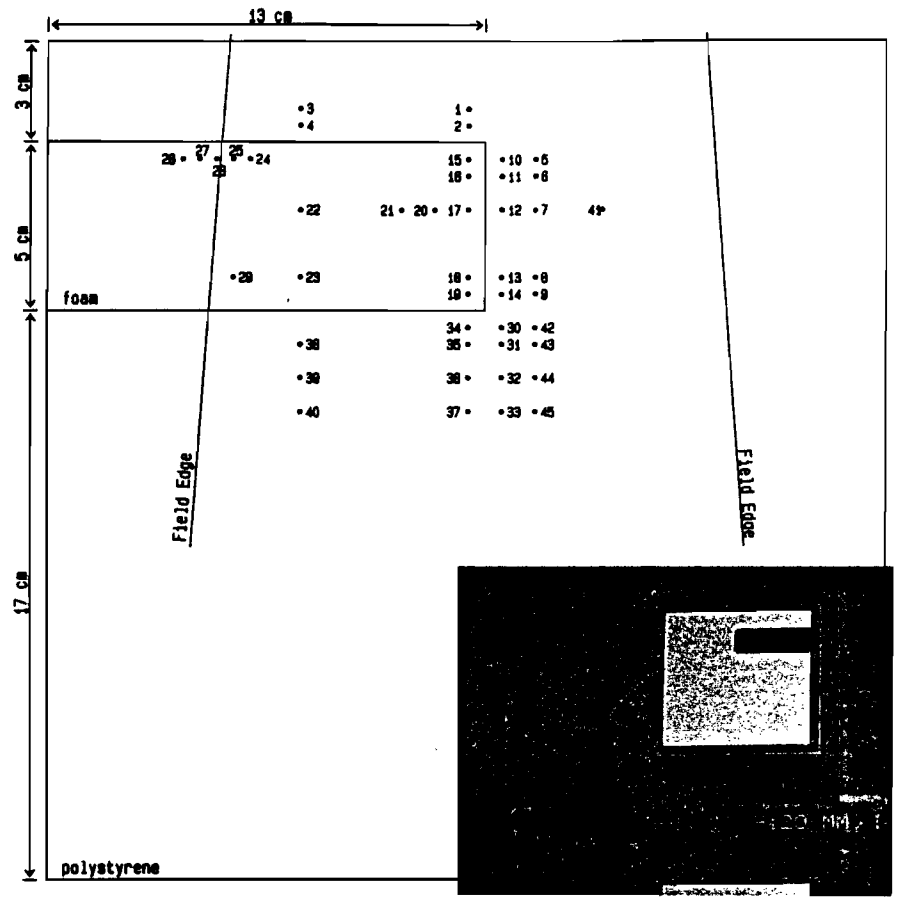

Figure 6. Polystyrene/Foam Phantom

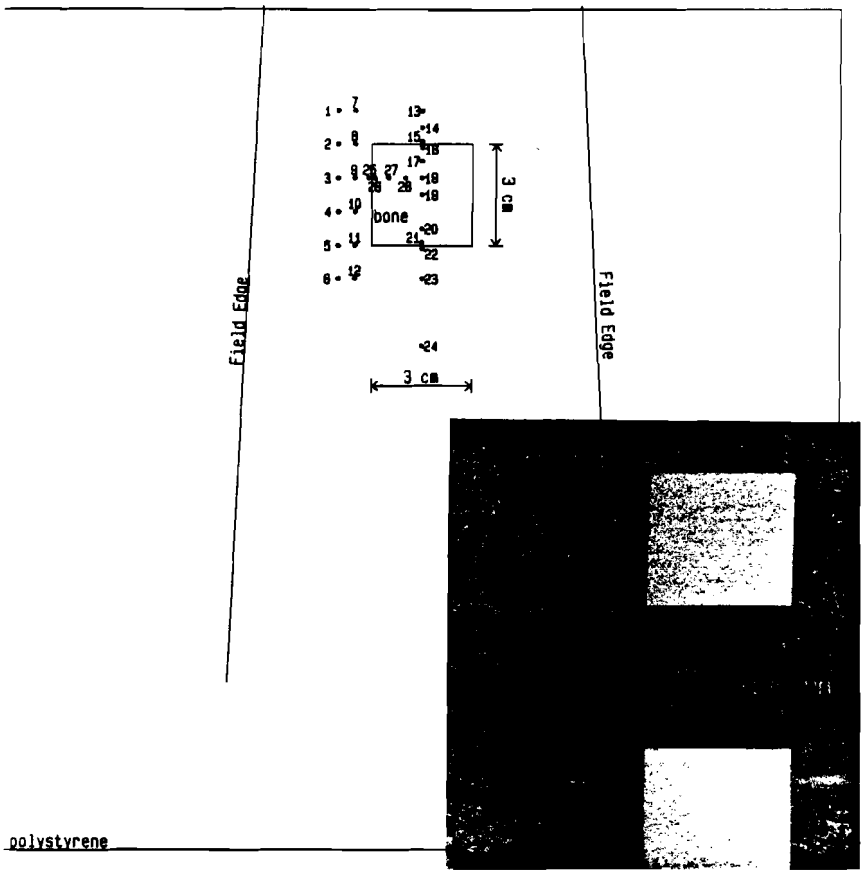

Figure 7. Polystyrene/Bone Phantom

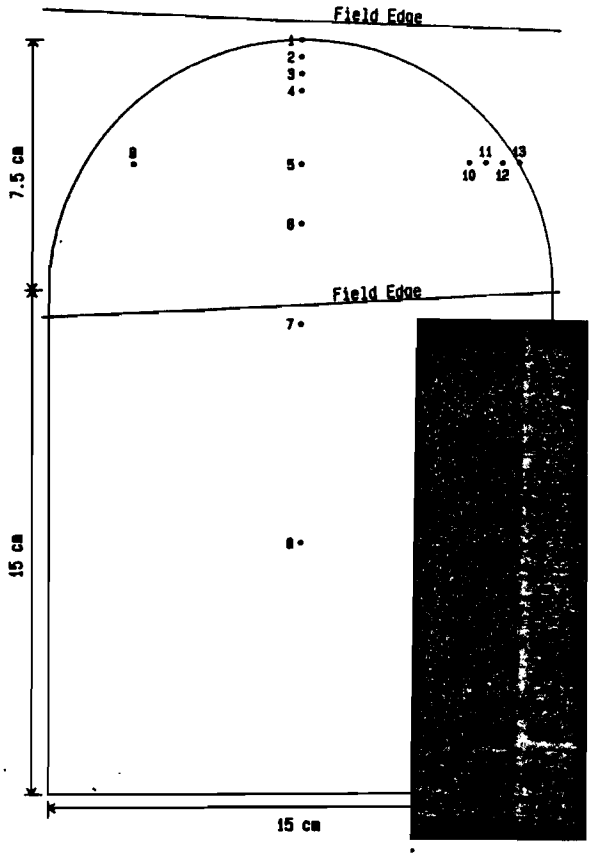

Figure 8. Polystyrene/Hemisphere Phantom

Table 2

Comparison of Dose Calculation and Measurement
for Polystyrene/Foam Phantom

MACHINE: Clinac 4 (Uranium) ENERGY: 4 MV

TEST 1: Polystyrene/Foam Phantom
Field Size 15cm x 15cm at Isocenter (80cm SAD).
5cm overlying material.

				Effective Pathlength Calculation			Delta Volume Calculation		
Point #	Measured Dose (cGy)	Uncertainty (2 S.D.)(cGy)	Normalized Measured Dose	Calculated Dose (cGy)	Normalized Calculated Dose	Difference	Calculated Dose (cGy)	Normalized Calculated Dose	Difference
1	212.0	2.8	1.125	217.1	1.152	-0.027	222.8	1.157	-0.032*
2	217.3	2.0	1.153	212.6	1.128	0.025	216.4	1.124	0.029
15	190.7	1.4	1.012	204.8	1.087	-0.075*	204.9	1.064	-0.052*
16	182.9	1.4	0.971	201.5	1.070	-0.099*	204.0	1.060	-0.089*
17	184.3	1.8	0.978	195.6	1.038	-0.060*	198.3	1.030	-0.052*
18	180.7	2.6	0.959	184.3	0.978	-0.019	188.7	0.980	-0.021
19	168.0	1.4	0.892	181.2	0.962	-0.070*	186.6	0.969	-0.077*
34	178.2	2.8	0.946	173.7	0.922	0.024	183.3	0.952	-0.006
35	170.2	1.7	0.903	169.4	0.899	0.004	177.7	0.923	-0.020
36	166.3	1.9	0.883	160.3	0.851	0.032*	168.5	0.875	0.008
37	158.6	1.6	0.842	151.9	0.806	0.036*	160.7	0.835	0.007
3	231.1	5.1	1.127	224.0	1.189	0.038*	228.7	1.188	-0.061*
4	222.6	5.8	1.182	219.3	1.164	0.018	221.1	1.149	0.033*
22	193.4	4.9	1.027	202.5	1.075	-0.048*	196.0	1.018	0.009
23	174.1	3.9	0.924	191.3	1.015	-0.091*	183.3	0.952	-0.028*
38	179.3	3.7	0.952	175.9	0.934	0.018	174.8	0.908	0.044
39	165.1	4.0	0.876	166.9	0.886	-0.010	167.1	0.868	0.008
40	161.1	3.9	0.855	157.7	0.837	0.018	159.1	0.826	0.029
10	206.5	3.2	1.096	204.0	1.083	0.013	205.9	1.070	0.026
11	201.8	2.7	1.071	199.9	1.061	0.010	200.2	1.040	0.031*
12	187.5	1.7	0.995	192.3	1.021	-0.025	188.2	0.978	0.017
13	169.0	2.7	0.897	178.0	0.945	-0.048*	165.7	0.861	0.036*
14	163.2	1.5	0.866	174.3	0.925	-0.059*	160.7	0.835	0.031*
30	153.8	1.8	0.816	165.9	0.881	-0.064*	152.8	0.794	0.022
31	146.8	1.9	0.779	161.4	0.857	-0.077*	148.5	0.771	0.008
32	142.4	1.4	0.756	152.6	0.810	-0.054*	140.5	0.730	0.026
33	134.8	1.8	0.711	144.2	0.765	-0.054*	134.0	0.696	0.015
5	205.8	4.9	1.092	202.9	1.077	0.015	209.4	1.088	0.004
6	203.8	4.8	1.082	198.0	1.051	0.031*	203.7	1.058	0.024
7	188.4	3.8	1.000	188.4	1.000	0.000	192.5	1.000	0.000
8	172.9	4.0	0.918	169.6	0.900	0.018	170.1	0.884	0.034*
9	164.3	3.7	0.872	165.3	0.877	-0.005	164.7	0.856	0.016
42	152.9	3.6	0.812	156.5	0.831	-0.019	155.3	0.807	0.005
43	147.7	3.4	0.784	152.0	0.807	-0.023	150.9	0.784	0.000
44	143.0	3.2	0.759	143.5	0.762	-0.003	141.9	0.737	0.022
45	133.1	3.4	0.706	135.4	0.719	-0.012	132.8	0.690	0.016
41	192.3	4.8	1.021	187.6	0.996	0.025	196.0	1.018	0.003
24	199.1	4.9	1.057	205.8	1.092	-0.036*	199.8	1.038	0.019
25	180.9	5.7	0.960	187.8	0.997	-0.037*	169.0	0.878	0.082*
26	104.1	3.5	0.553	87.9	0.467	0.086*	80.6	0.419	0.134*
27	34.4	1.2	0.183	26.4	0.140	0.042*	17.6	0.091	0.092*
28	20.4	0.8	0.108	14.5	0.077	0.031*	9.9	0.051	0.057*
29	161.5	5.0	0.857	180.6	0.959	-0.101*	171.3	0.890	-0.033*
20	187.9	4.8	0.997	199.5	1.059	-0.062	196.2	1.019	-0.062
21	189.1	4.7	1.004	200.5	1.064	-0.061*	196.2	1.019	-0.015

Table 3

Comparison of dose calculation and measurement
for polystyrene/bone phantom.

MACHINE: CLINAC 20 ENERGY: 18 MV

TEST 2: POLYSTYRENE/BONE PHANTOM
FIELD SIZE 10CM X 10CM AT ISOCENTER (100CM SAD),
5CM OVERLYING MATERIAL.

DELTA VOLUME CALCULATION

POINT #	MEASURED DOSE (cGy)	UNCERTAINTY (2 S.D.)(cGy)	CALCULATED DOSE (cGy)	NORMALIZED MEASURED DOSE	NORMALIZED CALCULATED DOSE	DIFFERENCE
1	227.7	10.7	224.3	1.053	1.040	0.013
2	221.7	9.0	222.3	1.025	1.031	-0.006
3	216.2	9.2	215.7	1.000	1.000	0.000
4	211.8	9.4	208.8	0.980	0.968	0.012
5	200.3	8.3	200.9	0.926	0.931	-0.005
6	190.0	8.5	192.7	0.879	0.893	-0.014
7	220.7	9.0	223.2	1.021	1.035	-0.014
8	224.3	9.6	221.4	1.037	1.026	0.011
9	220.3	9.1	215.3	1.019	0.998	0.021
10	217.6	10.2	208.4	1.006	0.966	0.040*
11	208.9	9.3	200.7	0.966	0.930	0.036*
12	194.5	7.9	192.5	0.900	0.892	0.008
13	224.9	9.1	221.7	1.040	1.028	0.012
14	219.1	8.5	221.2	1.013	1.025	-0.012
15	220.2	8.6	219.9	1.019	1.019	0.000
16	229.4	1.8	219.9	1.061	1.019	0.042*
17	236.3	1.8	216.4	1.093	1.003	0.090*
18	228.2	1.7	211.1	1.056	0.979	0.077*
19	229.4	2.3	207.1	1.061	0.960	0.101*
20	214.6	1.3	196.5	0.994	0.911	0.083*
21	205.2	1.5	190.9	0.949	0.885	0.064*
22	201.7	8.3	190.9	0.933	0.885	0.048*
23	187.7	8.7	181.9	0.868	0.843	0.025
24	163.9	6.6	165.3	0.758	0.766	-0.008
25	225.6	10.6	213.3	1.043	0.989	0.054*
26	227.0	10.2	213.3	1.050	0.989	0.061*
27	226.7	0.9	211.3	1.049	0.980	0.069*
28	228.0	1.5	211.1	1.055	0.979	0.076*

Table 4

Comparison of dose calculation and measurement
for polystyrene/hemisphere phantom.

MACHINE: CLINAC 20 ENERGY: 18 MV

TEST 3: POLYSTYRENE/HEMISPHERE PHANTOM — EFFECTIVE PATHLENGTH CALCULATION
FIELD SIZE 8.5CM X 8.5CM AT ISOCENTER (100CM SAD),
7.5CM OVERLYING MATERIAL.

POINT #	MEASURED DOSE (cGy)	UNCERTAINTY (2 S.D.)(cGy)	CALCULATED DOSE (cGy)	NORMALIZED MEASURED DOSE	NORMALIZED CALCULATED DOSE	DIFFERENCE
1	132.9	2.9	127.7	0.652	0.627	0.026
2	198.6	4.2	190.0	0.975	0.933	0.042*
3	208.1	3.6	207.4	1.022	1.018	0.003
4	210.8	4.3	208.4	1.035	1.023	0.012
5	203.7	4.0	203.7	1.000	1.000	0.000
6	205.9	4.2	201.7	1.011	0.990	0.021
7	32.4	.4	29.1	0.159	0.143	0.016
9	166.7	3.7	166.6	0.818	0.818	0.000
10	208.6	4.7	193.7	1.024	0.951	0.073*
11	193.3	4.2	172.7	0.949	0.848	-0.101*
12	154.4	3.5	136.4	0.758	0.670	-0.088*
13	70.7	0.7	91.9	0.347	0.451	-0.104

MACHINE: CLINAC 20 ENERGY: 18 MV

TEST 3: POLYSTYRENE/HEMISPHERE PHANTOM — DELTA VOLUME CALCULATION
FIELD SIZE 8.5CM X 8.5CM AT ISOCENTER (100CM SAD),
7.5CM OVERLYING MATERIAL.

POINT #	MEASURED DOSE (cGy)	UNCERTAINTY (2 S.D.)(cGy)	CALCULATED DOSE (cGy)	NORMALIZED MEASURED DOSE	NORMALIZED CALCULATED DOSE	DIFFERENCE
1	132.9	2.9	104.5	0.652	0.507	0.145*
2	198.6	4.2	225.6	0.975	1.094	-0.119*
3	208.1	3.6	224.2	1.022	1.087	-0.065*
4	210.8	4.3	221.1	1.035	1.072	-0.037*
5	203.7	4.0	206.3	1.000	1.000	0.000
6	205.9	4.2	201.8	1.011	0.978	0.033*
7	32.4	.4	24.1	0.159	0.117	0.042*
9	166.7	3.7	162.8	0.818	0.789	0.029
10	208.6	4.7	209.3	1.024	1.015	0.009
11	193.3	4.2	181.2	0.949	0.878	0.071*
12	154.4	3.5	125.8	0.758	0.610	0.148*
13	70.7	0.7	6.6	0.347	0.032	0.315*

1. Barry, C. D. and McAlister, J. P., Computational Crystallography, D. Sayre, ed., Oxford University Press, 1982.

2. Barry, C. D., Molnar, C. E., and Rosenberger, F. U., "MMS-X Molecular Modeling System," Technical Memorandum No. 229, Washington University, St. Louis, MO, 1977.

3. Wong, J. W., and Henkelman, R. M., "A New Approach to CT-Pixel-Based Photon Dose Calculations in Heterogeneous Media," Medical Physics, vol. 10, pp. 199-208, 1983.

4. Wong, J. W., Slessinger, E. D., Rosenberger, F. U., Krippner, K., and Purdy, J. A., "The Delta-Volume Method for 3-Dimensional Photon Dose Calculations," IEEE Computer Society Press, pp. 26-30, 1984.

5. International Commission on Radiation Units and Measurements (ICRU) Report 29, pp. 45-50, Washington, DC, 1981.

C-2. The Dependence of Dose Deposition on Atomic Constituents in the Medium

Personnel: J. W. Wong, Ph.D., Radiology
S. M. Hancock, M.S., Medical College of Ohio
S. P. Monthofer, Radiology
J. A. Purdy, Ph.D., Radiology
C. Y. Yu, M.S., Radiology

Support: CA 41574
Mallinckrodt Institute of Radiology

The study of dose perturbations due to the presence of inhomogeneities in a high-energy photon beam provides important information in our continuing effort to develop a unified method of photon dose calculation. Our previous measurements demonstrate that as photon energy increases, changes in the atomic constituents affect both pair-production and multiple coulomb electron scatterings to the extent that the resultant contributions in dose can be larger than 5% of the total dose [1]. It becomes imperative that we understand the physics of the problem so that an adequate model can be developed.

During the past year, we have adapted our water-tank apparatus for in-air measurements. The purpose of the study is to elucidate the spatial energy deposition distribution due to the ejected secondary electrons from photon interactions in an irradiated target as a function of its size and atomic number. The dose distributions in-air around a small "ring-shaped" target were measured for the 18MV x-ray beam as we cycled the ring above and below the ionization chamber. No build up material was used for the chamber so as to minimize the secondary photon contribution to the signal. Figure 1 shows the results for copper rings of various thickness but at approximately the same radial distance from the detector axis. The

results, represented as 'normalized cross-sections', have been corrected for inverse square and normalized with respect to the 45° value.

Also shown in Figure 1 are the theoretical cross-sections for the ejected electron fluence from the Compton interactions in an ideal point target. The calculations have incorporated spectral distribution for the 18MV x-ray beam deduced from published data [2]. Of interest is the fact that Compton interactions do not produce electrons at larger than 90°. The data reveal that as the ring size increases, the cross-section curve becomes shallower, reducing the forward small-angle component while increasing the large-angle component. This presumably is due to increased multiple coulomb electron scattering. The large-angle component may also be enhanced by those charged particles produced from pair-production interactions which have a spatial distribution that, although mostly forward, span from 0° to 180°.

These initial studies provide important information for the modeling of photon-electron transport. In the coming year, we plan to refine our measurements by constructing an apparatus in which a very small semiconductor diode, or scintillator-tipped detector can be moved around a stationary target irradiated by a small horizontal photon beam. This approach will provide finer spatial resolution measurements and eliminate the ambiguity of changing contaminations in the photon beam. Furthermore, an explicit model will be developed to describe the results for both our previous 'in-water' and the present 'in-air' studies. We will attempt to calculate the results in terms of energy deposition rather than the arbitrary normalized data since there is generally no simple one-to-one relationship between measured energy deposition and ejected particle fluence, and the normalized approach does not readily provide direct delineation of the effects of ring size and the contribution from pair-production.

1. Yu, C. Y., Wong, J. W., and Purdy, J. A., "Photon Dose Perturbations Due to Small Inhomogeneities," submitted for publication in Medical Physics 1986.

2. Mohan, R., and Chui, C., "Energy and Angular Distributions of Photons from Medical Linear Accelerators," Medical Physics, vol. 12, pp. 592-597, 1985.

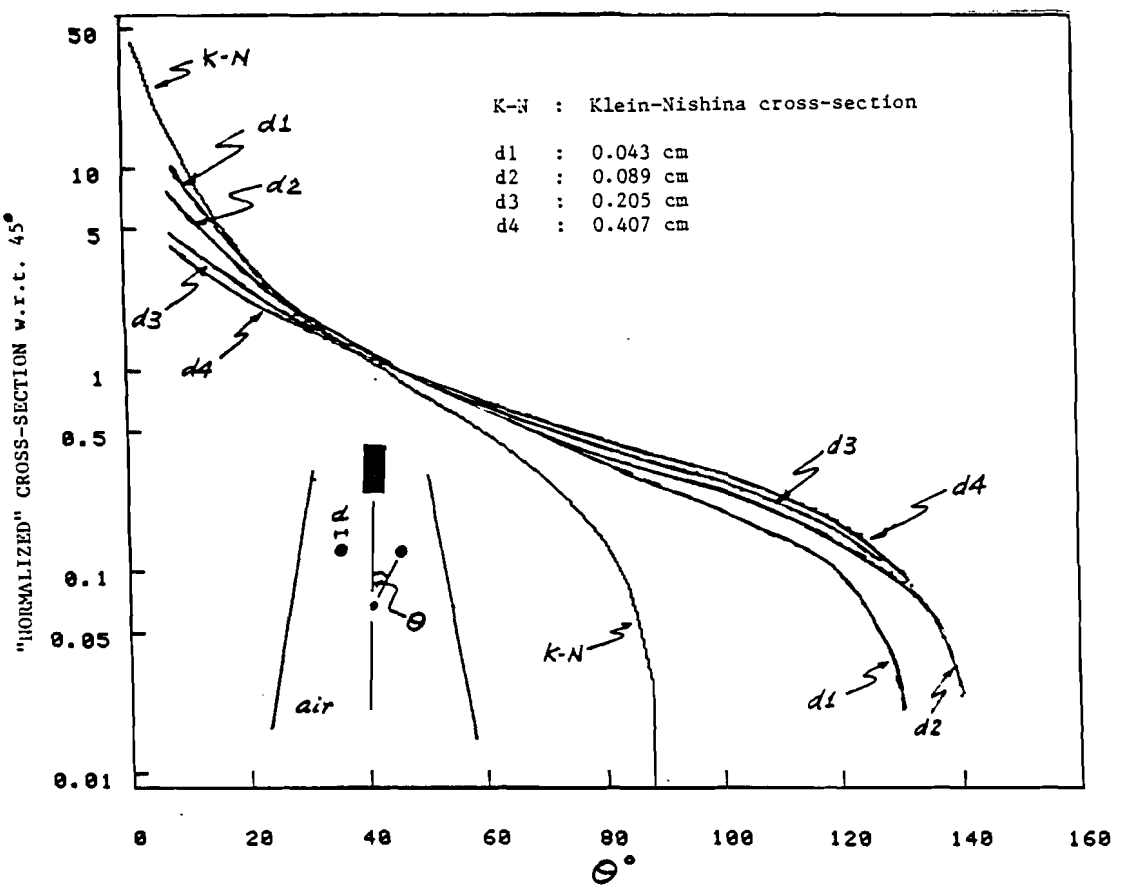

Figure 1. "Normalized" cross-section for ejected electron vs scatter angle. The diameter of the various cooper rings is denoted by d. Each curve is normalized to its own value at 45°. Rigorously, the measured data are not true cross-sections because there is no simple conversion from energy measurements to number fluence.

C-3. Clinical Application of a Quantitative Treatment Verification Approach

Personnel: J. W. Wong, Ph.D., Radiology
W. B. Harms, B.S., Radiology
R. E. Hermes, BCL
T. Roy, M.D., St. Louis Medical Center
E. D. Slessinger, M.S., Radiology
M. W. Vannier, M.D., Radiology

Support: RR 01380
Mallinckrodt Institute of Radiology

Throughout our effort to develop an accurate method of dose calculations for radiation treatment planning, it has been our concern that there is a paucity of verification techniques to ensure the proper implementation of an optimized treatment plan, particular to the dose calculated. The customary practice is to examine the measured transmitted intensity distributions at the beam-exit side of the patient (i.e. portal image) based on usually low-contrast, anatomical landmarks.

While portal imaging has improved during the past few years with the advent of digital radiographic techniques [1,2], the approach basically verifies only geometric alignment. Repeated comparisons of the portal images over the course of treatment only verify reproducibility of the alignment. Typical portal images do not detect treatment errors such as misplaced filters or wedges.

Three years ago, we proposed that an accurate dose calculation can also serve as a means to achieve quantitative dosimetric verification. The predicted transmitted planar (or 2D) portal dose distribution on the beam-exit-side of the patient should correlate with measurements, provided that the 3D CT information used in treatment planning, as an a priori requirement, truthfully represents the patient under treatment.

As feasibility studies, we employed our delta-volume algorithm for cobalt-60 irradiations in well controlled geometries. The studies have been divided into three phases. Phase 1: Delta-volume cobalt-60 calculations have been shown to agree with measurements in a stringent modular plastic phantom consisting of interchangeable cork and aluminum units. The calculated transmitted dose distribution agreed with fixed-point high precision thermoluminescent dosimetry (TLD) measurements to 1.8% $\pm$ 1.4%. Phase 2: CT scan data of the chest portion of the Rando phantom were used for 3D calculations. Within the phantom, calculations agreed with TLD measurements to 0.2% $\pm$ 2.5%. The calculated 2D portal dose distribution agreed with that deduced from scanning ionization measurements to 1.0% $\pm$ 2.4%. Phase 1 and 2 studies have been reported in previous progress reports. The results demonstrate that under well controlled conditions, a calculated portal image agrees with measurements.

During the past year, we have completed the final phase of our feasibility studies which involved an actual clinical treatment. 3D CT-based calculations were used to predict the portal dose image of a patient treated for lung cancer. The patient was immobilized. An exposed portal film with a digitized pixel resolution of about 0.4 mm-squared was

converted to dose by calibrating with 35 judiciously positioned TLDs irradiated simultaneously during treatment. Point calculations differed from the 35 TLD measurements by 1.2% ± 10.0%, indicating the inadequacy of fixed-point comparisons for this more difficult arrangement. The portal film image was useful to identify a misalignment of the TLDs with respect to the calculational grid. Initial comparison of the film dosimetry data with 238 calculation points showed a difference of -1.6% ± 6.6%. More critical profile analysis suggested a slight 4 mm translational misregistration comparable to a recent report on geometric alignment error [3]. Adjustment of the portal calculation grid yielded a much smaller difference of -0.3% ± 3.1%. However, local regions of large systematic differences (>±5%) remained. Figure 1 shows the comparison of the measured and calculated dose values expressed as a histogram distribution of percent difference of the measured values. Figures 2a and 2b show the calculated and measured portal images as portal isodose contour plots.

The results of the studies are encouraging and provide much insight into the uncertainties of clinical dose predictions. Planar portal dose distribution comparison was superior to point verification and stresses the importance of calculation at higher spatial resolution of the order of a few mm. Useful quantitative treatment verification requires in-depth understanding of the many uncertainty factors associated with calculation, measurement, geometric setup and patient motion. It is also not clear whether a 2-dimensional exit-dose comparison gives adequate assurance on the accuracy of the 3-dimensional dose distribution delivered to the patient. Finally, for this approach to be practical for clinical use, a rapid area-dosimetry system needs to be developed. It is our intention to address these issues in the coming year.

1. Leong, J., "A Digital Image Processing System for High Energy X-Ray Portal Images," Physics in Medicine and Biology, vol. 29, pp. 1527-1535, 1984.

2. Partowmah, M., Lam, W. C., and Lam, K. S., "Portal Verification with an Electronic Imaging System," Work-in-Progress Abstracts, Medical Physics, vol. 12, supplement, 1985. Presented at the 27th Annual Meeting of the AAPM, Seattle, 1985.

3. Partowmah, M., Lam, K. S., and Lam, W. C., "On-line Measurement of Geometric Errors in External Beam Radiotherapy," Medical Physics, vol. 13, p. 575, 1986 (abstract).

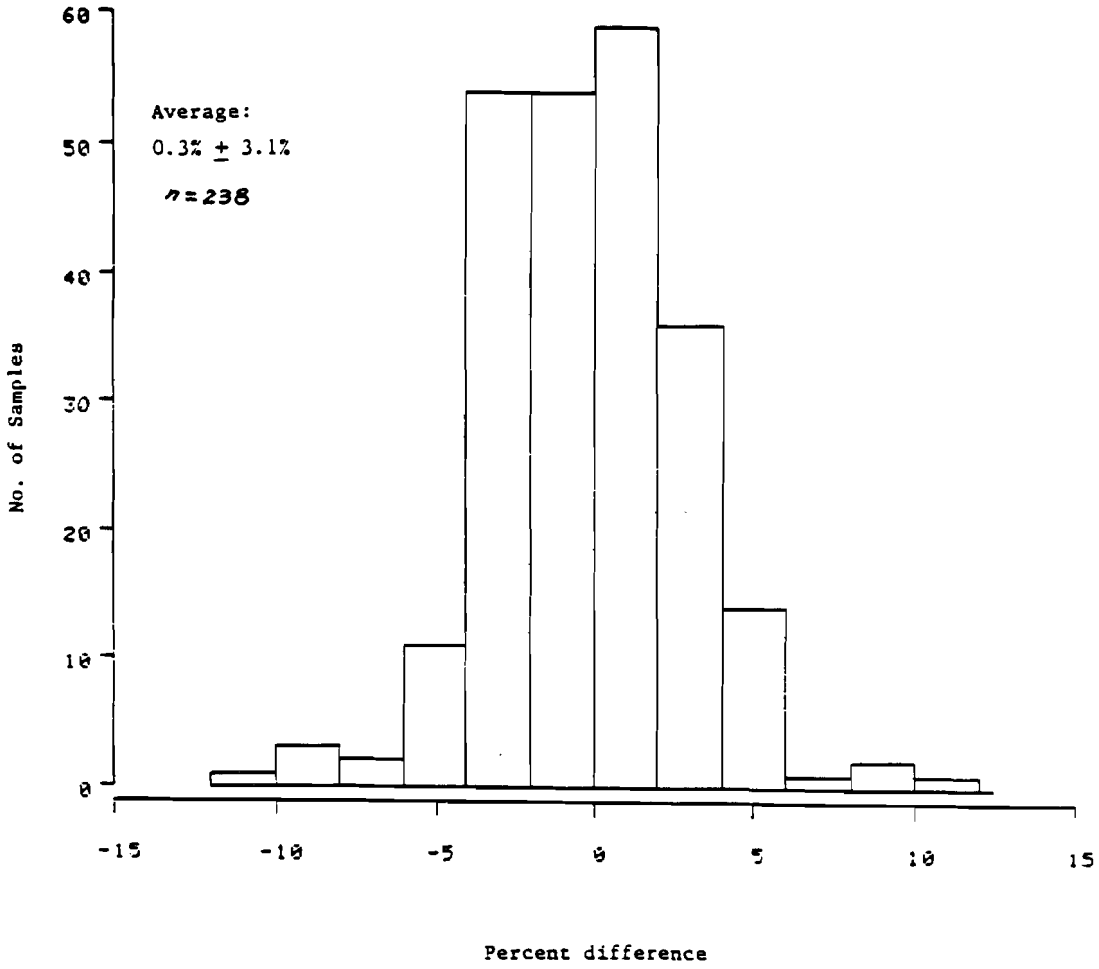

Figure 1. Histogram distribution of the percent difference between measured patient exit-dose and calculations.

a. Calculated

b. Measured

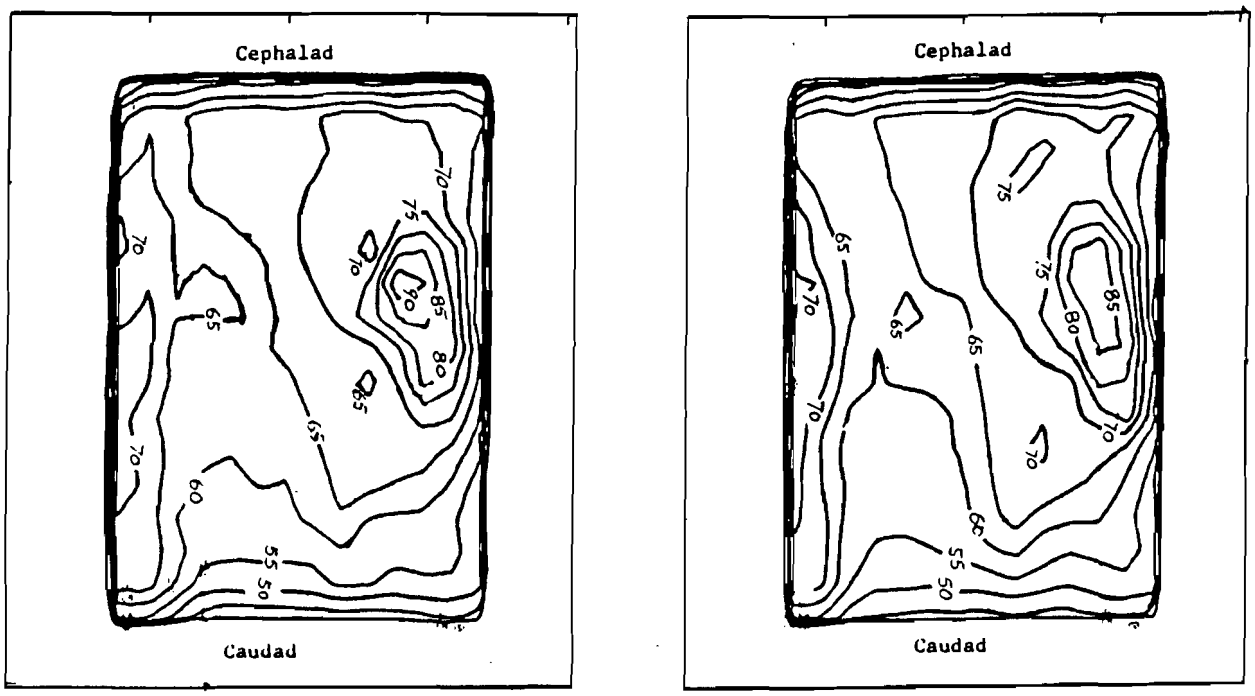

Figure 2. Comparison of patient-exit-dose distribution based on film dosimetry and delta-volume calculations.

C-4. Development of a Rapid Area-Dosimetry System

Personnel: J. W. Wong, Ph.D., Radiology
W. R. Binns, Ph.D., Physics
J. W. Epstein, Physics
S. K. Ge, Radiology
M. H. Israel, Ph.D., Physics
J. Klarmann, Ph.D., Physics
B. H. Raup, Physics
F. U. Rosenberger, BCL and Computer Systems Laboratory

Support: RR 01380
RR 01379
Mallinckrodt Institute of Radiology
Washington University

During the past few years, it has become apparent that methods of photon dose calculations capable of achieving the recommended goal of 3% accuracy will be available in the near future. For the calculations to be meaningful, it also becomes imperative that the measured water dosimetry data, resident in the treatment planning system, attain an accuracy of better than 3%. While the input data based on the customary "point" ionization chamber measurements have precision of the order of 0.5%, the excessive measuring time permits only a few standard data sets to be acquired. All 3-dimensional dosimetry data are generated from the standard set by interpolation and extrapolation functions and are subjected to possible errors in the empirical fitting model. One example is along the diagonal axis of the beam. As an alternative, we have developed a novel detector system where a large quantity of dosimetric data can be measured within a very short time, in the order of seconds. The approach is attractive since computer storage is becoming more and more affordable.

The project is a collaborative effort for the Division of Radiation Oncology and the Cosmic Ray Group in the Department of Physics at Washington University. The dosimetry system is based on a sheet of plastic scintillator, a digital camera, and a small computer system. The schematic of the external photon or electron beam dosimetry system is shown in Figure 1. At present, a prototype system has been built based on a polystyrene scintillator sheet to be viewed by a GE-TN2505 charge-injection device (CID) digital camera interfaced to an IBM-XT personal computer via a Poynting Products Inc. image buffer. Initial measurements have been made.

Figures 2a and 2b, and 3a and 3b show the iso-intensity distributions for the 12-MeV and 20-MeV electron beam along with a comparison of the central-axis depth-intensity profiles to the depth-dose profiles deduced from ionization measurements. The 2-dimensional scintillation data consisted of about 90,000 points acquired in two 5-sec integration times with the GE camera operating in the charge-inhibit mode. The artifact near the center of the iso-intensity contours were caused by a dust speck on the camera detector. All camera operations were controlled by the Poynting software package. For more efficient data analysis, the

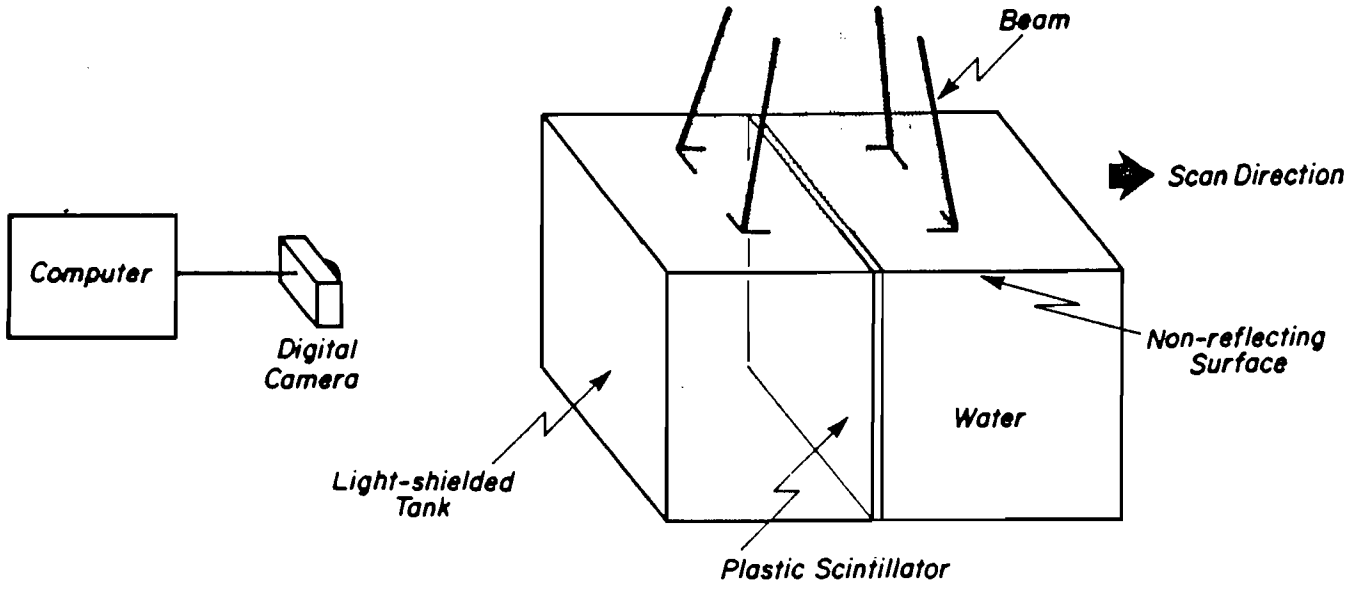

EXTERNAL PHOTON AND ELECTRON BEAMS DOSIMETRY SYSTEM

Figure 1. Schematic of an external beam dosimetry system based on a plastic scintillator sheet.

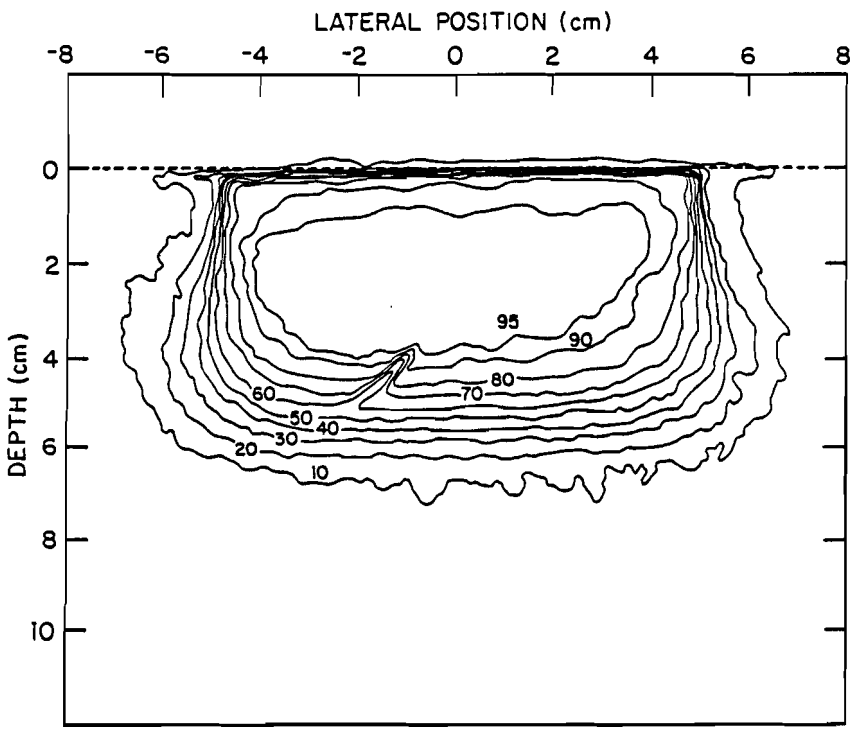

Figure 2a. Iso-intensity contour for the 12 MeV electron beam using the new system with green scintillator. Dose rate 500 rad/min.

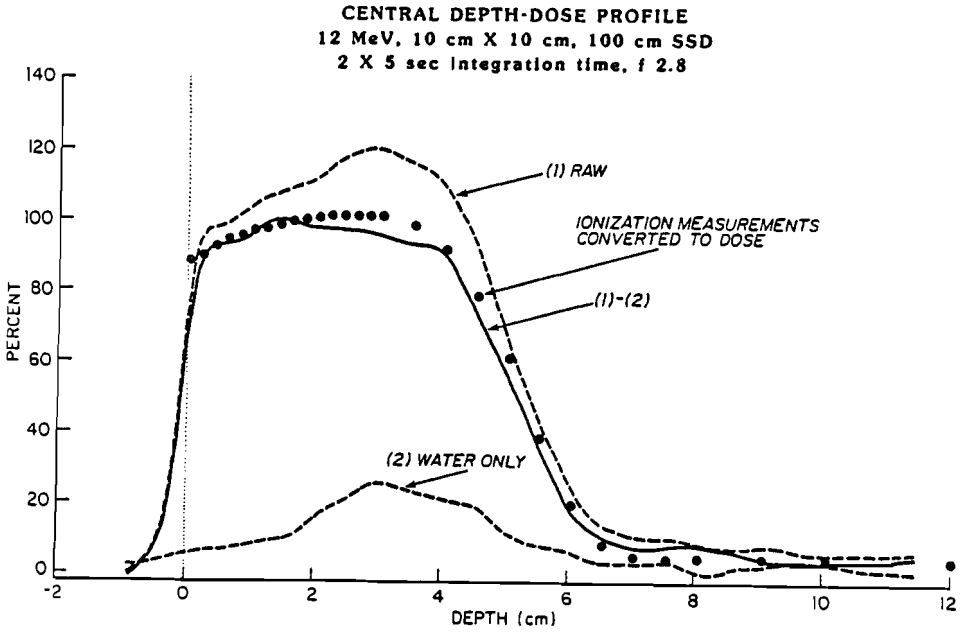

Figure 2b. 12 MeV electron beam percent maximum depth profile for scintillation light output and ionization (dose) measurements. Significant scintillation was due to the tap water.

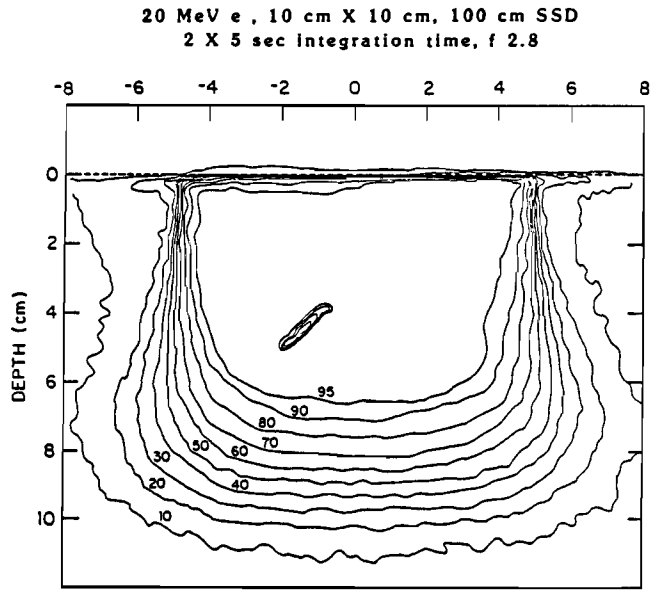

Figure 3a. Iso-intensity contour for the 20 MeV electron beam using the new system with green scintillator. Dose rate 500 rad/min.

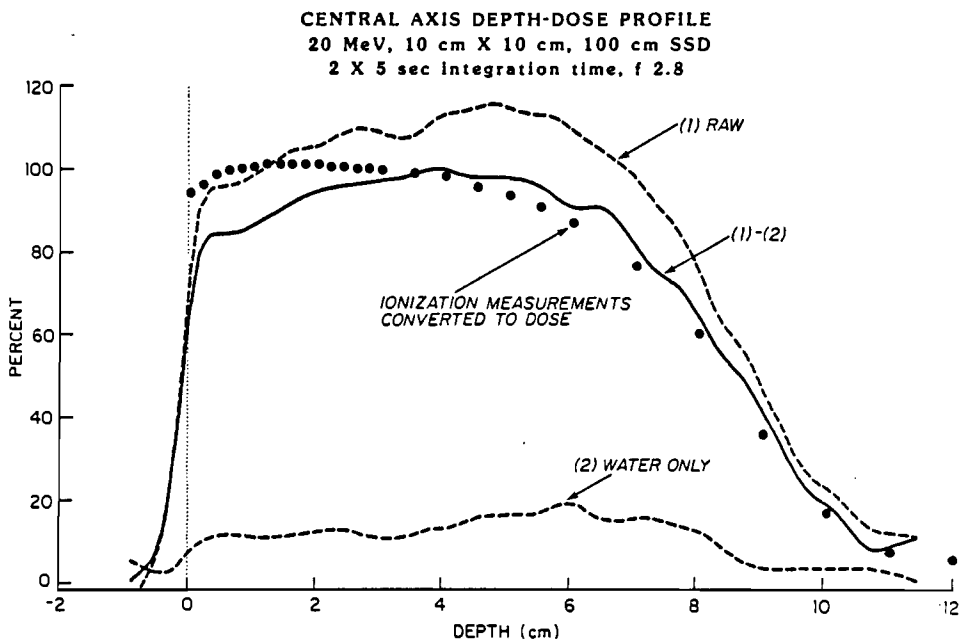

Figure 3b. 20 MeV percent maximum depth profile for scintillation light output and ionization (dose) measurements.

90,000 data points were reduced to about 7500 data points with an area resolution of approximately 2mm-squared.

From our studies, we have learned that: (1) tap water could scintillate because of the presence of impurities and this light output must be subtracted as background; (2) vignetting effect at very large camera lens aperture causes a central enhancement artifact that can be eliminated with a smaller aperture at the expense of longer data collection time; (3) there is non-uniformity in the response of individual pixels of the 243 x 388 CID array which can be reduced by mathematical smoothing at the expense of spatial resolution; and (4) dark current must be reduced by cooling in order to achieve favorable signal-to-noise ratio (S/N) (e.g. S/N improves by about a factor of 4 with cooling from 20°C to 0°C.)

The results shown in Figures 2 and 3 are most encouraging. We believe that the scintillation data at present is within 5% agreement to ionization dosimetry with the majority of the discrepancies due to effects such as local non-uniformity, optical reflections and refractions, etc. These effects will be studied and corrected in the coming year.

After refinement, we intend to characterize the properties of the area-dosimetry system in terms of its resolution, linearity and energy response to various beam modalities, uniformity and susceptibility to radiation damage. If successful, this area-dosimetry system will greatly enhance practical radiation dosimetry studies, particularly for difficult problems such as build-up effects. We are also hopeful that the approach can be extended to brachytherapy dosimetry and quantitative treatment verification.

D. Quantitative Imaging: Positron-Emission Tomography

Stimulated by the clinical impact of the EMI transmission tomographic scanner in 1973, experimental studies were initiated in collaboration with the Division of Radiation Sciences to evaluate positron coincidence-detection as a method for emission reconstruction tomography. This collaborative activity resulted in a prototype scanner called PETT (Positron-Emission Transaxial Tomograph). Extensive studies in patients and animals were conducted with the PETT III scanner in collaboration with the divisions of Neurology and Cardiology. A subsequent scanner, PETT IV, utilized concepts developed with its predecessor but incorporated a novel technique for the simultaneous collection of four tomographic slices from a single set of detectors. Until its decommissioning two years ago, PETT IV was located in the Coronary Care Unit for use in the SCOR project for the quantification of regions of myocardial ischemia and infarction (D-1, D-2). Subsequent scanners have been developed that permit more rapid data collection and improved spatial resolution. One of these, PETT V, was used in experimental studies in dogs. PETT VI became operational during the summer of 1980 and employs fast detectors and an entirely circular motion for rapid data acquisition. Further experimental and clinical studies with this system occurred over this past year (D-1, D-3, D-4). Developments in crystal technology and high-speed electronics now permit the propagation time of each of the two photons created in an annihilation to be measured. Theoretical and experimental studies of tomography systems that utilize this new information continued, and the software and hardware needed to realize the predicted benefits were developed. Super PETT I, the first operational system utilizing time-of-flight information, has been in routine use in the Cardiac Care Unit for over a year now (D-2). This device replaced PETT IV. A second generation time-of-flight tomograph, Super PETT II (Head and Body), has been in the final stages of testing during the past year and will soon be moved to the Division of Radiation Sciences to replace PETT VI (D-4). At this time PETT VI will move to Clinical Sciences and be devoted entirely to animal studies (D-1). Studies to improve data acquisition and reconstruction algorithms for Super PETT I and Super PETT II continued during the year (D-5 to D-10) and novel processing architectures were developed (D-12). A new approach for estimating parameters in dynamic studies using list-mode data (D-11) was completed and will now be installed in the clinical setting for routine use. Collaborating institutions are being configured with satellite processing systems to allow research at their facilities to utilize PETT data acquired with the PETT instruments at Washington University (D-13).

D-1. PETT Experimental Studies

Personnel: S. R. Bergmann, M.D., Ph.D., Medicine
J. Markham, BCL
D. W. Myears, M.D., Medicine
B. E. Sobel, M.D., Medicine
M. J. Welch, Ph.D., Radiology

Support: RR 01380
HL 13851
HL 17646

The overall goal of this project is to implement and evaluate procedures required to translate into intact animals the results obtained with selected positron-emitting tracers used to characterize myocardial metabolism and perfusion in isolated hearts and anesthetized, open-chest dog studies performed with Isolated Probe Data Acquisition System (A-6). Utilizing positron-emission tomography with PETT VI, the distribution of tracer and the time course of its uptake and clearance from myocardium can be quantified. Such studies are intimately related to the clinical studies using positron-emitting tomography (D-2).

We have previously demonstrated that PET can be used to estimate the salutary response to coronary thrombolysis. These studies have continued during the current project year. Concomitant use of pharmacologic agents may be required for maximal salvage of ischemic myocardium by reperfusion. Accordingly, in dogs with induced thrombotic coronary occlusion, the effects of intravenous diltiazem given 30 minutes before administration of streptokinase in myocardial blood flow in myocardial salvage were evaluated with positron-emission tomography, and results correlated with direct measurements of myocardial infarction by assay of creatine kinase activity in myocardial homogenates and flow measured with radioactive microspheres. Infarct size averaged 27.9 $\pm$ 11.4% of the left ventricle in 10 control dogs in which coronary occlusion was maintained for 24 hours. In eight dogs given streptokinase alone, starting two hours after occlusion, infarct size averaged 15.7 $\pm$ 10% ($p < 0.05$ compared with control). In nine other dogs given 15 μg/kg/min of diltiazem, beginning 30 minutes before streptokinase, infarct size averaged 9.4 $\pm$ 6.7% ($p < 0.05$ compared with reperfusion). At the dose administered, diltiazem did not alter blood flow, heart rate, or mean arterial pressure after coronary occlusion or thrombolysis.

The region at risk determined from perfusion images obtained with PET and $H_2{}^{15}O$ was similar in the three groups (30.6 $\pm$ 7.3% of the left ventricle in control dogs, 31.8 $\pm$ 4.5% in dogs with reperfusion alone, and 30.5 $\pm$ 11.6% in dogs with reperfusion plus diltiazem). Infarct size quantified in terms of myocardium exhibiting less than 50% of peak ^{11}C-palmitate uptake 24 hours after occlusion, and expressed as a percentage of the region at risk averaged 89.6 $\pm$ 11.4% in control dogs was reduced to 45.1 $\pm$ 29.8% in dogs with reperfusion alone, and was reduced further to 22.3 $\pm$ 16.4% in dogs given diltiazem and reperfusion. Thus, concomitant treatment with diltiazem markedly enhances salvage of reperfused myocardium after coronary thrombolysis, an observation that was detectable noninvasively with PET, and which will serve as the basis for a clinical trial of this concomitant pharmacologic therapy.

In additional studies, we studied ischemia followed by reperfusion on the metabolic and flow response to prolonged reperfusion. PET with $H_2{}^{15}O$ and ^{11}C-palmitate were used to sequentially assess myocardial perfusion and metabolism before and after angiographically documented lysis of occlusive thrombi (occlusion interval of 2.5 hours) and sequentially for four weeks. Four control dogs were studied in which permanent coronary occlusion was induced by placement of a copper coil into the left anterior descending coronary artery. Six dogs were studied in which reperfusion was induced two hours after occlusion with the use of either intracoronary streptokinase or intravenous tissue-type plasminogen activator. Sequential angiography documented patency of the coronary artery for four weeks in treated dogs. Occlusion of the left anterior descending coronary artery resulted in an anterior perfusion defect 90 minutes after coronary thrombosis. Tomograms obtained one hour after the onset of reperfusion documented substantial restoration of perfusion to the previously ischemic myocardium. Despite maintained patency of the artery, nutritional perfusion was markedly reduced 24 hours later to approximately 40% of normal flow. This decrease was transitory however, and one week after reperfusion, flow in the anterior region had increased substantially from the nadir seen at 24 hours after recanalization. Perfusion in this region remained relatively unchanged between one and four weeks after recanalization. Blood flow quantified with PET correlated closely with values obtained conventionally with radio-labeled microspheres.

Restoration of perfusion after thrombolysis was accompanied by increases in the accumulation of ^{11}C-palmitate in animals subjected to thrombolysis. However, 24 hours after recanalization, accumulation of ^{11}C-palmitate was depressed in association with a diminution of perfusion. Some recovery of accumulation of ^{11}C-palmitate was evident during the interval from 24 hours to one week after reperfusion. However, the time course and extent of metabolic recovery varied considerably among the six dogs given thrombolytic agents. In some, accumulation of ^{11}C-palmitate improved in parallel with the improvement of perfusion. In others, accumulation of ^{11}C-palmitate remained depressed one, two, and four weeks after recanalization.

In dogs with persistent occlusion, there was marked depression of myocardial blood flow and accumulation of ^{11}C-palmitate in the anterior region, initially, and 24 hours later. However, despite maintained thrombotic occlusion of the LAD coronary artery for four weeks, myocardial blood flow in the initially ischemic region increased with time. Late increases of perfusion, presumably attributable to collateral flow, were not accompanied by increases in fatty acid uptake at four weeks. Of interest, flow during ischemia was a poor predictor of regional recovery of myocardial blood flow or recovery of accumulation of ^{11}C-palmitate four weeks after recanalization ($r = 0.30$ and 0.45 respectively). Persistence of uptake of palmitate during ischemia was a weak but better predictor of accumulation of ^{11}C-palmitate at four weeks ($r = 0.64$). Additionally, the extent to which flow was restored after thrombolysis was not a powerful descriptor of the extent to which flow would be maintained four weeks after recanalization ($r = 0.49$). Initial accumulation of labeled fatty acid after recanalization ranged from 44 to 95% of normal. This uptake one hour after recanalization was a powerful descriptor of palmitate uptake four weeks after recanalization ($r = 0.86$, $p < 0.03$), and indicates a tomographic assessment of regional myocardium metabolism one hour after recanalization permits prediction of the amount of myocardium that can be

anticipated to exhibit metabolic criteria of salvage one month later. Thus, it suggests that tomographic assessment early after recanalization can delineate difference among hearts subjected to coronary thrombolysis that presage long-term benefit and may justify or mandate against other common aggressive interventions such as coronary bypass grafting or coronary angioplasty.

The studies completed during the past year have demonstrated the utility of PET, especially in evaluating the efficacy of interventions to improve myocardial metabolism and perfusion after coronary thrombolysis. The techniques developed in the project are currently being implemented in clinical studies designed to evaluate the efficacy of such interventions in patients.

During the coming year, we plan to continue our evaluation of the effects of coronary thrombolysis on the restoration of myocardial perfusion and metabolism with PET to better characterize response of this promising intervention. In particular, we are interested in studying the effects of a residual coronary stenosis (seen in the majority of patients undergoing coronary thrombolysis) on the metabolic and flow responses to recanalization. In addition, we plan to evaluate and implement algorithms for correction of the effects of partial volume and count spillover to enable measurements of perfusion in absolute terms.

D-2. Super PETT I Cardiac Studies

Personnel: E. M. Geltman, M.D., Medicine
H. D. Ambos, Medicine
T. R. Baird, Medicine
D. E. Beecher, BCL
A. S. Jaffe, M.D., Medicine
J. Markham, BCL
B. E. Sobel, M.D., Medicine
M. M. Ter-Pogossian, Ph.D., Radiology
M. J. Welch, Ph.D., Radiology

Support: RR 01380
HL 13851
HL 17646

This project is designed to characterize regional myocardial metabolism and perfusion quantitatively with positron-emission tomography (PET) in normal subjects and patients with coronary artery disease at rest and in response to stress induced with vasodilators or dynamic exercise. It is designed also to assess the efficacy of reperfusion induced by thrombolysis, balloon angioplasty, surgical revascularization or combinations of all three reflected by myocardial perfusion and metabolic activity.

Previous studies outlined in earlier progress reports had demonstrated the feasibility of employing dynamic high-resolution positron

imaging for the delineation of regional myocardial metabolism and perfusion. Studies during the past year have focused on several questions. A randomized, double-blind placebo-controlled trial was completed to determine whether nifedipine can improve myocardial metabolism in jeopardized myocardial zones in patients with evolving myocardial infarction. The viability of ischemic zones was assessed by positron emission tomography with intravenous carbon-11 (^{11}C) labeled palmitate. Tomographic studies were performed at the time of CCU admission prior to administration of nifedipine or placebo. Therapy was continued for 7 days. On the 10th day, tomographic studies were repeated. The estimated extent of impaired ^{11}C-palmitate accumulation declined from 58 $\pm$ 8 (SD) PET-g-Eg to 49 $\pm$ 7 in treated patients ($p < .05$) but did not change in controls (44 $\pm$ 9 initially and 44 $\pm$ 12 after 10 days). Enzymatic estimates of infarct size were comparable between groups and ejection fractions were comparable before and after therapy. Thus, despite the lack of gross reduction of infarct size, nifedipine initiated early after the onset of infarction apparently exerts salutary effects on regional myocardial metabolism in the peri-infarct zone compatible with decreased after-load, reduced coronary spasm, direct myocardial protection or combinations of the three. Furthermore, this investigation demonstrated the potential importance of PET for the assessment of interventions designed to modify the extent of myocardial necrosis in patients with evolving myocardial infarction.

Studies initiated earlier in this project, which were designed to develop, validate and implement a technique for the assessment of regional myocardial perfusion in patients with PET, have been continued during this past year. Twelve normal subjects and 34 patients with coronary artery disease were studied after the rapid infusion of 35 to 130 mCi of $H_2{}^{15}O$ and the inhalation of $C^{15}O$. A total of 35 studies were performed before and after pharmacologic vasodilator stress with dipyridamole (0.56 mg/kg, i.v. over 4 min). A variety of doses of $H_2{}^{15}O$ and a variety of infusion protocols were employed to determine the optimal procedure for assessment of myocardial perfusion. Data were reconstructed in a variety of formats with analysis of data in multiple 5-sec, 10-sec, or 120-sec frames. Optimal assessment of myocardial perfusion was achieved with bolus injection of $H_2{}^{15}O$ (0.4 to 0.5 mCi/kg) through a central intravenous catheter and reconstruction of the data as 120-sec reconstructions beginning with the arrival of radioactivity in the left ventricular cavity. These reconstructions were utilized for construction of regions of interest for further dynamic analysis. Dynamic analysis was performed by calculating the regional radioactivity sequentially in multiple 10-sec reconstructions beginning with the arrival of radioactivity in the left ventricle. Dynamic rates of accumulation of tracer were homogeneous in normal subjects at rest and after dipyridamole. In contrast, regions of depressed apparent content of $H_2{}^{15}O$ were present at rest or with stress in over 80% of patients with CAD. In addition, the rate of accumulation of $H_2{}^{15}O$ in tissue was depressed in zones subtended by partially or completely obstructed coronary arteries. The disparity between normal and abnormal zones was augmented after dipyridamole.

Studies in progress are designed to further characterize the dynamics of the accumulation of $H_2{}^{15}O$ in normal subjects and in patients with coronary artery disease. Further modeling of the regional dynamic time-activity curves is planned with applications of 1- and 2-compartment Ketty-Schmidt models. Data will be compared to results of quantitative coronary angiography which is currently being developed and validated.

Further clinical studies are in progress designed to characterize the dynamics of labeled fatty acid deposition and clearance from myocardium of normal subjects, patients with chronic stable ischemic heart disease and patients with acute myocardial infarction with and without reperfusion induced by coronary thrombolysis with rt-PA. Initial results indicate that myocardial accumulation and clearance of ^{11}C-palmitate appears to be homogeneous in normal subjects but clearance appears delayed in zones of recent ischemia. Zones of remote infarction demonstrate depressed apparent accumulation of tracer, but clearance rates appear to be relatively similar to those observed in normal zones.

The proposed research should ultimately permit noninvasive delineation of altered regional myocardial metabolism and perfusion in patients with functionally significant coronary artery disease. During the past year we have demonstrated the efficacy of nifedipine as a treatment of acute myocardial infarction, and thereby have established the utility of positron-emission tomography for the assessment of interventions designed to salvage ischemic myocardium. In addition, we have established a technique for the assessment of myocardial perfusion at rest and with vasodilator stress, employing the freely diffusible tracer $H_2{}^{15}O$ which permits the noninvasive assessment of myocardial perfusion independent of abnormalities of myocardial metabolism.

D-3. Study of the Use of Maximum-Likelihood Image Reconstruction for Super PETT I Dog Heart Studies

Personnel: J. Markham, BCL
S. R. Bergmann, M.D., Ph.D., Medicine
S. K. Liu, BCL
S. M. Moore, BCL
D. L. Snyder, BCL

Support: RR 01380
HL 17646

This project was designed to explore the feasibility of using the EM algorithm for maximum-likelihood reconstruction of cardiac images obtained using Super PETT I (D-2, D-10). Images of a dog heart were reconstructed from the same scan data using the EM algorithm and the confidence-weighting (CW) algorithm (presently used for Super PETT I image reconstruction) to determine if the EM algorithm produces superior (less noisy) images.

In dynamic studies of myocardial perfusion and metabolism, a total scan time of a few minutes is subdivided into shorter intervals and multiple images are reconstructed for the shorter intervals so that changes in the distribution of the radionuclide can be measured (D-2). Because of the small number of annihilation events detected during the short intervals and the loss of data due to gating with selected portions of the heart cycle, the dynamic images are extremely noisy. The EM algorithm for maximum-likelihood reconstruction of images should produce images which are less noisy (PR 20, D-8).

An image of a dog heart, obtained following injection of gallium labeled (^{68}Ga) microspheres, was reconstructed with the EM algorithm. The microsphere image was selected for analysis because it was moderately noisy with the left ventricle readily discernable. Gating of the data according to the heart cycle was used in the reconstruction process to reduce the effects of heart motion.

The first step was to modify the existing Super PETT programs to retain projection data for all 96 angles instead of using the reduced angle data described in D-7. A coordinate transformation was then performed, using linear interpolation in two directions, to generate data in the format required by the existing EM programs. Forty iterations of the EM algorithm without the addition of a sieve function (D-5) were performed to produce an image without the artifacts seen when more iterations are used.

The CW image and the EM images were then compared visually to detect obvious differences. Although the EM image appeared to have better resolution, no quantitation of resolution could be obtained because of the unknown source (the dog heart). The CW image was less noisy, probably due to the smoothing effects introduced by the angle reduction and the filter used for reconstruction. We concluded that the improvements in the image using the EM algorithm were not sufficient to justify immediate implementation of the EM algorithm in view of the uncertainties concerning the sieve functions to be used and the excessive execution time required.

D-4. In Vivo Measurements of Regional Blood Flow and Metabolism in Brain

Personnel: M. E. Raichle, M.D., Neurology and Radiology
D. C. Ficke, B.S., Radiology
P. T. Fox, M.D., Neurology and Radiology
M. H. Gado, M.D., Radiology
R. L. Grubb, Jr., M.D., Neurological Surgery
P. Herscovitch, M.D., Neurology and Radiology
M. R. Kilbourn, Ph.D., Radiology
K. B. Larson, BCL
J. Markham, BCL
M. A. Mintun, M.D., Radiology
J. S. Perlmutter, M.D., Neurology
W. J. Powers, M.D., Neurology and Radiology
D. L. Snyder, BCL
M. M. Ter-Pogossian, Ph.D., Radiology
M. J. Welch, Ph.D., Radiology

Support: RR 01380
HL 13851
HL 25944
NS 06833
ECS 8215181
Washington University

Because of the previously noted (PR 21, D-3) deficiencies of compartmental models for estimating cerebral blood flow with PET using radioactive water as a tracer, we have been led to the formulation and testing of distributed-parameter models for this purpose. The distributed-parameter models we have investigated take into account longitudinal gradients of tracer concentration along the capillaries but assume that transverse gradients are zero. The resulting conservation conditions take the form of sets of partial differential equations in the concentrations, with axial distance and time as independent variables and with capillary and cellular permeabilities, surface areas, volumes, and thermodynamic activity coefficients as parameters.

Encouraged by close agreement between our model predictions and external count-rate data obtained in animal experiments (PR 21, D-3), we have begun to investigate the possibility of applying our model for measurement of cerebral blood flow in patients using positron-emission tomography (PET). For this purpose, we have conducted experiments in which oxygen-15-labeled water was injected intravenously in human subjects and the resulting radioactivity was monitored in brain using a PET scanner. Data were acquired regionally during sequential ten- and twenty-second scan intervals. Arterial blood samples withdrawn at a peripheral site during the scans were radioassayed in a laboratory scintillation well counter, and from these, the cerebral-blood inflow concentration history was inferred by appropriate time shifts. The influx history was then convolved with the unit-impulse residue-response function of our two-barrier distributed-parameter model (PR 21, D-3). The resulting dispersed simulation is used to form an objective function as the basis for parameter estimation. We have preliminary results for one set of patient data that appear plausible; these have reinforced our expectation of success with the remaining data sets that await analysis.

A program was implemented on the Radiation Sciences Perkin-Elmer 3242 computer system to compute blood flow, extraction fraction, and mean transit time from time-activity curves of radioactive tracers obtained using isolated scintillation-detection probes placed over the brain. This program utilizes the index methods, previously derived by investigators here, in which an exponential function is fit to the downslope of the count-rate data curve. Parameters of the fitted curve are then used in empirically derived equations to yield the physiological parameters of interest. Semilog plots of the count-rate data and the fitted curves are generated on a graphics terminal so that the user can detect obvious anomalies in the data.

The program has been used to analyze several cases of the probe data collected by the LINC (Laboratory Instrument Computer) during the past 15 years. Data from 461 LINC tapes were transferred to ten 9-track magnetic tapes to allow analysis of the data on the present computer systems.

D-5. The Use of Sieves to Stabilize Images Produced with the EM Algorithm for Emission Tomography

Personnel: D. L. Snyder, BCL
M. I. Miller, BCL
S. M. Moore, BCL

Support: RR 01380

We have shown (PR 21, D-7) that Grenander's sieves can be used with the expectation-maximization (EM) algorithm to reduce the noise artifact seen with increasing iterations in PET reconstructions. We have been exploring this idea for convolution kernel-sieves in which the kernel is a circularly symmetric Gaussian function. This choice is not fundamental but has the advantage of requiring no substantial changes in the implementation of the EM algorithm without sieves and requiring no substantial additional computation. The Gaussian kernel is defined by a single parameter, its full width at half maximum. A rationale for the choice of a value for this parameter is unclear. It should be small so that resolution is not sacrificed, but it must be large enough to suppress the noise artifact. We have been studying the effects of this parameter on reconstructed images in a computer simulation of a PET system for the heart-liver phantom. Preliminary results indicate that the noise artifact can be suppressed at the expense of decreased resolution. We have presented evidence [1] that the use of Grenander's method of sieves reduces these undesirable artifacts. Work on this problem is continuing.

1. Miller, M. I., Snyder, D. L., and Moore, S. M., "An Evaluation of the Use of Sieves for Producing Estimates of Radioactivity Distributions with the EM Algorithm for PET," IEEE Transactions on Nuclear Science, vol. NS-33, no. 1, pp. 492-495, 1986.

D-6. Time-of-Flight Data Acquisition System Development for Super PETT I and Super PETT II

Personnel: D. E. Beecher, BCL
D. G. Ballinger, B.S., Radiology
D. C. Ficke, B.S., Radiology

Support: RR 01380
HL 13851

The data acquisition system for Super PETT I (PR 21, D-5) has remained essentially unchanged over the past year. A small problem with collection priority was identified and corrected in the initial testing phase.

A major effort was spent designing and implementing the 3-phase collection software required for Super PETT II (head and body). The three phases consisted of:

a) on-the-fly attenuation array (ignoring TOF information);
b) acquisition and storage of raw list-mode events;
c) acquisition and storage of preprocessed list-mode events.

The new design for support hardware for Super PETT II (PR 21, D-11) necessitated some major changes in the slice processor interface as well as the data-acquisition software to support that new interface. The new interface uses an internal dual-buffer to allow collection of events from the gantry while the other buffer is being read to memory and processed and/or stored to disk for post-processing. All three phases were initially designed and implemented for the head-system. These routines have been successfully used over the past year. The software modules were then modified slightly to operate with the body system and are currently in the final testing stages.

D-7. A Reduced-Angle Reconstruction Algorithm for Super PETT I

Personnel: D. G. Politte, M.S., Radiology
D. E. Beecher, BCL
D. C. Ficke, B.S., Radiology
G. R. Hoffman, B.A., Radiology

Support: RR 01380
HL 13851
HL 17646

Computer simulations have been performed in order to quantify the performance of the reduced-angle weighting algorithm relative to confidence weighting. The performance of the reduced-angle weighting algorithm depends both on the number of angles into which the data are organized and

on whether optimal or suboptimal weights are used. The motivation for use of suboptimal weights is that they can be applied more efficiently.

The results of simulations of a 30-cm-diameter disk with a uniform intensity of radioactivity such that one million counts occur on the average have been reported [1] and are summarized below:

- The images reconstructed with optimal and suboptimal weighting functions are only negligibly different when the number of reduced angles is greater than or equal to 16.

- The signal-to-noise ratio loss due to using 16 reduced angles, instead of the original 96 angles, is approximately one decibel everywhere within the disk.

- The algorithm yields unbiased estimates of the desired image.

- The reconstructed resolution is the same as with confidence weighting.

The image-reconstruction software in routine use for Super PETT I uses 16 reduced angles with suboptimal weighting.

The simulation software also can be used to determine the performance of the reduced-angle weighting algorithm for other tomograph designs and geometries, such as Super PETT II.

1. Politte, D. G., Hoffman, G. R., Beecher, D. E., Ficke, D. C., Holmes, T. J., and Ter-Pogossian, M. M., "Image-Reconstruction of Data from Super PETT I: A First-Generation Time-of-Flight Positron-Emission Tomograph," IEEE Transactions on Nuclear Science, vol. NS-33, no. 1, pp. 428-434, February 1986.

D-8. Design Studies of Computational Alternatives for TOF-Based PET Reconstructions

Personnel: S. M. Moore, BCL
S. K. Liu, BCL

Support: RR 01380

Previous studies (PR 21, D-8) provided estimates of the time needed to compute the maximum-likelihood (ML) estimate of a PET image using the EM algorithm (D-10). Those studies were carried out under the assumption that array processors or custom hardware would be used to perform the computations. New studies performed in the last year reaffirmed our estimate of producing ML estimates of seven images in five minutes using custom hardware.

The computation times for three possible implementations of the EM algorithm were parameterized for a system consisting of a Microvax II and a Mercury ZIP 3232+ Array Processor (F-6). Using timing estimates provided by the manufacturer before delivery of the system, we estimated the time needed to perform the EM algorithm as a function of the number of view angles, the size of the reconstructed image array (X, Y), the size of measurement data array (distance, TOF), the size of the filter kernel, and the density of the measurement data. The three implementations differed in the manner in which the Gaussian filter (corresponding to the measurement error) was applied to the data. One method was to perform all filtering steps in the frequency domain using FFTs. The other two methods involved performing a coordinate rotation to perform the convolutions in the original measurement space (d, T) rather than in the image-viewing space (X, Y) (D-9).

As expected, these estimates showed that an array processor implementation would not be suitable for a clinical setting. However, use of an array processor is appropriate while evaluating the EM algorithm. Below is our estimate of the time needed to perform one iteration of the EM algorithm using the ZIP 3232+ array processor for one set of parameters.

Number of angles:	96
Size of view space:	256 x 256
Pixel size (view space):	.25 cm
Measurement error (FWHM):	6 cm along TOF axis, 1 cm transverse to TOF axis
Nonzero pixels in measurement data:	5%

Filtering Method	Estimated Time/Iteration
FFT	18 min.
Convolution in D,T space (256, 40)	2.3 min.
Convolution in D,T space (256, 256)	8 min.

Future work in this area will include implementation of these algorithms on the ZIP array processor to determine the accuracy of our estimates and the effects of these implementations on estimates of the image. Current implementations of the algorithm using coordinate rotation and convolution in the measurement space take 23 and 36 minutes per iteration on a MASSCOMP computer for 256 x 40 and 256 x 256 systems, respectively.

D-9. Investigation of Methods for Speeding Maximum-Likelihood Image Reconstruction with the EM Algorithm

Personnel: D. L. Snyder, BCL
H. A. Klotz, M.S., Electrical Engineering
S. K. Liu, BCL
F. U. Rosenberger, BCL and Computer Systems Laboratory

Support: RR 01380
RR 01379

The computational demands of the expectation-maximization (EM) algorithm are so great that images cannot be produced in clinically useful times with straightforward processing on a serial machine. For this reason, we have been exploring a variety of ways for speeding up the algorithm. These include: processing data in rotated coordinates (D-8); using a reduced number of angular views (PR 21, D-6); modifying each step of the algorithm using a linear search procedure; and using special arithmetic to carry out the computations.

Rotated coordinates: Our past studies of the EM algorithm have been performed in rectangular coordinates. There are two speed up advantages in implementing the processing in a coordinate system oriented so that one axis is aligned with the time-of-flight direction. One is that the pixels along the time-of-flight axis can be made larger because of the relatively large errors in the time-of-flight data; this results in fewer pixels to process. The other advantage is that the Gaussian kernel of the two-dimensional convolutions to be performed in the EM algorithm is separable in the rotated coordinate system, which means that two one-dimensional convolutions can be used in place of each two-dimensional convolution. Since many two-dimensional convolutions are required, this can result in significant time saving.

Reduced angles: Reducing the number of angles at which data are processed directly reduces the computation time required. The effect on image quality of reducing the number of angles has been studied (PR 21, D-6) for the confidence-weighted algorithm but not yet for the EM algorithm.

Linear line search: The k-th step of the EM algorithm takes activity estimate k and produces activity estimate k+1. The algorithm is such that the likelihood for estimate k+1 is greater than the likelihood for estimate k. One approach for speeding the algorithm is to modify estimate k+1 in such a way that the likelihood is increased more. L. Kaufman of Bell Laboratories, Murray Hill, NJ has suggested a modification in the form of a linear combination of estimate k and estimate k+1, with the use of a golden-section search to identify the linear combination yielding the greatest increase in likelihood.

Arithmetic: An implementation of the EM algorithm in residue arithmetic has been simulated and the results show little degradation in the quality of the resulting images compared to an implementation in floating point arithmetic. A parallel, pipelined

architecture of a special purpose processor based on the use of residue arithmetic appears to offer very high speed so that images can be produced in clinically useful times.

These approaches to speeding up the EM algorithm are continuing to be studied.

D-10. EM Algorithm Studies

Personnel: D. L. Snyder, BCL
J. Markham, BCL
M. I. Miller, BCL
L. J. Thomas, Jr., BCL

Support: RR 01380

We have observed two artifacts when the expectation-maximization (EM) algorithm is used to compute maximum-likelihood estimates of radioactivity distributions for PET. One is in the form of high peaks and low valleys seemingly randomly distributed throughout the images; we call this a noise artifact. The other artifact is in the form of a systematic, nonrandom, Gibbs-like overshoot at edges in the images; we call this an edge-overshoot artifact. Others who have used the EM algorithm for PET reconstructions have also observed both types of artifact; these concerns have been repeatedly expressed at national conferences, such as the IEEE Nuclear Science Symposium and the Society of Nuclear Medicine meeting. We continue to try to identify the causes of these artifacts.

Our conclusion is that the noise artifact is fundamental to the maximum-likelihood method of image reconstruction and not to the use of the EM algorithm, which is but one numerical technique for computing maximum-likelihood estimates. We have also identified one possible approach for removing the noise artifact through the use of Grenander's method of sieves (D-5). Our work to date on this problem has been published [1].

The edge-overshoot artifact can be a substantial distortion. Our first conjecture when this artifact was observed was that it was not fundamental but, rather, wes the result of using too few iterations of the EM algorithm. This conjecture was based upon early simulations of one-dimensional mean-value data (i.e., no Poisson noise) in which the edge overshoot was observed to disappear after a very large number (80000) of iterations. In more recent computer simulations, however, we find that the overshoot does not disappear with continued iterations, even up to a million iterations, and that the peak overshoot can remain fixed at a value greater than the 9% associated with the Gibb's phenomenon of truncated Fourier series; our current feeling is that this excess overshoot may be due to the nonnegativity of the activity distribution and the fact that the EM algorithm produces estimates satisfying this nonnegativity constraint. The difference between the early and recent simulations lies in subtle issues associated with the numerical implementations. These differences can seem like minor ones, but they can have a major influence on the

manifestation of the artifact. For example, the decision of how far to retain the tail of the Gaussian convolution kernel before setting values to zero is important; cutting off at three standard deviations yields greatly different overshoot behavior from cutting off at six standard deviations. Our study of this artifact is continuing. Our tentative conclusion at this time is that it, like the noise artifact, is fundamental but not just to maximum-likelihood reconstruction. We now feel that it arises from the numerical instability necessarily encountered in the deconvolution problem of tomographic reconstruction regardless of the algorithm used.

1. Snyder, D. L. and Miller, M. I., "The Use of Sieves to Stabilize Images Produced with the EM Algorithm for Emission Tomography," IEEE Transactions on Nuclear Science, vol. NS-32, no. 5, pp. 3864-3872, October 1985.

D-11. Maximum-Likelihood Estimation of Parameters in Dynamic Tracer Studies

Personnel: J. M. Ollinger, BCL
D. L. Snyder, BCL

Support: RR 01380

The advent of positron-emission tomography (PET) made possible for the first time non-invasive, regionally localized parameter estimation in dynamic tracer studies. Despite the hope that complex models developed for single-probe experiments could be readily adapted for use with PET, investigators find that this is often not the case due to the poor time resolution of the data available to them. Data are currently collected by reconstructing a series of images over the time course of the study, spatially integrating each image over a region of interest to form a histogram of activity levels versus time, and then estimating parameters from this histogram. Since each image must span a time subinterval containing enough counts to yield an adequate image, the total number of subintervals in the histogram is limited. The primary goal of this research is to develop algorithms to compute estimates using the high temporal resolution inherent in the data collected by many PET scanners.

Snyder [1] proposed a method that solves this problem by using the EM algorithm of Dempster, Laird, and Rubin [2] to compute maximum likelihood parameter estimates from list-mode data, that is, from data which contain a record of each detected annihilation. The method can be decomposed into two algorithms, a weighting algorithm, which estimates a histogram of activity levels from list-mode data, and a parameter-estimation algorithm, which computes parameter estimates from this histogram. The research effort during the past year has been directed toward extending the weighting algorithm to both include the effects of attenuation, randoms, imperfect detector efficiency and nonuniform sampling density, and to permit the use of projection data collected at high frame rates. This extension is given in [3] and [4]. Furthermore, an evaluation of the weighting algorithm as described in [1] is given in [5].

The weighting algorithm computes an approximate minimum-mean-square error estimate of the histogram based on the Poisson statistics of the list-mode data. This estimate cannot be computed exactly, since it depends on the tracer concentration, which, being both unknown and non-stationary, must be approximated by a series of reconstructed images. The algorithm consists of first reconstructing images over each of a number of time intervals, identifying a region of interest in each image, computing probability arrays for each interval, weighting each detected event with the probability that it occurred in the region of interest, that it was detected by the scanner, and that it was not a random, and, finally, summing the weighted events into a histogram. This histogram is used along with an average survival probability in the region of interest by the parameter estimation algorithm. Since the number of subintervals in the histogram is limited only by the time resolution of the list-mode data, the output histogram can have the same number of subintervals as if it were collected with a single probe. These high-resolution histograms can be used with either the maximum-likelihood estimation algorithm discussed here or, with slight modifications to the algorithm, by any of the commonly used weighted least-squares algorithms. A variant of the algorithm can be used with projection data rather than list-mode data. Initial results of the evaluation of this algorithm indicate that the final parameter estimates are significantly more accurate than those obtained by the standard method.

Results of an evaluation of the weighting algorithm in [5] indicate that the summed square error of curve fits to histograms estimated by the weighting algorithm are as much as 50 times smaller than that for histograms estimated using the standard approach. Furthermore, estimates of physiological parameters computed from these histograms are significantly more accurate than those estimated from histogram computed using the standard method.

The evaluation of the iterative, parameter-estimation portion given in [4] shows that the maximum likelihood estimates are less biased and have a lower error variance than weighted least squares at all counting rates, but especially at low count rates. Furthermore, the EM algorithm was much less sensitive to poor starting values. It is, however, slower than weighted least squares by a factor of approximately 15.

In the next year we plan to implement and validate the extensions to the algorithm given in [4]. This validation will be done using simulations and real data.

1. Snyder, D. L. "Parameter Estimation for Dynamic Studies in Emission Tomography Systems Having List-Mode Data," IEEE Transactions on Nuclear Science, vol. NS-31, no. 2, pp. 925-932, April 1984.

2. Dempster, A. P., Laird, N. M., and Rubin, D. B., "Maximum Likelihood from Incomplete Data via the EM Algorithm," Journal of the Royal Statistical Society, vol. 39, pp. 1-38, 1977.

3. Ollinger, J. M. and Snyder, D. L., "A Preliminary Evaluation of the Use of the EM Algorithm for Estimating Parameters in Dynamic Tracer Studies," IEEE Transactions on Nuclear Science, vol. NS-32, no. 1, pp. 848-854, February 1985.

4. Ollinger, J. M., "Algorithms for Parameter Estimation in Dynamic Tracer Studies Using Positron-Emission Tomography," Doctoral Dissertation, Washington University, August 1986.

5. Ollinger, J. M., and Snyder, D. L., "An Evaluation of an Improved Method for Computing Histograms in Dynamic Tracer Studies Using Positron-Emission Tomography," IEEE Transactions on Nuclear Science, vol. NS-34, no. 1, pp. 435-438, February 1986.

D-12. Slice Processor Support for Super PETT II

Personnel: D. E. Beecher, BCL
D. G. Ballinger, B.S., Radiology
D. C. Ficke, B.S., Radiology
G. R. Hoffman, B.A., Radiology
D. G. Politte, M.S., Radiology

Support: RR 01380
HL 13851

During the past year, software development has been underway to utilize the slice processors in support of Super PETT II (PR 21, D-11).

The connectivity of the support systems for Super PETT II is shown in Figure 1. As can be seen, there is no way to interface directly with the slice computers. The user needs a communication scheme whereby he can communicate with each slice computer. This problem was solved with a software system which allows users to control task execution on each of the seven slice computers thru a task executing on the main computer.

Whenever a slice computer is started up, part of its startup procedure loads and starts a monitor task called SCMON (Slice Computer Monitor). There are identical SCMON tasks running on all seven slice computers. SCMON controls all other tasks running on a particular slice computer. SCMON constantly watches a non-buffered indexed file on the slice computer's dual-ported disc. This file is called MCTCOM.BLK (Slice Computer Monitor Communications Block). The main computer task (MCT), and the Slice Computer Monitors (SCMON) cannot share bi-directional communications blocks for two reasons: first, MCT runs on a user account under the multi-terminal monitor (MTM), while SCMON runs on the system account. There is no MTM running on the slice computers. MCT can write to a file on its own account but can only read from a file on the systems account. Likewise, SCMON can write to a file on the systems account, but can only read from private MTM account files. Second, the 80-Mbyte fixed disk on any given slice computer is actually set up as two virtual disks, one proprietary to the slice computer, allowing the main computer read-only privileges, and the other proprietary to the main computer, allowing the slice computer read-only privileges.

Each slice computer disk will also have a Slice Computer Subtask Communications Block (SCSCOM.BLK). This is a bi-directional communication

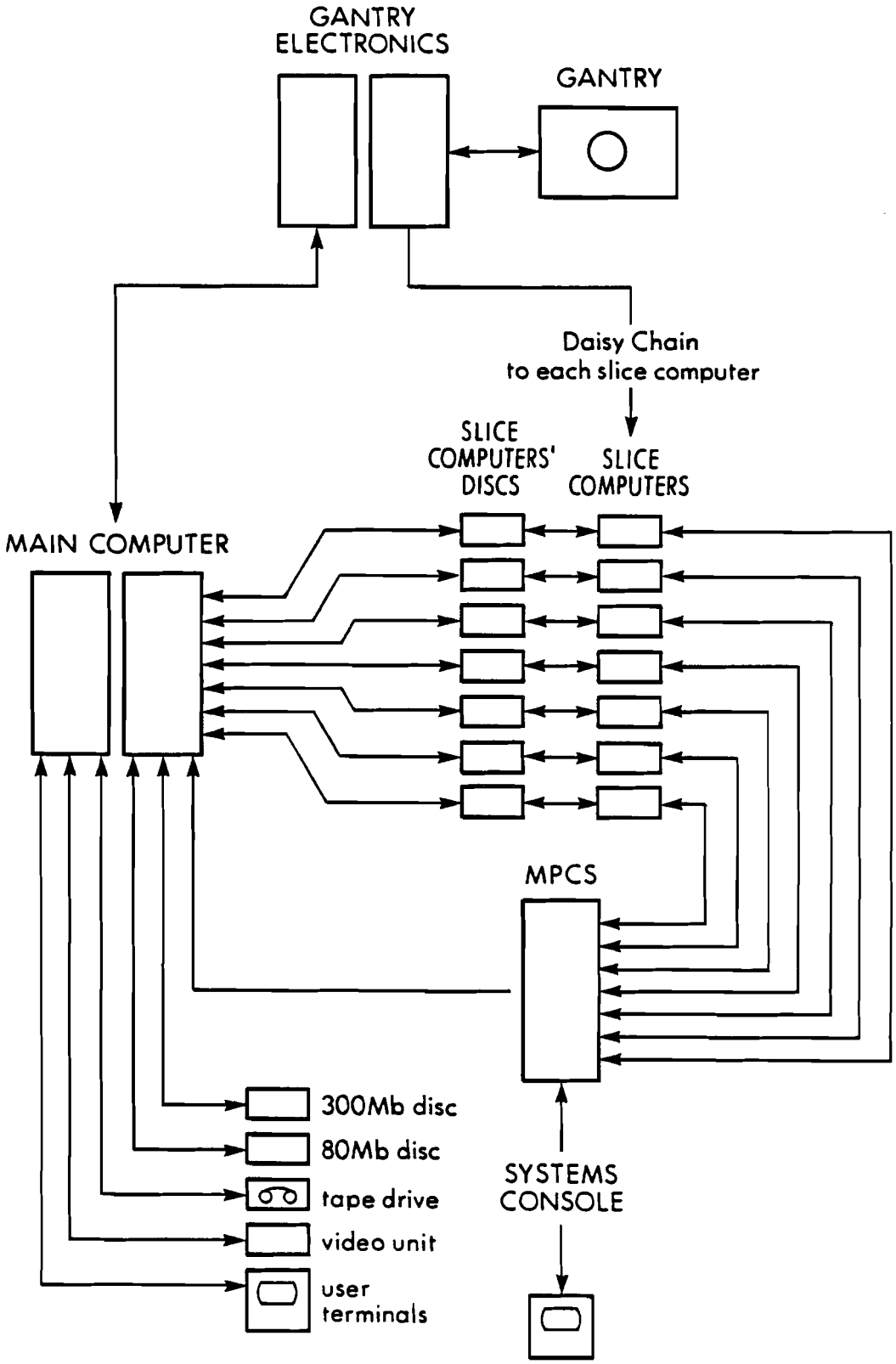

Figure 1. Gantry/Computer Connections and Computer/Computer Connections

block on the systems account with which SCMON and the subtasks communicate. There can be only one subtask running on a slice computer at any given time.

The task on the main computer that communicates with the slice computers is called MCT (Main Computer Task). MCT is essentially a middleman that passes data to the slice computers and informs the user of the status of the slice computers. It has a series of instructions that can be fed in from a special file or from the user's terminal. This scheme has been in routine use for several months now with no major changes.

D-13. Satellite PETT Systems

Personnel: D. E. Beecher, BCL
P. T. Fox, M.D., Neurology and Radiology
M. E. Raichle, M.D., Neurology and Radiology

Support: RR 01380
HL 13851

The methods for acquiring cerebral-blood-flow images during functional brain activation and for analyzing these images has been developed at this center over the past several years. Initial studies have shown that this approach is an efficient and powerful tool for studying the functional organization of the human central nervous system. To maximize the use of this technology, we have chosen to collaborate with investigators outside the Washington University Medical Center.

Collaboration has been initiated for several reasons. First, the neurophysiological sophistication of the experiments performed should be commensurate with the technical sophistication of the PET methods utilized. This is best accomplished by collaboration or consultation with experts in each field of study. Second, as our facility is unique and costly to maintain, tomograph utilization should be as nearly continuous as possible. We have found that the time required for PET data acquisition is quite small relative to that of experiment design and development, data analysis and interpretation. Collaboration with other investigators who are willing to learn PET data analysis techniques, and who bring with them expertise in stimulus development and experiment design, increases the productivity of our facility. This is clearly important as our facility is unique and costly to maintain. Third, this gives other scientists an opportunity to use PET to test in the human brain hypotheses that they have developed through their work in other fields. Finally, we anticipate that new methods of data analysis and manipulation will grow from the transfer of ideas allowed by collaboration with experts in fields outside of PET.

Three investigators from the Division of Biology of California Institute of Technology are now active collaborators: John M. Allman, Ph.D., David C. Van Essen, Ph.D., and Francis Miezin, M.S.. All three are established visual-system biologists. All are active in studying striate and extra-striate visual systems in higher non-human primates, particularly

the macaque and owl monkey. Their knowledge of visual-system physiology is necessary for optimal sophistication in visual experiment design. In later phases of this project, their continued work in non-human species will guide selection of hypotheses to be tested and experiment design.

In addition, Dr. Judith Lauter of the University of Arizona (Department of Speech and Hearing) will become an active investigator after the placement of her satellite system in early October.

The computer system (which is totally funded by the collaborating institutions), is fully compatible with that used in our laboratory for stimulus presentation and image analysis. The system includes: a Perkin-Elmer 3205; two Lark disk drives; and a Ramtek 9465 image display system. The collaborators have already spent considerable time in our laboratory learning the stages of data acquisition and processing. Scan data acquired in our laboratory will be transferred to the participating institutions for processing and analysis. Similarly, software developed at the collaborating institutions may be transported to this laboratory on a mini-disk for local use.

E. Systems for Specialized Biomedical Studies

This section describes projects that do not fall readily into the major sub-sections of this report. Some of the topics represent applications of previously described technology whilst others are adventurous forays into new and as yet uncharted territory.

In the first of these categories, new hard- and software techniques have been applied to long standing problems as in the combination of statistical and data acquisition systems for scintillation studies and in the development of stimulus generators for use in the neurosciences. Here, the capabilities of modern color displays and computer software produce a convenient, flexible and reliable tool.

Also, work has progressed systematically on the development and application of an algorithm based on the maximum-likelihood method for estimating the spatial distributions of radioactive intensities from electron microscopic autoradiographs. Related work on automated segmentation of biomedical images is motivated by the needs of the electronmicroscopic autoradiography project but has much broader applicability.

In the second category, work on detailed mapping of chromosomes has continued, expanded in scope and now offers the prospect of describing large DNA molecules within an acceptable time span.

Finally, work continues on the development of computer models that are more representative of the acid-base relationships of in vivo blood than have previously been attained.

E-1. DNA Restriction Mapping

Personnel: J. S. Turner, BCL
M. V. Olson, Ph.D., Genetics

Support: RR 01380
GM 28232
Washington University

The discovery of site-specific restriction endonucleases in 1970 has, in principle, opened the way to the detailed physical mapping of the chromosomes of any organism. These enzymes recognize short, precisely defined sequences in DNA and cleave the DNA double helix at or near their recognition sites. The central importance of restriction enzymes in any DNA-mapping project arises because the sites provide simple landmarks along the otherwise monotonous backbone of a DNA chain. The strategy being developed for mapping extremely complex DNA sequences is based on working with fragment-size data alone. This method, described in [1], relies on the analysis of a large set of partially overlapping clones to order both the clones themselves and the restriction sites present in the redundantly sampled source DNA.

The work in the past year has focused on an analysis of the intrinsic complexity of the mapping problem and the development of effective algorithms for it. We have shown that the general mapping problem is NP-complete by means of a transformation from the well-known shortest common superstring problem [2]. The close relationship of the shortest common superstring problem (SCS) to the general mapping problem has motivated an investigation of approximation algorithms for SCS. We have developed several algorithms that yield near optimal solutions, by exploiting relationships with the longest path problem in graphs and the asymmetric traveling salesman problem [3].

We have investigated a simple greedy algorithm for the general mapping problem through a series of statistical simulations. This work makes it clear that this algorithm cannot be expected to accurately construct a restriction enzyme map, but the analysis of how it fails has led us to a new algorithm which is now under investigation. The new approach is capable of much greater accuracy than those considered earlier, appears fast enough for large DNA molecules and does not require the use of backtrack search.

1. Olson, M. V., Dutchik, J. E., Graham, M. Y., Brodeur, G. M., Helms, C., Frank, M., MacCollin, M., Scheinman, R., and Frank, T., "A Random-Clone Strategy for Genomic Restriction Mapping in Yeast," Washington University School of Medicine, Department of Genetics, 1986.

2. Turner, J. S., "The Complexity of the Shortest Common Matching String Problem," Washington University Computer Science Department, WUCS-86-9, 4/30/86.

3. Turner, J. S., "Approximation Algorithms for the Shortest Common Matching String Problem," Washington University Computer Science Department, WUCS-86-16, 7/18/86.

E-2. A Quantitative Model for In-Vivo Acid-Base Relations

Personnel: L. J. Thomas, Jr., BCL

Support: Washington University

Work has continued on a model to represent the acid-base relations of the blood in vivo. The model will account for steady-state equilibrium between the blood and interstitial fluid (plus lymph), the transition from mixed venous to arterial blood, and for intracellular buffering as well as metabolic acid production. The object is to achieve an improved analytic representation of the composition of in-vivo arterial blood so that clinically available data can be used to achieve more precise quantification of acid-base abnormalities than is possible by the empirical approximations now in general use.

Because the substantial buffering capacity of hemoglobin varies as a function of its oxygen saturation, an analytic expression for the sigmoid oxy-hemoglobin dissociation curve is necessary to the model. Accordingly, recent work has focused on developing an algorithm for expressing the dissociation curve at a precision comparable to the experimental errors in the data upon which the currently accepted "standard" dissociation curve is based. A review of the literature showed that the standard error of the best data available is about 0.1% saturation at low and high oxygen saturations and about 0.5% saturation in the midrange.

Many workers have developed analytic expressions for the standard oxy-hemoglobin dissociation curve, but none achieves a fit to the standard curve within the error bounds of the data. Of the published algorithms, the five best were programmed and evaluated by comparison with the current standard curve and by testing for numerical stability over the full range of oxygen tensions, from 0 to 1000 Torr. The best was numerically stable but showed an error about five times the standard error of experimental measurements at an oxygen tension not far from that of normal arterial blood. All of the others showed larger errors or were unstable at one region of the curve or another.

A sound theoretical expression for the oxy-hemoglobin dissociation curve, based on the known physico-chemical interactions of oxygen with hemoglobin was developed by G. S. Adair in 1925. Adair incorporated the four equilibrium constants for the interactions of oxygen with the hemoglobin molecule in an expression that is essentially the ratio of two quartic polynomials. The Adair formulation, however, does not fit the experimental data satisfactorily. For example, errors of over 1% saturation are encountered at a saturation close to that of normal mixed-venous blood. None of the algorithms considered above employs the Adair expression or variations thereof. In his last published paper, F. J. W. Roughton showed evidence to suggest that the deviation of the Adair equation from experimental data is a systematic function of oxygen saturation and suggested that the theoretical shape of the curve may be modified by an intracellular enzyme (2,3-DPG) which is now known to perturb the affinity of hemoglobin for oxygen as a function of oxygen saturation.

After exploring a number of variations of published algorithms in unrewarded attempts to achieve a more satisfactory fit to the oxyhemoglobin dissociation curve, the Roughton hypothesis was adopted and a piece-wise Adair-function was tried. The Adair function was used for a spline fit to the standard dissociation curve. With only four knots (at oxygen partial pressures of 20, 34, 44, and 75 Torr), the entire curve was fitted to within 0.1% saturation. That result is within the standard error of the standard curve at the extremes and about one fifth the standard error in the midrange. Moreover, the Adair expression is devoid of numerical instabilities throughout the full range of the standard curve as well as at extremely high oxygen tensions where some of the other algorithms fail.

The piece-wise Adair-function algorithm is being incorporated into the model reported last year (PR 21, E-3). As time permits, efforts in the coming year can now be turned to algorithms for including in the model the transition from mixed-venous to arterial blood and the release of acids from the intracellular space.

E-3. Isolated-Scintillation Probe Data Acquisition System

Personnel: D. E. Beecher, BCL
H. D. Ambos, Medicine
S. R. Bergmann, M.D., Ph.D., Medicine
M. A. Brown, M.D., Medicine
W. P. Hellberg, BCL

Support: RR 01380
HL 17646

The system as described in PR 21, E-4, is now installed, fully operational and routinely used for isolated-probe studies. Several small problems concerning data collection methodology and curve analysis techniques were identified and corrected in the early on-site testing phase.

This LSI 11/23 system is also being used for additional data analysis which requires a collection of various small-scale analysis routines. Implementation has begun on this system of "statistics-calculator" programs.

Integration of these programs and printer-plot capability will be achieved by storing input and output data in text files which can be examined and altered by the user using standard DEC text-editing facilities. The most comprehensive of the programs, STATPAC, includes Linear Regression and complete Analysis of Variance (ANOVA) capabilities.

Design emphasis is on practical user ergonomics with consistent "rules" for program behavior and data storage, while reducing implementation complexity.

E-4. Maximum-Likelihood Estimation Applied to Electron-Microscopic Autoradiography

Personnel: M. I. Miller, BCL
K. B. Larson, BCL
B. Roysam, BCL
J. E. Saffitz, M.D., Pathology and Medicine,
D. L. Snyder, BCL and Electrical Engineering
L. J. Thomas, Jr., BCL

Support: RR 01380
HL 17646

A new method for analysis of electron microscope autoradiographs has been described ([1] and PR 21, E-6) which is based on the maximum-likelihood method of statistics for estimating the intensities of radioactivity in subcellular organelle structures. A Poisson statistical model describing the autoradiographic grain distributions is adopted, which we prove results from the underlying Poisson nature of the radioactive decays as well as the additive errors introduced during the formation of grains. Within the model, an iterative procedure derived from the expectation-maximization algorithm of mathematical statistics is used to generate the maximum-likelihood estimates. The algorithm has the properties that at every stage of the iteration process the likelihood of the data increases; and for all initial non-zero starting points the algorithm converges to the maximum-likelihood estimates of the organelle intensities.

The maximum-likelihood approach differs from the mask-analysis method and other published quantitative algorithms in the following ways:

1) In deriving estimates of the radioactivity intensities the maximum-likelihood algorithm requires the actual locations of the grains as well as the micrograph geometries; each micrograph is digitized so that both the grain locations as well as the geometries of the organelle structures can be used.

2) The maximum-likelihood algorithm iteratively computes the minimum-mean-squared-error estimate of the underlying emission locations that resulted in the observed grain distributions, from which intensity estimates are generated; this algorithm does not minimize a Chi-squared-error statistic.

3) The maximum-likelihood approach is based on a Poisson model and is therefore valid for low-count experiments; there are no minimum constraints on data collection for any single organelle compartment.

4) The maximum-likelihood algorithm requires the form of the point-spread function describing the emission spread; a probability matrix based on the use of overlay masks is not required.

5) The maximum-likelihood algorithm does not change for different organelle geometries; arbitrary geometries are incorporated by maximizing the likelihood-function subject to the geometry constraints.

The new method and preliminary evaluations of the quantitative accuracy of the maximum-likelihood and mask-analysis algorithms have been reported [1-3]. Based on two different phantoms in which we compared the squared-error resulting from the two algorithms, we find that the new maximum-likelihood approach provides substantially improved estimates of the radioactivity intensities of the phantoms.

The simulations described above were systematically extended in scope to cover increasingly realistic situations. First of all, the single-geometry simulations using a Gaussian point-spread function were extended to low-count conditions wherein the performance measures were gathered by performing multiple-realizations on a single phantom. These experiments confirmed our prediction that even when the geometry of micrographs does not vary, i.e., when transition probabilities can be computed perfectly, the maximum-likelihood algorithm outperforms the mask-analysis algorithm. We attribute this to the exploitation of actual grain coordinates and to the Poisson model.

We next implemented the $\cos^3$ point-spread function developed in [1]. This was made possible by the derivation in closed-form of the integral of the point-spread function over a rectangle. Of the several symmetrical forms that were discovered for this function, a form that uses only the primitive operations available in current floating-point units was chosen. This permitted a substantially more efficient implementation technique employing quadtrees (see E-5). These single-geometry simulations confirmed the superiority of the maximum-likelihood approach for the true point-spread function and showed that at low counts it is permissible to ignore grains at substantial distances from the emission region. This result supports the validity of a true multiple-independent-micrograph implementation.

Finally, we extended the simulations to cover the multiple-independent-micrograph case. This was made possible by the derivation in closed-form of the fourth-order integral for the transition probability between two arbitrary rectangles. This speeded up the transition probability computation by three orders of magnitude. A secondary implication of this formulation is a substantially improved and automated alternative to the mask-analysis procedure for computing transition probabilities. The multiple-geometry simulations demonstrated that compared to single-geometry case, the maximum-likelihood algorithm showed very little degradation in performance, whereas the mask-analysis performance degraded substantially.

1. Miller, M. I., Larson, K. B., Saffitz, J. E., Snyder, D. L., and Thomas, Jr., L. J., "Maximum-Likelihood Estimation Applied to Electron-Microscopic Autoradiography," Journal of Electron Microscopy Technique, vol. 2, pp. 611-636, 1985.

2. Miller, M. I., Larson, K. B., Saffitz, J. E., Snyder, D. L., Thomas, L. J., and Roysam, B., "A New Method for Analysis of Electron Microscopic Autoradiographs," Journal of Cell Biology, vol. 101, no. 5, (pt 2), p. 85a, 1985 (abstract).

3. Miller, M. I., Roysam, B., Saffitz, J. E., Larson, K. B., Thomas, Jr., L. J., "Validation of Maximum-Likelihood Analysis of Electron Microscopic Autoradiographs," Proceedings of the 70th Annual FASEB Meeting, St. Louis, MO, vol. 45, no. 3, p. 470, 1986 (abstract).

E-5. Automated Segmentation of Biomedical Images

Personnel: D. R. Fuhrmann, BCL
S. Akhtar, BCL
M. A. Brown, BCL
H. A. Drury, BCL

Support: RR 01380

This project began in response to the needs of researchers in electronmicroscopic autoradiography (EMA) [1] for a description of subcellular geometries in electron microscope cell images (E-4). The original and ultimate goal of the project is the completely automated segmentation of digitized images by texture analysis or similar computational method. In the interim, however, it was found that a reliable interactive data acquisition system was required so that EMA research could continue without interruption.

The EMAMAP software package for data acquisition was completed May 1986 [2]. With this system, a biologist or trained operator places a black-and-white enlargement of the original EM photograph on a graphics tablet, and hand-digitizes the edges of the desired structures. The regions enclosed by these edges are then classified by the operator according to a small list of organelle types. The resulting segmented image is stored externally in a raster-scan format.

One outgrowth of the EMAMAP project was the recognition of a need for more efficient data structures for the segmented images. Recent work has concentrated on the use of quadtrees toward this end [3]. It was found that a typical EMA image of 200k pixels could be stored externally with less than 10k bytes, and could be represented internally with 60-150k bytes, under this quadtree format. Furthermore, many image processing operations such as numerical 2-d integration are thereby facilitated. Several significant improvements to published quadtree-based image processing algorithms have been developed. It is anticipated that a software package functionally similar to EMAMAP but based on quadtrees will be completed by Fall 1986.

1. Miller, M. I., Larson, K. B., Saffitz, J. E., Snyder, D. L., and Thomas, Jr., L. J., "Maximum-Likelihood Estimation Applied to Electron-Microscopic Autoradiograph," Journal of Electron Microscopy Technique, vol. 2, pp. 611-636, 1985.

2. Fuhrmann, D. R., Drury, H., Akhtar, S., and Brown, M., "EMAMAP: An Interactive Data Acquisition Program for Electron Microscopic Autoradiography," BCL Monograph No. 474, June 1986.

3. Fuhrmann, D. R., and Brown, M. A., "Encoding Biomedical Images with Quadtrees," submitted to 1986 Allerton Conference on Communications, Control, and Computing.

E-6. Color Perimetry Studies

Personnel: W. M. Hart, Jr., M.D., Ph.D., Ophthalmology

Support: Washington University

This project has been dormant for the past year while awaiting renewal of support from the National Eye Institute. Therefore, no changes in hardware configuration or further developments in software design have been implemented, and no additional groups of patients have been examined. Notice of renewal of NEI support for use of the system (for a study of glaucoma over the next 5 years) was received effective July 1, 1986. Accordingly, work is now being re-started on modifications to the system to improve hardware reliability and to modify software so as to allow use of a new peripheral color-vision testing protocol. It is expected that 3 to 6 months will be required to bring the system back into full clinical use.

E-7. Software Development for Neurological Sciences

Personnel: D. E. Beecher, BCL
T. O. Videen, Ph.D., Neurology

Support: RR 01380
NS 06833

New visual-stimulus programs have been created for use in ongoing studies of the functional organization of the human visual cortex. These programs generate patterns on a Ramtek 9400 graphic display system. One program creates an alternating checkerboard pattern in which the checks are described by polar coordinates about a fixation point. The location, size, color and flicker frequency of angular checks is user-definable. A variation of this program allows the checks to be filled with random dots instead of a solid color. These programs have been used to reveal a topographical organization in human visual cortex using PETT.

Another program generates random-dot stereograms. The Ramtek display is divided into two halves of randomly-filled dots whose size and density are defined by the user. When the two patterns are optically aligned so that the images fuse, a checkerboard pattern appears in depth.

The size, number, and relative disparity of these 3-dimensional checks can be changed as required. The random dot patterns change in pseudo random order and the checkerboard pattern flickers in depth at frequencies set by the user. However, when the images are not fused, no checkered pattern can be perceived, and the dots appear to move in a random manner. This stimulus is being used to investigate the localization of stereoscopy in the human visual cortex.

The redesign and programming of the software system for display and quantitative analysis of neurological PETT images is nearly complete. This software allows appropriate PETT images to be displayed showing blood flow, blood volume, tissue activity, or the rate of oxygen utilization. Users can define specific regions for quantitative analysis. This new software system can be used with either PETT VI or Super PETT II images, and has been designed to be both more user-friendly and more easily maintained than existing software.

F. Resource Development Activities

Resource development activities are those which contribute to the goals of more than one major program of the laboratory, address the needs of individual users who can benefit from the expertise of the BCL staff and the inventory of computing and specialized test equipment, or identify new technologies which may become appropriate foundations for new experimental tools. Service to users does not follow the usual computation-center pattern with an established fee schedule and a highly centralized facility. Rather, senior laboratory staff members consider requests for assistance from investigators who must address a particular biomedical computing problem. If an appropriate technology exists, investigators may be referred to commercial vendors or fee-for-service organizations when these are available. In other cases, problems may be approached by the laboratory provided that the effort complements other activities of the laboratory. Many times the project can be assigned to a staff member with appropriate experience and completed in a short time. The investigator then has his or her results, and a short note describing the work will appear in the annual report and perhaps the open literature. A few projects, however, may develop into major initiatives within the laboratory. Most of the major projects began in this fashion and the opportunities that supporting activities provide are valued.

The IPAQ project (F-1 thru F-7) has focused laboratory efforts on providing a computational environment which can be utilized in addressing the demanding needs of algorithm development. A distributed approach, multiple computing systems integrated with communication networks, is being developed. Equipment acquisition, system integration and software installation and development have dominated this reporting period.

Continuing studies and measurements on broadband cable transmission (F-8) support both local and campus-wide networking projects. Studies of a modified approach to ray-tracing for three-dimensional volume representation utilizing two-dimensional display devices have continued (F-9). A reflectance camera with digitized output has been obtained and is being evaluated (F-11) for use as an acquisition device for biomedical photographic images.

Many digital hardware designs are one-time, special purpose projects. Others may have wide appeal and construction of multiple copies may result, as in the case of the TERRANET local network (F-10). System development activities included the data communication laboratory exercises (F-12) and the exportation of the FORTRAN utilities for the HP 7475 plotter (F-13).

F-1. A Distributed Facility for Image Presentation, Analysis and Quantification (IPAQ)

Personnel: G. J. Blaine, BCL
D. E. Beecher, BCL
M. A. Brown, BCL
K. W. Clark, BCL
J. R. Cox, Jr., BCL
R. E. Hermes, BCL
S. M. Moore, BCL
S. R. Phillips,BCL
F. U. Rosenberger, BCL and Computer Systems Laboratory

Support: RR 01380
RR 01379
Digital Equipment Corporation
Washington University

Decentralized computing organized along departmental and research laboratory lines characterizes the environment which continues to evolve at most major medical research institutions. This is particularly true in quantitative imaging where many projects have diverse image-data sources (modalities), different data-acquisition requirements, and dissimilar methods for the extraction of quantitative information. Rather naturally, diverse computing styles and equipment choices have evolved. For example, our major collaborative research groups support installations tailored to their specific measurement and picture transformation needs, for which display peripherals from a variety of manufacturers (DeAnza, Ramtek, and Lexidata) are tightly coupled to different computers (DEC 730, 750, 780, PE 3230, 3242). Commonality is limited to little more than the popularity of Vax-class computers and a FORTRAN programming environment. Furthermore, the lack of common program-development tools and display-support software has minimized the opportunities for sharing developments across research programs and has necessitated large host-specific investments by those Resource researchers and collaborators who participate in modeling and algorithm development.

Algorithm development is often characterized by computationally demanding and memory-intensive tasks which must compete with concurrent usage of the existing computing resources for data acquisition and analysis activities. The limited computational capacity available for algorithm development and pressures for expediting the research process biases the investigator's attention toward ad hoc approaches to improvements in execution performance, often at the expense of fundamental algorithm studies which are more likely to yield long term benefits.

The broad goal of this core research and development activity is to create an environment for biomedical image presentation, analysis and quantification (IPAQ) which:

1) is focused on fundamental algorithm developments that individual biological scientists may not have the time, patience or resources to pursue;

2) provides an integrated approach to expedite the development and export to the local and national communities of new algorithms for improved quantification of biological information;

3) improves access for purposes of algorithm development to data from the diverse imaging modalities to encourage modality integration; and,

4) protects existing investments in decentralized and specialized biomedical research systems.

A series of study efforts led to the definition of an architecture and specification of system components capable of addressing the needs of quantitative imaging. The components of the distributed IPAQ facility are to include: 1) acquisition nodes consisting of the specialized imaging resources at the sites of the collaborations; 2) computation-oriented nodes to support development and initial evaluation of algorithms within the Resource; 3) high-performance computation/display nodes which are tailored to export specialized computation and/or picture presentation; and 4) a high-bandwidth network to interconnect our development activities with the collaborative research.

Computer equipment selection, purchasing, and systems integration activities have dominated the current reporting period. Three Digital Equipment Corporation MicroVAX II's (node names: wubcl, wucon, wuipaq), a MASSCOMP MC-5400 (node name: wumcp3), storage peripherals, a Mercury Array Processor and networking components were added and brought to an operational state in the past six months. The current system resource configuration is illustrated in Figure 1. Three levels of interconnections are illustrated:

a) terminal service at 9600 bps via TERRANET (F-10),

b) UNIX-UNIX service using TCP/IP over a baseband Ethernet (F-5), and

c) DECNET-UNIX service using DECNET-ULTRIX over Ethernet on the MIR broadband cable system (F-8).

Specifics of the IPAQ activities are summarized (F-2 thru F-7).

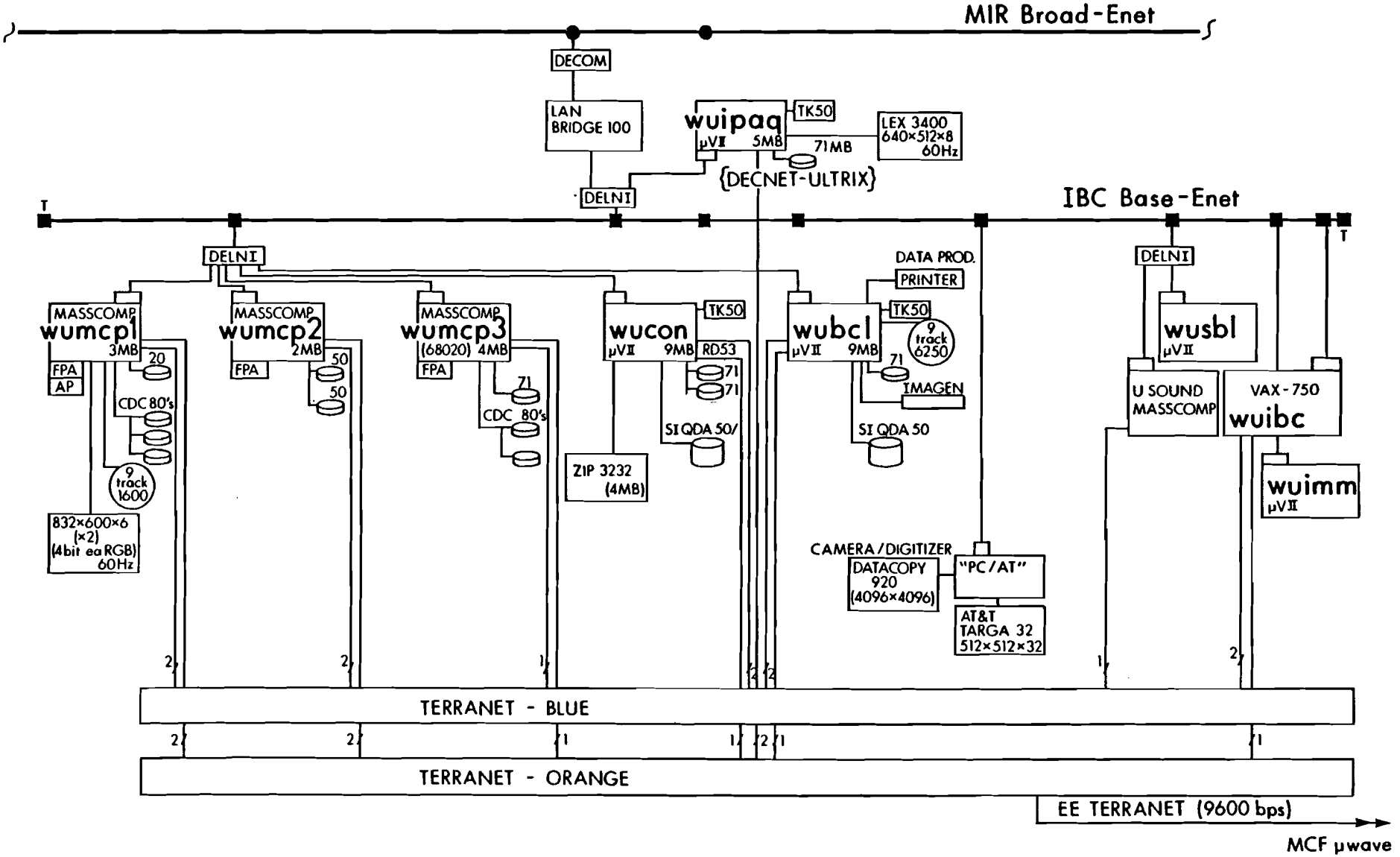

Figure 1. IPAQ Resource Configuration

F-2 IPAQ: System Integration

Personnel: R. E. Hermes, BCL
M. A. Brown, BCL
K. W. Clark, BCL
S. M. Moore, BCL
S. R. Phillips, BCL

Support: RR 01380
Digital Equipment Corporation

Selection and acquisition of new computer systems and related equipment and the integration of new equipment with existing resources during the past year has significantly improved the research and computing environment at the BCL. Previous dependence on a pair of PDP 11/34s has been supplanted by the addition of three MicroVAX and three MASSCOMP super-microcomputers. Current computing resources and associated primary applications are summarized in the following table.

	WUIPAQ	WUBCL	WUCON	WUMCP1	WUMCP2	WUMCP3
Machine Type	MicroVAX II	MicroVAX II	MicroVAX II	Masscomp 5500	Masscomp 5500	Masscomp 5400
Terminal Ports	9	17	9	11	11	4
Memory Size	9 MB	9 MB	9 MB	3 MB	2 MB	4 MB
Disk Configuration	2-RD53/71 MB	RX50 Floppy 1-RD53/71 MB 520 MB [Eagle]	RX50 Floppy 1-RD53/71 MB 520 MB [Eagle]	Floppy 64 MB [Winch.] 3-9762/67 MB	Floppy 84 MB [Winch.]	Floppy 71 MB [Winch.] 2-9762/67 MB
Other Devices	Floating Point Ethernet TK50 Lexidata	Floating Point Ethernet TK50 9-track tape Imagen Laser Pr DataProducts Pr	Floatint Point Ethernet TK50 Mercury AP	Floating Point Ethernet Masscomp AP Graphics Proc.	Floating Point Ethernet	Floating Point Ethernet
Application Areas	Communications Studies Computation	Program Dev. Text Processing Computation	Program Dev. Computation	Program Dev. Computation Graphics	Text Processing	Program Dev. Computation

All systems use the UNIX operating system and support the FORTRAN and C programming languages thereby allowing software developed on one machine to be executed on another. This development environment is further enhanced by system communication via Ethernet providing users easy access to files on other systems within the Resource. Other network connections provide access to the laboratories of collaborators (F-5). Terminal connection is provided via the dual Terranet networks, direct connection, or virtually via Ethernet.

Since each system serves a particular research effort, the machines were configured to best suit the expected needs of that effort. The machine "wumcp1" supplies most of the graphics needs, whereas, "wucon" and its array processor and large disk capacity is ideal for handling more specialized computing needs, and the machine "wuipaq" with less disk capacity is more than adequate to serve the needs of the network and communications studies. The machine "wumcp3" is a resource dedicatible to running compute intensive algorithms which don't require the array processor. Program development, documentation, and other text entry needs are served by "wumcp2" and "wubcl". This distributed approach to computing allows the dedication of certain computing resources to specific research activities when necessary without hindering or prohibiting other users from computer access.

This computing environment is augmented by the addition and integration of a variety of data acquisition and output devices. These include a Lexidata Imaging System for image display, a DATACOPY reflectance camera for image acquisition (F-11), a Mercury Array Processor (F-6), an Imagen Laser Printer (F-3), and a Hewlett Packard Laserjet printer.

Several significant milestones have been crossed during the past year: a near ten-fold increase in computing capacity, an eight-fold increase in disk storage capacity, efficient data transport within the laboratory and more importantly to collaborator's laboratories, and a coherent program development environment across all computing resources. The major result being the existence of a distributed system of computing resources which provides a more productive atmosphere for conducting basic research.

F-3 IPAQ: Systems Support

Personnel: R. E. Hermes, BCL
D. E. Beecher, BCL
M. A. Brown, BCL
K. W. Clark, BCL
S. M. Moore, BCL
S. R. Phillips, BCL

Support RR·01380

Support and development of the local computing environment continues to be an important laboratory activity, particularly during the past year because of major equipment acquisitions (F-2). A major goal has been to provide a computing environment which is coherent across distributed computer resources and to provide the software tools necessary for conducting basic research.

Coupled with the acquisition of multiple MicroVAX systems, and additional MASSCOMP systems was the decision to continue to rely upon the UNIX operating system. Because UNIX provides an operating environment which can be supported on diverse systems, and has excellent support for system communications, we chose to use Digital Equipment's Ultrix-32M on the MicroVAXes and MASSCOMP's RTU on the MASSCOMPs. Both versions of UNIX are derivatives of Berkeley UNIX BSD 4.2 with enhancements from AT&T System V. A significant effort was expended to become familiar with and install Ultrix on each system. In addition, a new release of the RTU system was installed on each MASSCOMP.

Operating system installation was coupled with the setup of the networking software, importing of software already operating on other local UNIX systems, installation of support software for controlling peripherals, and user familiarization with new systems and software. Although many local computer users were familiar with the UNIX operating system, some were not; others were unfamiliar with the new versions of software. To better service the user community, a mail system to handle system and user

problems was established whereby problems could be addressed on a timely basis by a small group of system coordinators. This method allows problems to be handled quickly, without the need for full-time system managers for each system.

With a relatively large number of multiuser systems and no full-time system managers, the problem of day-to-day system supervision for potential maintenance problems becomes difficult to handle. For instance, each machine would require a printing console terminal. To alleviate this problem, a locally developed software system for monitoring system consoles [1] was installed and deemed acceptable. Full functionality of the system will be realized when a special hardware multiplexor is installed.

Considerable effort has been spent developing support for an Imagen Laser printer. The Imagen printer is capable of producing typeset documents in addition to being able to output graphical information. To support typesetting, Unix typesetting software, DITROFF, was acquired and installed. A substantial number of software modules were supplied with the printer which support the wide variety of printer capabilities. Printer access is available from all machines on the local Ethernet.

One MASSCOMP system supports most of the high performance graphics needs, however an existing Lexidata Image Processor has been interfaced to a MicroVAX. A UNIX driver was written to support the device so that it could be used as a quick-view image station.

1. Ziring, N., "Conch: A Network Service for Console Access," Memorandum, Washington University, Engineering Computer Laboratory, 1985.

F-4. IPAQ: Image Presentation

Personnel: D. E. Beecher, BCL
M. A. Brown, BCL
R. E. Hermes, BCL
S. Husodo, BCL
Y-M. Kwan, BCL
S. M. Moore, BCL
J. B. Zimmerman, D.Sc., Radiology and Computer Science

Support: RR 01380
Washington University

Work has been initiated in several areas within image presentation, namely, image file formats, network considerations, image manipulation utilities, image presentation utilities, and 3-dimensional display of image data. Three-dimensional display is covered in section F-9.

Selection of Image File Format

Image file formats used within the Washington University community were examined to determine not only their requirements but also the efficacy of adapting one of them into an IPAQ standard. Included in these were formats for Radiation Sciences (PETT VI, Super PETT I, and Super PETT II), Laboratory of Neuro Imaging (LONI), Hilltop campus Image Processing Laboratory, and various CAT scanner formats. Diverse requirements for each format were found, with none being sufficiently flexible to accomodate the others.

The collaborative nature of research activities within the laboratory implied that an IPAQ format be able to accomodate these image formats which already exist within the Washington University community. With this goal in mind, a study of the ACR-NEMA digital image format standard was undertaken because of its flexibility and its applicability to medically-oriented images. Although the format is rather complex, its capability of dynamically creating new data types was very appealing. However, it was not clear that this image format would gain widespread acceptance, thereby creating the potential for supporting yet another "non-standard" image format. At this point, a review of the V-shell image format developed at the University of North Carolina was conducted. Many facilities use the V-shell format and associated image manipulation utilities included in the V-shell package. Through discussions with one of the implementors, we found that portions of the file handling routines could be quite easily modified to incorporate a new real-valued image data type which is necessary for some applications. Also discovered was the potential capability of storing secondary headers - which is very important for image conversion from different image processing sites. For these reasons we have adopted the V-shell routines and file format (modified) as an IPAQ digital image standard. Work is currently underway to install this package on the MicroVAX and MASSCOMP systems with additions necessary to handle real-valued images. After this installation, conversion routines to allow images to be passed between different installations within Washington University will be developed.

Also discussed was the problem of passing images over the University-wide network facilities and thus the need for a common network image format requiring only one conversion routine for images communicated over the network. Work is currently underway exploring possibilities for such a network format. The ACR-NEMA format will be scrutinized again in regard to the proposed network format.

F-5. IPAQ: Networking

Personnel: G. J. Blaine, BCL
R. E. Hermes, BCL
R. L. Hill, BCL and Radiology
S. R. Phillips, BCL
A. P. Rueter, B.S., Radiology
D. A. Schwab, BCL
E. Senol, BCL

Support: RR 01380
Washington University

Close coupling of our algorithm research, development and evaluation to the collaborative research areas is to be facilitated by a communication network which serves to federate distributed resources. Access to data from specialized imaging instruments located in our collaborator's laboratories is important to evaluating algorithm performance. Additionally, the communication network is to support presentation of images to our collaborating biomedical scientists. Quick-look capability should stimulate increased participation and reduce the time constant in the necessarily interactive evaluation of algorithm performance.

Information interchange between the distributed image acquisition resources within the medical center, the computation-oriented nodes at the BCL and the presentation nodes (currently located within BCL) can be functionally partitioned into "message" and "service" classes. Two-way query-based conversations are addressed by the "message network." Message network connectivity is supported by TERRANET (F-10), dedicated point-to-point 9600 bps channels on the MIR cable network (F-8) and 9600 bps channels on the Medical Computing Facilities inter-campus microwave link.

Error performance and robustness studies of the microwave-based channels and the FDM broadband cable channels were initiated on test channels which can be operated in a loop-back mode. Additional bit-error testor units (PR 21, F-3) were constructed for use in these studies. As error logging is from visual readout of an error accumulator, our sampling is rather coarse, and as a result the data are insufficient to support detailed correlation with weather and powerline events. "Average error rates" are indicated for weekly intervals as shown in Figure 1. The percentages which label each bar correspond to the valid collection interval for which the statistic is reported.

The transport of large data sets for access to measurement and image information is to be supported by bulk-transfer at high rate in a "service network." Our current "service network" is based on a baseband-Ethernet LAN which spans the Institute's medical campus facilities, and the backbone broadband-Ethernet LAN which is supported on the MIR cable network. A DEC LAN 100 Bridge supports inter-LAN traffic while minimizing backbone loading. Initial file transfer experiments, (MicroVAX-to-VAX 11/750 using DECNET/ULTRIX) indicate average transfer rates in the range of 600 to 750 Kbits per second are typical for a packet size of 2048 bytes and 1 Mbyte file transfers.

a). A 9600 BPS ASYNCH. PT-TO-PT COMMUNICATION CHANNEL FREQUENCY-DIVISION MULTIPLEXED ON THE OUTBOUND CABLE OF THE MIR BROADBAND CATV SYSTEM.

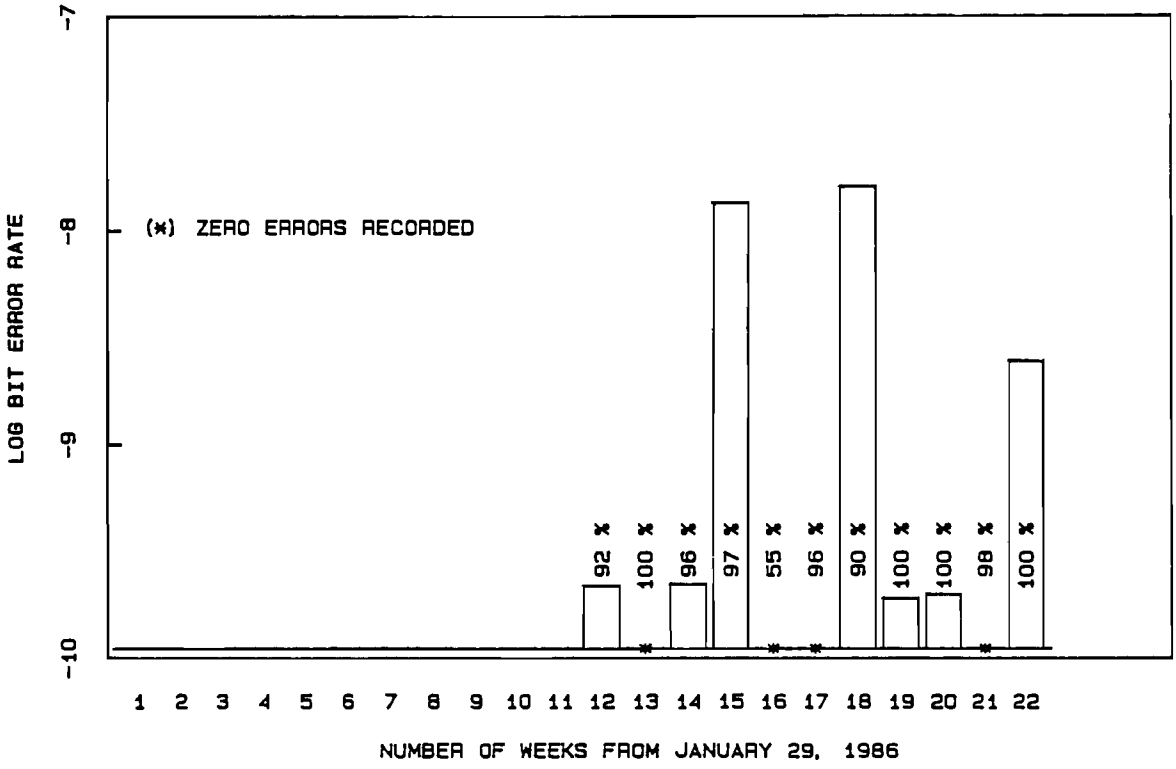

b). A SYNCHRONOUS CHANNEL OF A T-1 TIME-DIVISION-MULTIPLEX ON A 23 GHz MICROWAVE LINK.

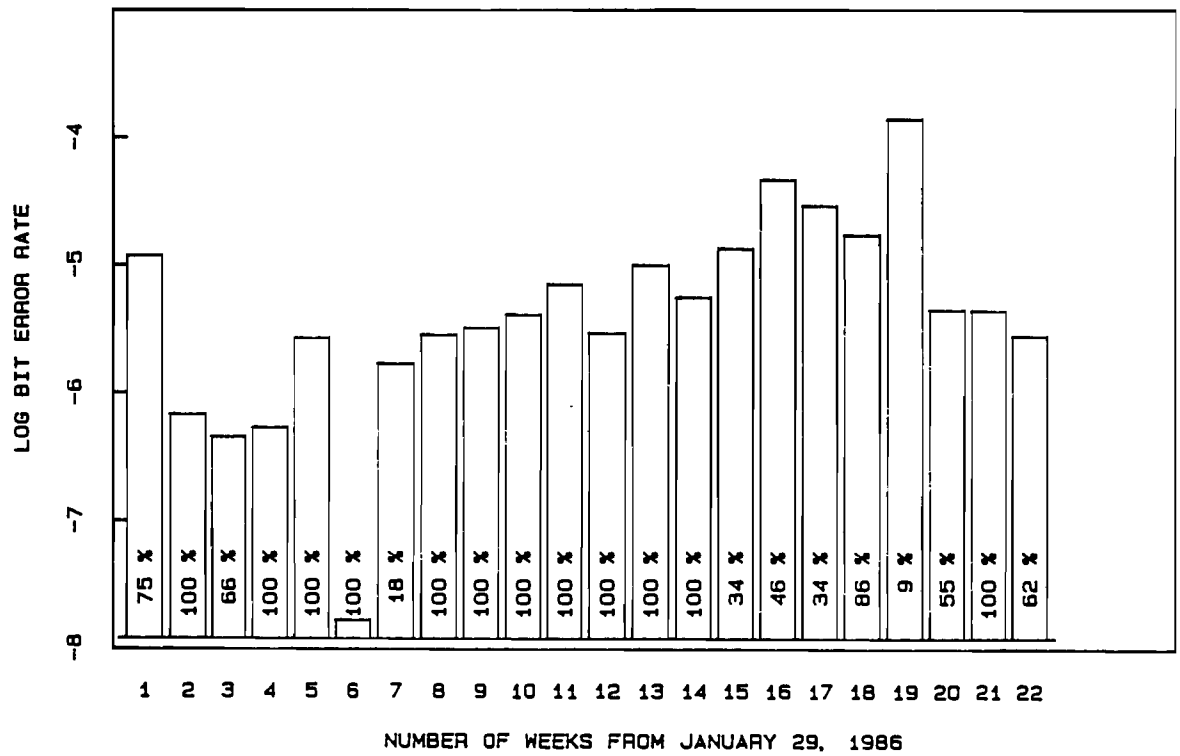

Figure 1. Average error statistics for 9600 bps data channels. The percentage-label associated with each one-week measurement interval indicates the quantity of data on which the error calculation was performed. Data loss resulted from the courseness of acquisition and instrument overflow conditions.

Four, 0-4 Mbps, broadband modems, were purchased from Coherent Systems Corporation. Modest cost (< $1000 per transceiver unit) and modest bandwidth (4 Mbps within a 6 MHz bandwidth) are features which may prove useful to future implementations of our "service-network." The modems transmit in the subsplit band (T9 17.75 MHz-23.75 MHz) and receive in the VHF high band (CH13 210-216 MHz). Research testing of the units was delayed while difficulties with the headend frequency-translator module were resolved.

F-6. IPAQ: Mercury Array Processor

Personnel: S. M. Moore, BCL
R. E. Hermes, BCL
B. D. Skinner, BCL
E. E. Witte, BCL

Support: RR 01380

A Mercury Computer Systems ZIP 3232+ array processor was purchased to enhance the computing power of a MicroVAX computer. The 3-board base system includes a 16 MFLOP array processor, 128 KB of data memory, and separate programming memories for the Control and Arithmetic Processors. The program memories for the Control and Arithmetic Processors contain 4096 40-bit microwords and 2048 32-bit microwords, respectively. Two additional boards contain a total of 4 MB of memory. Mercury Computer Systems also provided software for supporting the unit with the ULTRIX operating system. A device driver, utilities for building and debugging programs, and a library for performing standard vector operations were obtained.

An 8 MFLOP ZIP 3232 with 4 MB memory was received by February, but testing was not possible due to delays by the vendor in delivering software. Testing was begun in May following delivery of an upgrade to the 16 MFLOP ZIP 3232+ and software.

Preliminary tests of the ZIP focused on communicating with the array processor and understanding example programs supplied by the manufacturer. Formal tests were then initiated to examine the standard algorithm library provided by Mercury and to verify timing estimates found in the manuals. Errors were found in several routines in the standard algorithm library and reported to the vendor. Timing measurements of vector functions closely matched the estimates provided by Mercury for the 7 routines tested with the exception of the vector sine and exp routines. However, these two routines have bugs which are recognized by Mercury and are to be changed with the next release (2.0). Currently, the standard algorithm library is 70% complete, with the expectation that the next release due in August will provide routines that are currently missing or to replace those known to produce incorrect results.

Memory tests were written which wrote several patterns in the array processor memory and then read the memory for comparison. The pattern of errors we have detected by this method seems to indicate a problem in

software in the array processor and probably not in hardware. This problem was reported to Mercury along with the program which illustrates the error.

The next aim in this area is to use the array processor to implement the EM algorithm for providing the Maximum Likelihood estimate of PET images (D-5, D-8 thru D-10). Several versions of the algorithm will be implemented to allow study of how different implementations affect the computation time and the resultant image. Other plans include testing the new release of the standard algorithm library when it arrives and examining the numerical accuracy of the array processor.

F-7. IPAQ: Specialized Processor

Personnel: R. E. Hermes, BCL
E. T. Macke, M.S., Computer Systems Laboratory
R. E. Olson, Computer Systems Laboratory

Support: RR 01380
RR 01379

Exportation of computationally demanding algorithms may be facilitated by the integration of specialized processors into an engineering workstation. Such processors would be designed to implement computationally demanding portions of algorithms or carry out other special functions better suited to special hardware implementations rather than using the general purpose capabilities of a workstation. To examine the difficulty and problems associated with such an integration, a general purpose I/O board was integrated into a MASSCOMP workstation.

The I/O board was an Intel Multibus iSBC 519 Programmable I/O Expansion Board with multiple parallel ports. The first step was to determine the difficulty of writing a UNIX device driver. A first experiment included implementation of a MASSCOMP supplied general purpose device driver template. In so doing we were able to learn the necessary structure of a UNIX device driver. The MASSCOMP driver worked with few problems. The template driver was then modified with minor difficulty to support the Intel I/O board.

The UNIX I/O system is known to impose significant overhead on I/O operations. To determine the penalty imposed, a timing study was conducted for I/O operations via a UNIX driver versus direct device register access. The direct register access method merely required that special routines be developed to access the control registers of the target device without using the I/O facilities of the operating system. Repetitive writes to the I/O device were timed and recorded for each method.

Number of Writes	Unix Driver Method (sec)	Register Access Method (sec)
2000	1.3	Not Measurable
10000	6.2	Not Measurable
20000	12.5	Not Measurable
40000	25.1	Not Measurable
80000	50.3	Not Measurable
200000	Not Measured	0.7
1000000	Not Measured	4.1
2000000	Not Measured	7.5
4000000	Not Measured	15.6
8000000	Not Measured	30.2

As indicated in the table, register access is considerably faster than I/O via a driver, 7.55 microseconds vs 1.26 milliseconds per write. Therefore, in certain situations where time is a critical aspect of the problem, direct register access may be preferable, although it lacks the functional generality offered by driver access.

F-8. A Picture Communication System for Radiology

Personnel: G. J. Blaine, BCL
J. R. Cox, Jr., BCL and Computer Science
R. E. Hermes, BCL
R. L. Hill, BCL and Radiology
R. G. Jost, M.D., Radiology
A. Kumar, B.Tech., Radiology
S. R. Phillips, BCL
A. P. Rueter, B.S., Radiology

Support: RR 01380
RR 01379
Digital Equipment Corporation
Mallinckrodt Institute of Radiology
Washington University

A pilot cable system to transport analog and digital radiology pictures and support terminal-to-computer digital data transmission has been designed and installed (PR 21, F-3). A dual-cable 400 MHz system utilizes "off-the-shelf" cable television components to provide approximately 50 channels, achieved by frequency multiplexing channels of 6 MHz each. The system provides a workbench environment for the evaluation of commercial digital transmission equipment in addition to supporting experiments related to digital picture networking and archiving studies.

Studies and subsequent designs have been directed at communicating radiological images using channels based on frequency division of the 400 MHz channel. A bandwidth of 18 MHz is now utilized to support a broadband Ethernet channel. DECNET facilitates digital picture transport

from nuclear medicine and magnetic resonance instruments to Mallinckrodt's VAX 11/750 based archive. Links to the operational radiology information systems support image requests. Distribution of the retrieved image is currently limited to a small number of display sites and is supported by separate point-to-point analog transmission [1].

Development of a low-cost picture frame-buffer continued. The 512 x 512 x 8 bit/pixel frame-buffer was designed to support both parallel and serial data input and output. The 1 MHz serial synchronous interfaces were redesigned. The design is now based on a single fast microprogrammed machine which facilitates synchronization of the raster scan of the frame buffer with the serial output module. Initial tests of the new implementation indicate a substantial improvement in robustness.

1. Jost, R. G., Hill, R. L., Blaine, G. J., and Cox, Jr., J. R., "PACS Experience as a Motivation for a Campus-Wide Picture Network," Proceedings of SPIE, Application of Optical Instrumentation in Medicine XIV and Picture Archiving and Communication Systems (PACS IV) for Medical Applications, Newport Beach, CA, vol. 262, pp. 549-556, 1986.

F-9. 3-Dimensional Image Generation

Personnel: D. E. Beecher, BCL
J. R. Cox, Jr. BCL and Computer Science
F. U. Rosenberger, BCL and Computer Systems Laboratory

Support: RR 01380

Three-dimensional viewing techniques allow the biological scientist to gain more insight into data which is actually represented by a series of scan slices. The techniques described herein differ from the traditional solid modeling techniques in that we are trying to visualize known data, which is in the form of a voxel volume (see Fig. 1). Each volume element, (or voxel) represents an estimated quantity of attenuation, radionuclide distribution, etc; and the goal here is to accurately visualize the object (or objects) contained therein. Various techniques have been used for the visualization [1-5] and most recently, the techniques of Goldwasser, et al. [6-7], have been incorporated in a hardware implementation yielding real-time rotations of objects represented by voxel spaces.

The goal for this analysis is to reduce the number of voxels needed for processing with any given algorithm. The algorithm used by Goldwasser is clearly $O(n^3)$ in time due to the fact that all voxels contained in the volume are processed to generate the requested view. We will present techniques which greatly reduce the number of processed voxels thereby reducing overall execution speed.

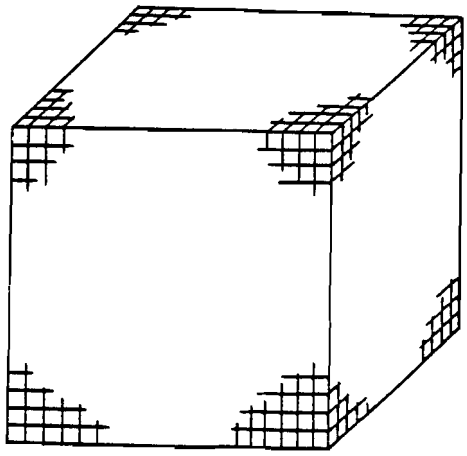

Figure 1. A generated voxel volume.

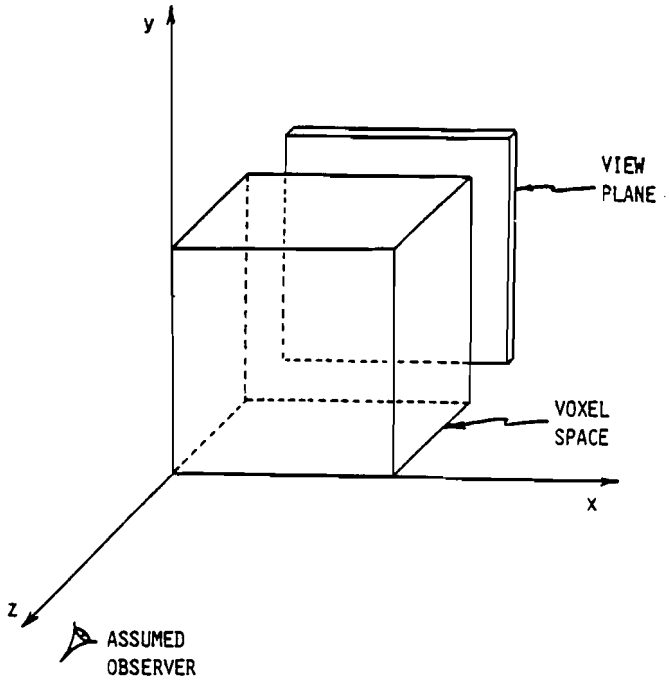

Figure 2. Initial configuration for back-to-front approach.

Basic Front-to-Back/Back-to-Front Approach

The basic idea is to manipulate an image plane into a position relative to the voxel volume in three-space such that the plane is perpendicular to a line parallel to the line-of-sight (see Fig. 2). We then move this plane through the volume using some increment to adequately sample the voxel space. This increment should be less than the width of a single voxel to ensure adequate sampling. When using the back-to-front technique, we always update the image plane when it intersects the object (as determined by thresholding), but with the front-to-back technique we update an image plane pixel only once; since that is the closest voxel in the object at that position. Image pixels are normally updated with a value proportional to the distance from the observer at that point.

It is straightforward to see that the front-to-back technique will be computationally less intensive because we update an image pixel only once, but we still look at all voxels in the volume.

Modified Approach-Ray Tracing

If, instead of moving the plane through the volume, we generate a ray from each image plane pixel along the line of sight, we can greatly reduce the number of voxels we need to examine (see Fig. 3). That is, for each pixel in the image plane, we radiate a ray along the line-of-sight until it intersects a voxel contained in the object, we then update the image plane with that distance value and we are finished with that pixel and do not examine any more voxels along that line of sight. This technique results in a great savings as far as voxels processed, and produces exactly the same image as do the other techniques discussed (see Fig. 4). Simulations run have shown a 33% decrease in number of voxels processed for the same phantom.

Current work

Work is currently underway to explore new techniques for object definition based on gradient changes in the voxel volume. This should produce more accurate surface definitions of the objects contained in the volume. These techniques are also being used in the design of an image manipulation module being locally developed by the Computer Systems Laboratory.

1. Artzy, E. Freeder, G., and Herman, G. T., "The Theory, Design, Implementation, and Evaluation of a Three Dimensional Surface Detection Algorithm," Computer Graphics and Image Processing, vol. 15, pp. 1-24, January 1981.

2. Farrell, E. J., "Color Display and Interactive Interpretation of Three-Dimensional Data," IBM Journal of Research and Development, vol. 27, no. 4, pp. 356-366, July 1983.

3. Fuchs, H., Dedem, Z. M., and Uselton, S. P., "Optimal Surface Reconstruction from Planar Contours," Communications of the ACM, vol. 20, pp. 693-702, 1977.

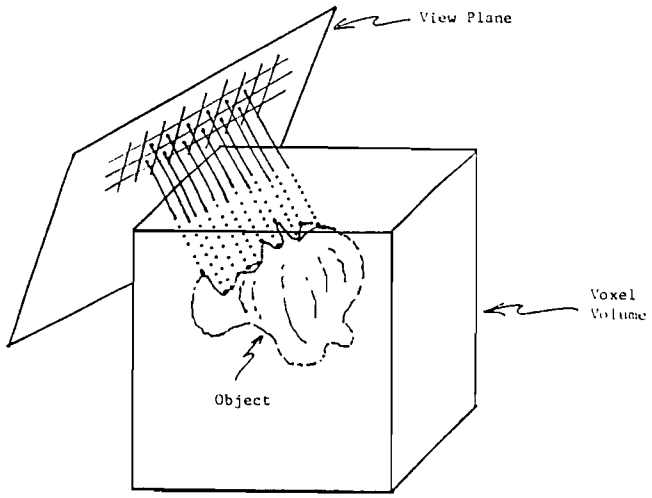

Figure 3. Modified ray-tracing approach.

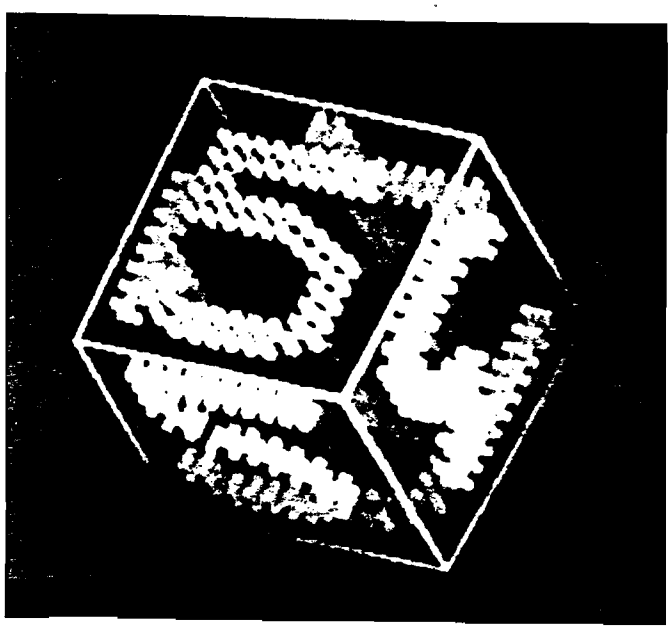

Figure 4. 3-D rendering (produced with either technique).

4. Lewis, M. H., Schlusselberg, D. S., Smith, W. K., Hagler, H. K., Woodward, D. J., and Buja, L. M., "Three-Dimensional Cardiac Morphometry with Computer Graphics," American Review of Diagnostics, vol. 2, no. 5, pp. 125-128, November-December 1983.

5. Robinson, D. E., "Display of Three-Dimensional Ultrasonic Data for Medical Diagnosis," Journal of the Acoustical Society of America, vol. 52, pp. 673-678, 1972.

6. Goldwasser, S. M., and Reynolds, R. A., "An Architecture for the Real-Time Display and Manipulation of Three Dimensional Objects," Technical Report No. MIPG77, Medical Image Processing Group, University of Pennsylvania, Philadelphia, PA, February 1983.

7. Goldwasser, S. M., Reynolds, R. A., Bapty, T., Baraff, D., Summers, J., Talton, D. A., and Walsh, E., "Physician's Workstation with Real-Time Performance," IEEE Computer Graphics and Applications, vol. 5, no. 12, pp. 44-57, December 1985.

F-10. An Experimental Local-Area Network: TERRANET

Personnel: G. J. Blaine, BCL
R. E. Hermes, BCL
S. Igielnik, Ph.D., Medical Computing Facilities
S. M. Moore, BCL
S. R. Phillips, BCL
D. A. Schwab, BCL

Support: RR 01380
Medical Computing Facilities
Washington University

TERRANET is now an integral part of the day-to-day operations of BCL. TERRANET provides terminal-to-computer and computer-to-computer communications for most multiuser computer systems in the laboratory. Nearly every office is equipped with a terminal tied to a TERRANET port; in addition, several public ports are available within BCL. Intersystem communication via TERRANET can be used to transfer text and data files. The initial TERRANET network (30 ports TERRANET-BLUE) has been augmented by a second parallel network (TERRANET-ORANGE). Communication between networks is accomplished through the use of 3 gateway ports on each network. Current resources on the two networks include 23 terminals, 20 ports to 9 distinct computer systems, and 5 modem or other network gateway connections.

A 9600 bps channel multiplexed onto the Medical Computing Facilities' microwave channel allows interconnection of our TERRANET ports to terminals and machine resources supported by the TERRANET configuration in the Electrical Engineering Department. The EE Department is located on the hilltop campus (approximately 2.5 miles from the medical campus).

F-11. An Evaluation of the DATACOPY Reflectance Camera

Personnel: D. E. Beecher, BCL
G. J. Blaine, BCL
R. E. Hermes, BCL
L. J. Thomas, Jr., BCL

Support: RR 01380

During the past year a Datacopy model 920 reflectance camera was acquired for offline image capture of opaque photographs/objects. The model 920 offers two resolution modes. In high resolution mode, an 8 1/2 x 11 page can be captured as a 3456 x 4472 pixel (8 bits/pixel) image, while in low resolution mode this is decreased to 1728 x 2800. The Datacopy was initially interfaced to an IBM PC/XT with a 10 megabyte hard disk. This system (on loan from IBM), was recently replaced by an IDS AT (a PC AT compatible) with 640 Kbytes of memory and 20 megabyte hard disk for image storage. The IDS is also configured with an AT&T TARGA 32 board which allows display and manipulation of true-color images (8 bits each - RGB).

Work is currently underway to utilize the gray-capture capability of the Datacopy camera. The TARGA board will be used to view these gray-scale images before they are shipped to other image processing stations. The goal is to create a dedicated image-capture facility to allow researchers a convenient mechanism for digitizing images into machine readable form.

F-12. Data Communication Laboratory Exercise

Personnel: D. E. Beecher, BCL
G. J. Blaine, BCL

Support: International Business Machines Corporation
Washington University

A course in Digital Data Communications (Computer Science: 423) was delivered in the Spring semester of 1986. The course was structured to include lectures and laboratory exercises in support of a data communications curriculum for Computer Science. Students were assigned 4 laboratories during the course of the semester to explore:

a) electrical characteristics of RS-232 communications,

b) various transfer protocols with associated error detecting and correcting techniques,

c) facsimile encoding and decoding, and

d) characteristics of network protocols and high-speed contention based communications schemes.

The laboratory exercises were designed to emphasize fundamentals and develop experience with performance metrics. Four IBM PC XT's, software, printers and the broadband-based IBM PC Network were loaned by the Academic Information Systems Division of IBM for development of the course. We found through the experience of teaching CS 423 that the laboratory portion of the course was an extremely valuable tool for the students. We are currently seeking support to acquire a permanent data communications laboratory which would be dedicated to supporting this course and other related courses which may be developed in the future.

F-13. A FORTRAN Interface for the HP 7475A Plotter

Personnel: T. O. Videen, Neurology
D. E. Beecher, BCL

Support RR 01380
HL 13851

The software library as described in PR 21, F-1, has been in routine use during the past year with no major changes. This implementation has been successfully ported to several laboratory systems (Perkin-Elmer 3205's), to allow software written on the larger mainframes to be used in the laboratory environment.

VI. INDUSTRIAL COLLABORATION

Industrial collaboration provides a mechanism for the deployment of laboratory developments. In addition, it benefits our staff by keeping us abreast of practical considerations of reliability, maintainability, and cost. During the past year, our formal collaborations have involved two ongoing projects, both in the area of electrocardiographic rhythm analysis. In one project, BCL analyzes tape-recorded ECGs for a pharmaceutical company which is evaluating an experimental cardiovascular drug. In the other project, BCL is helping a small company evaluate its implementation of a BCL-developed rhythm-analysis algorithm in a portable, real-time ECG analyzer.

For two and one-half years, BCL has analyzed long-term ECG recordings for a Mead-Johnson (Evansville, Indiana) sponsored "Multicenter Placebo-Controlled Study of Trazadone's Effects in Depressed Cardiac Patients" (PR 20, VI). BCL's contract to analyze these recordings was due to expire in October, 1985, but has since been extended. Patient recruitment from the clinical centers has fallen well behind projections, and Mead-Johnson is now negotiating with the FDA for an early termination of the study. Mead-Johnson has sent only 48 ECG recordings (from 12 patients) since July, 1985.

Since 1983, BCL personnel have worked closely with Biosensor Corporation (Brooklyn Center, Minnesota) to implement and refine the BCL-developed frequency-domain-based Argus ECG algorithms in a microprocessor-based real-time ambulatory patient ECG monitoring device. Biosensor markets a variety of systems and services (PR 21, VI). BCL personnel interact with Biosensor engineers to resolve algorithmic problems which typically arise in operational situations. In fact, several problems discovered in the long-term recording sessions prompted BCL personnel to refine our own algorithms and to construct a "clinical-event" database of 6-hour recordings (A-1). Prior to this we had relied solely on the AHA (3 hour) and MIT (1/2 hour) databases for algorithm development. This kind of interaction with Biosensor helps BCL keep research in touch with the commercial health-care sector.

VII. TRAINING ACTIVITIES AND SEMINARS

Training activities of the Biomedical Computer Laboratory are directed toward the goals of informing the local and national scientific communities about resource projects and facilities and of instructing a broad spectrum of people in the application of advanced computer-techniques to problems in clinical medicine and biological research. Training activities include the teaching of formal courses at the School of Medicine and the School of Engineering as well as supervision of graduate students by Laboratory staff. Both individual and small-group training about resource facilities are made available to the biomedical scientist. National workshops and symposia on topics of interest and importance to the resource and community are supported.

The bringing together of biomedical scientists, engineers, and computer scientists provides important cross-fertilization between disciplines. In these settings, students and staff find the need and opportunity to test the relevance of theory and the usefulness of technology in applications to real problems. Also, the biomedical scientists are aided in learning new techniques for acquiring useful information. To this end, some of the courses offered are addressed to biologists without strong technical backgrounds who want and need a below-the-surface appreciation of biomedical computing. Laboratory personnel also participate in regularly scheduled conferences in the clinical departments where both the biological and technological issues are examined.

Seminars and presentations relating to resource projects and applications are conducted by Laboratory staff as well as scientists and engineers from the national community. During the year the following activities were supported:

Seminars

"National Computer Conference - 1985: Review and Comments" July 18, 1985	Dr. G. J. Blaine Mr. R. E. Hermes Mr. S. M. Moore Biomedical Computer Laboratory Washington University St. Louis, MO
"Flexible's Supermini Computer" September 11, 1985	Mr. Ron Zachary Flexible Computer Corporation Dallas, TX
"The 11th International EEG Congress" September 18, 1985	Professor Harold Shipton Biomedical Computer Laboratory Washington University St. Louis, MO

"IMAGIS: An Image Information System" October 3, 1985	Professor Dr. Ir. Dick Boekee Delft University of Technology Professor Dr. Ab Bakker Ir. Kees Bijl Dr. Wim Heijser Dr. Ir. Jan Peter de Valk Leiden University Hospital The Netherlands
"Using NMR to Make Images: From Body to EMF and from EMF to Image" November 7, 1985	Dr. Tom Dixon Department of Radiology Washington University St. Louis, MO
"Current Clinical Successes and Shortcomings in Magnetic Resonance Imaging" November 14, 1985	Dr. Jay Hieken Department of Radiology Washington University St. Louis, MO
"Signal Processing Issues in Hazardous Aviation Weather Detection by Doppler Weather Radar" November 22, 1985	Dr. James E. Evans M.I.T. Lincoln Laboratory Lexington, MA
"Review of Current Facilities and Research with Discussion of Future Applications and Directions of Magnetic Resonance Imaging" December 5, 1985	Dr. William Murphy Dr. J. K. T. Kee Department of Radiology Washington University St. Louis, MO
"Algorithms for Estimating Parameters in Dynamic Tracer Studies" December 13, 1985	Mr. John M. Ollinger Biomedical Computer Laboratory Washington University St. Louis, MO
"Radar Development - The Early Years" A film made by the British Ministry of Defense January 14, 1986	Professor Harold Shipton Biomedical Computer Laboratory Washington University St. Louis, MO

"VSH Views"

March 11, 1986

Dr. John B. Zimmerman
Department of Computer Science
Washington University
St. Louis, MO

"The Application of Maximum-Entropy and Maximum-Likelihood for Image Reconstruction and Spectrum Estimation"

April 25, 1986

Dr. Michael I. Miller
Biomedical Computer Laboratory
Washington University
St. Louis, MO

- - - - - - - - - - - - -

Other Activities

A Lecture Series in support of Biomedical Engineering 3/2 Intensive Course
Sponsored by the Program in Biomedical Engineering
Sever Institute of Technology
Washington University

"Scope of Biomedical Engineering" December 30, 1985	Harold W. Shipton Biomedical Computer Laboratory Washington University St. Louis, MO
"Physical Principles of Tracer Kinetics" December 30, 1985	Kenneth B. Larson Biomedical Computer Laboratory Washington University St. Louis, MO
a film - "The Brain" January 1, 1986	Harold W. Shipton Biomedical Computer Laboratory Washington University St. Louis, MO
"Biomedical Instrumentation and Transducers" January 3, 1986	R. Martin Arthur Department of Electrical Engineering Biomedical Computer Laboratory Washington University St. Louis, MO
"Computers: Communication and Storage" January 9, 1986	G. James Blaine Biomedical Computer Laboratory Washington University St. Louis, MO
"Computers, Cardiologists and Cardiograms" January 10, 1986	Lewis J. Thomas, Jr. Biomedical Computer Laboratory Washington University St. Louis, MO

VIII. PUBLICATIONS AND ORAL PRESENTATIONS

Akita, H., Creer, M. H., Yamada, K. A., Sobel, B. E., and Corr, P. B., "The Electrophysiologic Effects of Intracellular Lysophosphoglycerides and Their Accumulation in Cardiac Lymph with Myocardial Ischemia in Dogs," Journal of Clinical Investigation, in press.

Bergmann, S. R., Fox, K. A. A., Knabb, R. M., and Sobel, B. E., "Salvage of Reperfused Myocardium Detected by Sequential Positron Emission Tomography (PET)," Journal of Nuclear Medicine, vol. 27, p. 732, 1986 (abstract).

Bergmann, S. R., Fox, K. A. A., Geltman, E. M., and Sobel, B. E., "Positron Emission Tomography of the Heart," Progress in Cardiovascular Diseases, vol. 28, pp. 165-194, 1985.

Bergmann, S. R., Fox, K. A. A., and Ludbrook, P. A., "Determinants of Salvage of Jeopardized Myocardium After Coronary Thrombolysis," in Cardiology Clinics, in press.

Bergmann, S. R., Ludbrook, P. A., and Sobel, B. E., "Coronary Thrombolysis with Tissue-Type Plasminogen Activator," in Cardiology Clinics, in press.

Broadstone, S. R., "Ultrasonic Reflection Tomography: An Off-Line High Resolution Imaging System for Tissue Characterization," Master of Science thesis, Department of Electrical Engineering, Washington University, St. Louis, MO, May 1986.

Broadstone, S. R., and Arthur, R. M., "Ultrasonic Reflection Tomography: An Off-Line Imaging System for Tissue Characterization," Ultrasonic Imaging, vol. 8, no. 1, p. 41, January 1986 (abstract).

Chabut, J. C., "An Examination of FSK-Based Digital Picture Communication Over the CATV Medium," Master of Science thesis, Department of Electrical Engineering, Washington University, St. Louis, MO, August 1985.

Corr, P. B., "Amphipathic Metabolites and Malignant Arrhythmias During Ischemia," Journal of Molecular and Cellular Cardiology, vol. 18, supplement I, p. 77, 1986 (abstract).

Corr, P. B., Akita, H., Creer, M. H., Yamada, K. A., and Sobel, B. E., "Increased Concentrations of Lysophosphatidylcholine in Cardiac Lymph from Ischemic Zones," Federation Proceedings, vol. 45, p. 657, 1986 (abstract).

Corr, P. B., and Cain, M. E., "Electrophysiology," in Cardiovascular Pathophysiology, G. G. Ahumada, ed., Oxford University Press, New York, in press.

Corr, P. B., Saffitz, J. E., and Sobel, B. E., "Contributions of Altered Lipid Metabolism to Arrhythmogenesis in the Ischemic Heart," in Life Threatening Arrhythmias During Ischemia and Infarction, M. J. Janse and D. J. Hearse, eds., in press.

Corr, P. B., Yamada, K. A., Creer, M., Sharma, A. D., and Sobel, B. E., "Lysophosphoglycerides and Ventricular Fibrillation Early After Onset of Ischemia," Journal of Molecular and Cellular Cardiology, in press.

Corr, P. B., Yamada, K. A., and Witkowski, F. X., "Mechanisms Controlling Cardiac Autonomic Function and Their Relation to Arrhythmogenesis," in The Heart and Cardiovascular System, H. A. Fozzard, E. Haber, R. B. Jennings, A. M., Katz, and H. E. Morgan, eds., Raven Press, New York, in press.

Cox, Jr., J. R. "Arbiter Specification and Fair Behavior," Proceedings of the Workshop on Computation Models and Realizations," St. Louis, MO, November 1985, in press.

Cox, Jr., J. R., and Zeelenberg, C., "Computer Technology: State of the Art and Future Trends," Journal of the American College of Cardiology, in press.

Eisenberg, P. R., Lee, R. G., Biello, D. R., Geltman, E. M., and Jaffe, A. S., "Chest Pain After Nontransmural Infarction: The Absence of Remediable Coronary Vasospasm," American Heart Journal, vol. 110, no. 3, pp. 515-521, 1985.

Eisenberg, P. R., Schechtman, K. B., Sherman, L. A., Sobel, B. E., and Jaffe, A. S., "Fibrinopeptide A - A Marker for Acute Coronary Thrombosis," Clinical Research, vol. 33, p. 182A, 1985 (abstract).

Eisenberg, P. R., Sherman, L., Rich, M., Schwartz, D., Schechtman, K. B., Geltman, E. M., Sobel, B. E., and Jaffe, A. S., "Determinants of Persistent Recanalization of Reocclusion Early After Thrombolysis: The Role of Continuing Activation of Thrombin," Journal of the American College of Cardiology, in press.

Eisenberg, P. R., Sherman, L., Rich, M., Schwartz, D., Schechtman, K., Geltman, E. M., Sobel, B. E., and Jaffe, A. S., "Importance of Continued Activation of Thrombin Reflected by Fibrinopeptide A to the Efficacy of Thrombolysis," Journal of the American College of Cardiology, vol. 7, pp. 1255-1261, 1986.

Fields, L. E., and Bergmann, S. R., "Normalization of Cardiac Dysfunction Induced by Diabetes by Reduction of the Concentration of Exogenous Fatty Acid," Journal of the American College of Cardiology, vol. 7, p 249A, 1986 (abstract).

Fields, L. E., Daugherty, A., and Bergmann, S. R., "Effect of Exogenous Fatty Acid Levels on Mechanical Performance and Lipid Content of Hearts Isolated from Alloxan-Diabetic Rabbits," American Journal of Physiology: Heart and Circulatory Physiology, in press.

Fox, K. A. A., Abendschein, D. R., Ambos, H. D., Sobel, B. E., and Bergmann, S. R., "Efflux of Metabolized and Non-Metabolized Fatty Acid from Canine Myocardium: Implications for Quantifying Myocardial Metabolism Tomographically," Circulation Research, vol. 57, pp. 232-243, 1985.

Fox, K. A. A., Bergmann, S. R., and Sobel, B. E., "Pathophysiology of Myocardial Reperfusion," Annual Review of Medicine, vol. 36, pp. 125-144, 1985.

Fox, K. A. A., Knabb, R. M., Bergmann, S. R., and Sobel, B. E., "Progress in Cardiac Positron Emission Tomography with Emphasis on Carbon-11 Labeled Palmitate and Oxygen-15 Labeled Water," in Noninvasive Imaging of Myocardial Metabolism, E. Van der Wall, ed., Martinus Nijoff Publishers, in press.

Fox, K. A. A., Knabb, R. M., Rosamond, T., Robison, A. K., Sobel, B. E., and Bergmann, S. R., "Prevention of Coronary Thrombosis with Sub-Thrombolytic Doses of Tissue-Type Plasminogen Activator (rt-PA)," Circulation, vol. 72., p. II-121, 1985 (abstract).

Fox, K. A. A., Robison, A. K., Knabb, R. M., Rosamond, T. L., Sobel, B. E., and Bergmann, S. R., "Prevention of Coronary Thrombosis with Subthrombolytic Doses of Tissue-Type Plasminogen Activator," Circulation, vol. 72, pp. 1346-1354, 1985.

Fox, K. A. A., Saffitz, J. E., and Corr, P. B., "Pathophysiology of Myocardial Reperfusion," in Thrombolysis and Myocardial Infarction, B. E. Sobel, ed., Cardiology Clinics, W. B. Saunders, Co., Philadelphia, in press.

Geltman, E. M., Bergmann, S. R., and Sobel, B. E., "Cardiac Positron Emission Tomography," in Positron Emission Tomography," M. Reivich and A. Alavi, eds., Alan R. Liss, Inc., New York, pp. 345-385, 1985.

Glueck, R. M., Mottley, J. G., Miller, J. G., Sobel, B. E., and Perez, J. E., "Effects of Coronary Artery Occlusion and Reperfusion on Cardiac Cycle-Dependent Variation of Myocardial Ultrasonic Backscatter," Circulation Research, vol. 56, pp. 683-689, 1985.

Glueck, R. M., Mottley, J. G., Sobel, B. E., Miller, J. G., and Perez, J. E., "Changes in Ultrasonic Attenuation and Backscatter of Muscle with State of Contraction," Ultrasound in Medicine and Biology, vol. 11, 605-610, 1985.

Gross, R. W., Corr, P. B., and Sobel, B. E., "Alterations in Phospholipid Metabolism During Myocardial Ischemia and Their Electrophysiologic and Biophysical Sequelae," Environmental Medicine, in press.

Harms, W. B., Slessinger, E. D., Wong, J. W., and Purdy, J. A., "Experimental Tests for Three-Dimensional Dose Calculations," accepted for presentation at the 28th Annual Meeting of the American Association of Physicists in Medicine, Lexington, KY, August 3-7, 1986.

Hart, Jr., W. M., "Color Contrast Perimetry: Hue Discrimination Defects in Acquired Dyschromatopsias," Documente Ophthalmologica Proceedings Series, in press.

Hart, Jr., W. M., Kosmorsky, G., and Burde, R. M., "Color Perimetry of Central Scotomas in Diseases of the Macula and Optic Nerve," in Documente Ophthalmologica Proceedings, Series 42, (6th International Visual Fields Symposium), A. Heijl and E. L. Greve, eds., Dr. W. Junk, Dordrecht, The Netherlands, pp. 239-245, 1985.

Hughes, B., Bergmann, S. R., Corr, P. B., and Sobel, B. E., "External Detection of β-Adrenoceptors with ^{125}I-Hydroxybenzylpindolol in Isolated Perfused Hearts," International Journal of Nuclear Medicine and Biology, in press.

Hughes, B., Marshall, D. R., Sobel, B. E., and Bergmann, S. R., "Characterization of Beta-Adrenoreceptors in vivo with Iodine-131 Pindolol and Gamma Scintigraphy," Journal of Nuclear Medicine, vol. 27, pp. 660-667, 1986.

Jaffe, A. S., Serota, H., Grace, A., and Sobel, B. E., "Diagnostic Changes in Plasma Creatine Kinase Isoforms Early After the Onset of Acute Myocardial Infarction," Circulation, in press.

Jaffe, A. S., and Sobel, B. E., "Thrombolysis with t-PA - Potentials and Pitfalls," Journal of the American Medical Association," vol. 255, pp. 237-239, 1986.

Johnston, P. H., "Phase-Insensitive Detection and the Method of Moments for Ultrasonic Tissue Characterization," Department of Physics, Washington University, St. Louis, MO, August 1985 (Ph.D. Dissertation).

Johnston, P. H., and Miller, J. G., "A Comparison of Backscatter Measured by Phase Sensitive and Phase Insensitive Detection," IEEE Transactions on Ultrasonics, Ferroelectrics, and Frequency Control, vol. UFFC-33, p. 78, 1986 (abstract).

Johnston, P. H., and Miller, J. G., "A Comparison of Backscatter Measured by Phase Sensitive and Phase Insensitive Detection," Proceedings of the 1985 IEEE Ultrasonics Symposium, in press.

Johnston, P. H., and Miller, J. G., "Phase-Insensitive Detection for Measurement of Backscattered Ultrasound," IEEE Transactions on Ultrasonics, Ferroelectrics, and Frequency Control, in press.

Jost, R. G., Hill, R. L., Blaine, G. J., and Cox, Jr., J. R., "PACS Experience as a Motivation for a Campus-Wide Picture Network," Proceedings of SPIE: Application of Optical Instrumentation in Medicine XIV and Picture Archiving and Communication Systems (PACS IV) for Medical Applications, Newport Beach, CA, vol. 626, pp. 549-556, February 1986.

Knabb, R. M., Fox, K. A. A., Sobel, B. E., and Bergmann, S. R., "Characterization of the Functional Significance of Subcritical Coronary Stenoses with $H_2{}^{15}O$ and Positron-Emission Tomography," Circulation, vol. 71, pp. 1271-1278, 1985.

Knabb, R. M., Fox, K. A. A., Sobel, B. E., and Bergmann, S. R., "Sequential Tomographic Assessment of Myocardial Perfusion and Metabolism After Coronary Thrombolysis," Circulation, vol. 72, p. II-138, 1985 (abstract).

Knabb, R. M., Rosamond, T. L., Fox, K. A. A., Sobel, B. E., and Bergmann, S. R., "Enhancement of Salvage of Reperfused Myocardium by Diltiazem," Journal of the American College of Cardiology, in press.

Knabb, R. M., Rosamond, T. L., Sobel, B. E., Fox, K. A. A., and Bergmann, S. R., "Enhanced Salvage of Reperfused Myocardium by Diltiazem Administered Prior to Coronary Thrombolysis," Journal of the American College of Cardiology," vol. 7, p. 53A, 1986 (abstract).

Knabb, M. T., Saffitz, J. E., Corr, P. B., and Sobel, B. E., "Endogenous Amphiphiles and Arrhythmogenesis: A Relationship Demonstrated in Hypoxic Myocytes," Circulation, vol. 72, supplement III, p. III-235, 1985 (abstract).

Knabb, M. T., Saffitz, J. E., Corr, P. B., and Sobel, B. E., "The Dependence of Electrophysiologic Derangements on Accumulation of Endogenous Long-Chain Acyl Carnitine in Hypoxic Neonatal Rat Myocytes," Circulation Research, vol. 58, 230-240, 1986.

Kramer, J. B., Davis, A. G., Dean, Jr., R., McCluskey, E. R., Needleman, P., and Corr, P. B., "Thromboxane A_2 Does Not Contribute to Arrhythmogenesis During Infarction," Circulation, vol. 72, supplement III, p. III-228, 1985 (abstract).

Kramer, J. B., Dean, Jr., R., and Corr, P. B., "Protective Effect of Cardiac Sympathectomy on Lethal Arrhythmias During Chronic Myocardial Infarction," Surgical Forum, vol 36, pp. 227-229, 1985.

Kramer, J. B., Saffitz, J. E., and Corr, P. B., "Mechanisms of Arrhythmogenesis During Chronic Myocardial Infarction," European Heart Journal, in press.

Kramer, J. B., Saffitz, J. E., and Corr, P. B., "Mechanisms of Polymorphic Nonsustained Ventricular Tachycardia During Infarction," Circulation, vol. 72, supplement III, p. III-279, 1985 (abstract).

Kramer, J. B., Corr, P. B., Cox, J. L., Witkowski, F. X., and Cain, M. E., "Simultaneous Computer Mapping to Facilitate Intra-Operative Localization of Accessory Pathways in Patients with Wolff-Parkinson-White Syndrome," American Journal of Cardiology, vol. 56, pp. 571-576, 1985.

Kramer, J. B., Davis, A. G., Dean, R., McCluskey, E. R., Needleman, P., and Corr, P. B., "Thromboxane A_1 Does Not Contribute to Arrhythmogenesis During Evolving Canine Myocardial Infarction," Journal of Cardiovascular Pharmacology, vol. 7, pp. 1069-1076, 1985.

Kramer, J. B., Saffitz, J. E., Witkowski, F. X., and Corr, P. B., "Intramural Reentry As a Mechanism of Ventricular Tachycardia During Evolving Canine Myocardial Infarction," Circulation Research, vol. 56, pp. 736-754, 1985.

Larson, K. B., "Physical and Mathematical Principles of Tracer Kinetics in Biological Applications," seminar presented to Washington University Three-Two Program students, St. Louis, MO, December 30, 1985.

Lerch, R., and Bergmann, S. R., "Assessment of Myocardial Metabolism with ^{11}C-Palmitate. Comparison with ^{123}I-Heptadecanoic Acid," European Heart Journal, vol. 6 (supplement B), pp. 21-27, 1985.

Lindsay, B. D., Ambos, H. D., Schechtman, K. B., and Cain, M. E., "Improved Selection of Patients for Programmed Ventricular Stimulation by Frequency Analysis of Signal-Averaged ECG's," Circulation, vol. 73, pp. 675-683, 1986.

Mead, C. N., Clark, K. W., and Thomas, Jr., L. J., "An Annotated Clinical Event Database as a Tool for Evaluating Dysrhythmia Detector Performance," accepted for presentation at the IEEE Conference on Computers in Cardiology, Boston, MA, October 7-10, 1986.

The MILIS Study Group, "Hyaluronidase Therapy for Acute Myocardial Infarction: Results of a Randomized, Blinded, Multicenter Trial," American Journal of Cardiology, vol. 57, pp. 1236-1243, 1986.

Miller, J. G., Perez, J. E., Mottley, J. G., Madaras, E. I., Johnston, P. H., Blodgett, E. D., Thomas III, L. J., and Sobel, B. E., "Myocardial Tissue Characterization: An Approach Based on Quantitative Backscatter and Attenuation," IEEE Transactions on Sonics and Ultrasonics, vol. SU-32, p. 111, 1985 (abstract).

Miller, J. G., Perez, J. E., and Sobel, B. E., "Ultrasonic Tissue Characterization of Myocardium," Progress in Cardiovascular Disease, vol. 28, pp. 85-110, 1985.

Miller, M. I., "Strategies for the Representation of Broadband Stimuli in the Discharge Patterns of Auditory Nerve Fibers," presented at the NATO Conference Advanced Research Workshop in Auditory Frequency Selectivity, Cambridge, England, June 1986.

Miller, M. I., Karamanos, N. A., and Bosch, W. R., "E-M Algorithms for Estimating Parameters from Single-Memory Markov Point-Processes Having a Multiplicate Intensity," Proceedings of the Twenty-Third Annual Allerton Conference on Communication, Control and Computing, Monticello, IL, pp. 370-371, 1985.

Miller, M. I., Larson, K. B., Saffitz, J. E., Snyder, D. L., Thomas, L. J., and Roysam, B., "A New Method for Analysis of Electron Microscopic Autoradiographs," Journal of Cell Biology, vol. 101, no. 5, (pt 2), p. 85a, 1985 (abstract).

Miller, M. I., Larson, K. B., Saffitz, J. E., Snyder, D. L., and Thomas, Jr., L. J., "Maximum Likelihood Estimation Applied to Electron-Microscopic Autoradiography," Journal of Electron Microscopy Technique, vol. 2, pp. 611-636, 1985.

Miller, M. I., Roysam, B., Saffitz, J. E., Larson, K. B., Snyder, D. L., and Thomas, Jr., L. J., "A New Method for the Analysis of EM Autoradiographs," accepted for presentation at the 3rd International Symposium on Autoradiography, Sheffield University, Sheffield, England, September 16-18, 1986.

Miller, M. I., Roysam, B., Saffitz, J. E., Larson, K. B., and Thomas, Jr., L. J., "Validation of Maximum-Likelihood Analysis of Electron Microscopic Autoradiographs," Proceedings of the 70th Annual FASEB Meeting, St. Louis, MO, vol. 45, no. 3, p. 470, 1986 (abstract).

Miller, M. I., Snyder, D. L., and Moore, S. M., "An Evaluation of the Use of Sieves for Producing Estimates of Radioactivity Distributions with the EM Algorithm for PET," IEEE Transactions on Nuclear Science, vol. NS-33, no. 1, pp. 492-495, February 1986.

Miller, M. I., and Snyder, D. L., "Applications of Maximum-Likelihood Estimation to Biomedical Imaging," presented at the Seventh Annual Conference, Frontiers of Engineering and Computing in Health Care, Chicago, IL, September 28-30, 1985.

Miller, T. R., Grossman, S. J., Schechtman, K. B., Biello, D. R., Ludbrook, P. A., and Ehsani, A. A., "The Association of Age and Other Factors with Rapid Diastolic Filling," Journal of the American College of Cardiology, in press.

Ollinger, J. M., and Snyder, D. L., "An Evaluation of an Improved Method for Computing Histograms in Dynamic Tracer Studies Using Positron Emission Tomography," IEEE Transactions on Nuclear Science, vol. NS-33, no. 1, pp. 435-438, February 1986.

Perlmutter, J. S., Larson, K. B., Raichle, M. E., Markham, J., Mintun, M. A., Kilbourne, M. R., and Welch, M. J., "Strategies for In Vivo Measurement of Receptor Binding Using Positron Emission Tomography," Journal of Cerebral Blood Flow and Metabolism, vol. 6, pp. 154-169, 1986.

Pogwizd, S. M., and Corr, P. B., "Electrophysiologic Mechanisms Responsible for Arrhythmias During Reperfusion of Ischemic Myocardium," Federation Proceedings, vo. 45, p. 779, 1986 (abstract).

Pogwizd, S. M., Kramer, J. B., Saffitz, J. E., and Corr, P. B., "Intramural Reentry as a Basis for Ventricular Arrhythmias Induced by Ischemia," Circulation, vol. 72, supplement III, p. III-227, 1985 (abstract).

Pogwizd, S. M., Onufer, J. R., Kramer, J. B., Sobel, B. E., and Corr, P. B., "Induction of Delayed Afterdepolarizations and Triggered Activity in Canine Purkinje Fibers by Lysophosphoglycerides," Circulation Research, in press.

Politte, D. G., Hoffman, G. R., Beecher, D. E., Ficke, D. C., Holmes, T. J., and Ter-Pogossian, M. M., "Image-Reconstruction of Data from Super PETT I: A First-Generation Time-of-Flight Positron-Emission Tomograph," IEEE Transactions on Nuclear Science, vol. 33, no. 1, pp. 428-434, February 1986.

Purdy, J. A., Harms, W. B., Wong, J. W., Matthews, J. W., and Emami, B. E., "Three Dimensional Radiation Treatment Planning System," accepted for presentation at the 28th Annual Meeting of the American Association of Physicists in Medicine, Lexington, KY, August 3-7, 1986.

Purdy, J. A., Wong, J., and Harms, W. B., "New Developments in Three Dimensional Radiotherapy Treatment Planning," Proceedings of the PC Users Group Symposium, Tokyo, Japan, October 15, 1986, in press

Purdy, J. A., Wong, J. W., Harms, W. B., and Emami, B. E., "State-of-the-Art High Energy Photon Treatment Planning," in Frontiers of Radiation Therapy and Oncology, vol. XXI, Treatment Planning in the Radiation Therapy of Cancer, J. M. Vaeth, ed., in press.

Purdy, J. A., Wong, J. W., Harms, W. B., Emami, B., and Matthews, J. W., "State-of-the-Art of High Energy Photon Treatment Planning," Proceedings of the Twenty-First Annual San Francisco Cancer Symposium, February 28-March 2, 1986, in press.

Rosamond, T. L., Abendschein, D., Bergmann, S. R., and Fox, K. A. A., "The Metabolic Fate of Labeled Palmitate in Ischemic Myocardium: Implications for Positron Emission Tomography (PET)," Circulation, vol. 72, p. II-468, 1985 (abstract).

Saffitz, J. E., and Corr, P. B., "Autoradiographic Detection of Alterations of Myocardial Adrenergic Receptors Induced by Ischemia," European Heart Journal, in press.

Saffitz, J. E., and Corr, P. B., "Quantitative Characterization of $Alpha_1$-Adrenergic Receptors in Transmural Slices of Myocardium," Circulation, vol. 72, supplement III, p. III-329, 1985 (abstract).

Sedlis, S. P., Schechtman, K. B., Ludbrook, P. A., and Schonfeld, G., "The Ratio of Apoprotein AI to Apoprotein B Correlates with the Severity of Coronary Artery Disease," Circulation, vol. 72, supplement III, p. III-184, 1985 (abstract).

Sedlis, S. P., Schechtman, K. B., Ludbrook, P. A., Sobel, B. E., and Schonfeld, G., "Plasma Apoproteins and the Severity of Coronary Artery Disease," Circulation, vol. 73, pp. 978-986, 1986.

Sharma, A. D., and Corr, P. B., "Alpha-Adrenergic Mediated Effects of Catecholamine in the Ischemic and Reperfused Heart," in Alpha-Adrenoceptor Blockers in Cardiovascular Disease, Churchill Livingstone, NY, pp. 249-264, 1985.

Shipton, H. W., "From Entertainment to Education; from Education to Enlightment," in Topographic Mapping of Brain Electrical Activity, F. H. Duffy, ed., Butterworth Publishers, Stoneham, MA, pp. 217-224, 1986.

Shipton, H. W., "Topography," in Encyclopedia of Neuroscience, G. Adelman, ed., in press.

Slessinger, E., Wong, J., Vannier, M., Hermes, R., and Roy, T., "Clinical Application of a New Treatment Verification Approach," accepted for presentation at the 28th Annual American Association of Physicists in Medicine, Lexington, KY, August 3-7, 1986.

Snyder, D. L., and Miller, M. I., "Estimation Under Quantum-Limited Conditions," Topical Meeting on Quantum-Limited Imaging and Image Processing Technical Digest, Optical Society of America, Honolulu, Hawaii, pp. 120-123, March 31-April 2, 1986.

Snyder, D. L., and Miller, M. I., "The Use of Sieves to Stabilize Images Produced with the EM Algorithm for Emission Tomography," IEEE Transactions on Nuclear Science, vol. NS-32, pp. 3864-3872, October 1985.

Sobel, B. E., and Bergmann, S. R., "The Impact of Coronary Thrombolysis and Tissue-Type Plasminogen Activator (t-PA) on Acute Myocardial Infarction," in Thrombolysis: Biological and Therapeutic Properties of New Thrombolytic Agents, D. Collen, H. R. Lijnen, and M. Verstraete, eds., Churchill Livingstone, Edinburgh, pp. 61-84, 1985.

Sutera, S. P., Tilton, R. G., Nowak, M. D., Howe, J., Larson, K. B., and Williamson, J. R., "Vascular Flow Resistance in Isolated Rabbit Hearts: In Vivo Viscosity of RBC Suspensions," Federation Proceedings, vol. 45, no. 5, p. 1154, 1985 (abstract).

Thomas III, L. J., Wickline, S. A., Perez, J. E., Sobel, B. E., and Miller, J. G., "A Model for the Change in Backscatter Accompanying the Contraction of Muscle," Ultrasonic Imaging, 1985 (abstract).

Thomas III, L. J., Wickline, S. A., Perez, J. E., Sobel, B. E., and Miller, J. G., "A Real-Time Integrated Backscatter Measurement System for Quantitative Cardiac Tissue Characterization," IEEE Transactions on Ultrasonics, Ferroelectrics, and Frequency Control, vol. UFFC-33, pp. 27-32, 1986.

Tilton, R. G., Cole, P. A., Larson, K. B., Kilo, C., and Williamson, J. R., "Hyaluronidase Does Not Prevent Deterioration of Vascular Functional Integrity During Reperfusion After No-Flow Ischemia in Isolated Rabbit Hearts," Circulation Research, vol. 56, pp. 839-850, 1985.

Toga, A. W., and Arnicar; T. L., "Image Analysis of Brain Physiology," IEEE Computer Graphics and Applications," vol. 5, no. 12, pp. 20-25, 1985.

Toga, A. W., Arnicar, T. L., Samaie, M., Lothman, E. W., and Collins, R. C., "Three Dimensional Study of Functional Anatomy of Experimental Seizures," American Academy of Neurology, in press.

Toga, A. W., Santori, M. S., and Samaie, M., "Regional Distribution of Flunitrazepam Binding Constants: Visualizing Kd and Bmax by Digital Image Analysis," Journal of Neuroscience, in press.

Turi, Z. G., Rutherford, J. D., Roberts, R., Muller, J. E., Jaffe, A. S., Rude, R. E., Parker, C., Raabe, D. S., Stone, P. H., Hartwell, T. D., Lewis S. E., Parker, R. W., Gold, H. K., Robertson, T. L., Sobel, B. E., Willerson, J. T., Braunwald, E., and the Multicenter Investigation for the Limitation of Infarct Size (MILIS), "Electrocardiographic, Enzymatic and Scintigraphic Criteria of Acute Myocardial Infarction As Determined from Study of 726 Patients," American Journal of Cardiology, vol. 55, pp. 1463-1468, 1985.

Turner, J. S., "The Complexity of the Shortest Common Matching String Problem," Washington University Computer Science Department Technical Report, WUCS-86-9, April 30, 1986.

Wickline, S. A., Thomas III, L. J., Miller, J. G., Sobel, B. E., and Perez, J. E., "A Relationship Between Ultrasonic Integrated Backscatter and Myocardial Contractile Function," Journal of Clinical Investigation, vol. 76, pp. 2151-2160, 1985.

Wickline, S. A., Thomas III, L. J., Miller, J. G., Sobel, B. E., and Perez, J. E., "Myocardial Ultrasonic Backscatter: Physiological and Physical Determinants of the Cardiac Cycle-Dependent Variation of Integrated Backscatter," Clinical Research, vol. 33, p. 237A, 1985 (abstract).

Wickline, S. A., Thomas III, L. J., Miller, J. G., Sobel, B. E., and Perez, J. E., "Sensitive Detection of the Effects of Reperfusion on Myocardium by Ultrasonic Tissue Characterization with Integrated Backscatter," Circulation, in press.

Wickline, S. A., Thomas III, L. J., Miller, J. G., Sobel, B. E., and Perez, J. E., "The Dependence of Myocardial Ultrasonic Integrated Backscatter on Contractile Performance," Circulation, vol. 72, pp. 183-192, 1985.

Wong, J., Binns, W. R., Epstein, J. W., Klarmann, J., and Israel, M. H., "Plastic Scintillator Sheet as a Real Dosimeter in Radiotherapy," accepted for presentation at the 28th Annual Meeting of the American Association of Physicists in Medicine, Lexington, KY, August 3-7, 1986.

Wong, J., and Purdy, J., "An Examination of Recent Methods of Photon Dose Calculations," accepted for presentation at the 28th Annual Meeting of the American Association of Physicists in Medicine, Lexington, KY, August 3-7, 1986.

Yamada, K. A., Akita, H., Sobel, B. E., and Corr, P. B., "The Dependence of Electrophysiologic Effects Induced by Lysophosphatidylcholine on the Compartment in Which It Resides," Federation Proceedings, vol. 45, p. 657, 1986 (abstract).

Yamada, K. Y., Saffitz, J. E., and Corr, P. B., "Role of Alpha- and Beta-Adrenergic Receptor Stimulation in the Genesis of Arrhythmias During Myocardial Ischaemia," European Heart Journal, in press.

Yamada, K. A., Saffitz, J. E., and Corr, P. B., "Sympathetic Influences on Arrhythmogenesis in the Ischemic Heart," European Heart Journal, in press.

Yamada, K. A., Saffitz, J. E., Sobel, B. E., and Corr, P. B., "Enhanced Salvage of Reperfused, Ischemic Myocardium by α-Adrenergic Blockade," Journal of American College of Cardiology, vo. 7, p. 54A, 1986 (abstract).

Yu, C. X., Wong, J. W., and Purdy, J. A., "Photon Dose Perturbations Due to Small Inhomogeneities," Medical Physics, vol. 12, p. 521, 1985 (abstract).

IX. MONOGRAPHS AND WORKING NOTES

The Biomedical Computer Laboratory's Monograph Series was established to systematize the many reports, reprints, program descriptions and other documents written at BCL or supported in part by the Laboratory's facilities or staff.

A forum, much less formal than our monograph series, has been instituted to serve as a repository for materials such as: research notes, system and component documentation, technical survey notes and prepublication drafts. Working Note Files are maintained for access by anyone associated with the Institute for Biomedical Computing. Distribution for outside use can be made available with the consent of the contributing author.

Monographs

Following is a list of the monographs published by BCL during the past year. Copies of the complete index to the Monograph Series are available on request.

Monograph Number	Author(s)	Title	Date
469	Chabut, J. C.	An Examination of FSK-Based Digital Picture Communication Over the CATV Medium	8/85
470	Miller, M. I. Snyder, D. L. Moore, S. M.	An Evaluation of the Use of Sieves for Producing Estimates of Radioactivity Distributions with the EM Algorithm for PET	10/85
471	Ollinger, J. M. Snyder, D. L.	An Evaluation of an Improved Method for Computing Histograms in Dynamic Tracer Studies Using Positron-Emission Tomography	10/85
472	Jost, R. G. Hill, R. L. Blaine, G. J. Cox, Jr., J. R.	PACS Experience as a Motivation for a Campus-Wide Picture Network	1/86
473	Perlmutter, J. S. Larson, K. B. Raichle, M. E. Markham, J. Mintun, M. A. Kilbourn, M. R. Welch, M. J.	Strategies for In Vivo Measurement of Receptor Binding Using Positron-Emission Tomography	5/86

Monograph Number	Author(s)	Title	Date
474	Fuhrmann, D. R. Drury, H. Akhtar, S. Brown, M.	EMAMAP; An Interactive Data Acquisition Program for Electron Microscopic Autoradiography	6/86
475	Mead, C. N. Clark, K. W. Platt, J. C. Thomas, Jr., L. J.	ARGUS: Algorithm Development: A Decade of Progress Results of Final System Evaluation and Implementation in a CMOS Environment	1/85

Working Notes

Following is an index of notes submitted during the current reporting period.

Working Note Number	Author(s)	Title	Date
69	Videen, T. O.	APl: Analysis Program for Super PET I User's Manual	7/85
70	Videen, T. O.	User's Manual for IMAGES	7/85
71	Videen, T. O.	User's Manual for LABELS	7/85
72	Fuhrmann, D. R.	EMA Map Program Specification	9/85
73		WITHDRAWN	
74	Markham, J.	Coordinate Transformation for Super PET Data	12/85

IPAQ Working Notes

Working Note Number	Author(s)	Title	Date
1	Blaine, J.	IPAQ Task Review	8/85
2	Blaine, J. Hermes, R.	A Partial Survey of Image Digitizing Products	9/85
3	Macke, E. Hermes, R.	Report on Device Driver Investigations to Date	12/85

Working Note Number	Author(s)	Title	Date
4	Hermes, R. Moore, S.	DRAFT IPAQ Image File Format Description	5/86
5	Fuhrmann, D.	MIXPAINT - a Utility for Color Selection	6/86
6	Suppplied by F. Rosenberger	Reports on UNIX Word Processing from High Altitude Observatory	6/86
7	Ollinger, J.	How to Run Jobs Sequentially, at Low Priority and/or in Background on UNIX or How to Number-Crunch and Remain Popular	7/86